Max-Planck-Institut für Kolloid und Grenzflächenforschung

Novel Carbon Materials with Hierarchical Porosity: Templating Strategies and Advanced Characterization

Dissertation

zur Erlangung des akademischen Grades
"doctor rerum naturalium"
(Dr. rer. nat.)
in der Wissenschaftsdisziplin "Physikalische Chemie"

eingereicht an der
Mathematisch-Naturwissenschaftlichen Fakultät
Universität Potsdam

von
Philipp Adelhelm

Potsdam, im Mai 2007

Contents

Chapter 1

Introduction

Within the periodic table, the sixth element, *carbon,* shows several unique characteristics making it one of the most important ones in ancient times and modern chemistry. As the integral part of natural matter, carbon materials such as wood and coal were first used as combustible, constructing materials or as pigment. After the discovery of the element character by the french chemist LAVOISIER around 1780, carbon became today's backbone of a whole branch in modern chemistry (Organic Chemistry), mainly due to its abundance and ability to bond with itself and other atoms in a plentiful fashion. The nature of the bonding between carbon atoms is determined by the electronic configuration and gives rise to allotropes of completely different properties. In diamond, each carbon atom is bonded to four others (sp^3 hybridization) forming a three-dimensional framework of cubic symmetry. In graphite, each carbon atom is bonded to three others (sp^2 hybridization) forming planar sheets in a hexagonal stacking. These two allotropes impossingly show the diversity in the carbon world. On one side, diamond is a highly transparent material and known as the hardest natural material. It does not conduct electricity whereas it can transport heat in an incomparable way (more than 100 times better than aluminum). On the other side, graphite is opaque, used for thermal insulation, conducts electricity and is soft enough to be used as a dry lubricant. Graphite is the thermodynamically stable form of carbon at moderate temperatures and pressures and melts at

4000 °C. Diamond only forms when high temperature is accompanied by high pressure and can be found in nature only because the transformation into graphite is kinetically hindered. The carbon family was extended by famous discoveries in the 80's and 90's of last century: Carbon nanotubes and fullerenes. Both allotropes are supposed to be very useful for future applications [1–4]. For example, carbon nanotubes exhibit one of the highest Young's moduli ever measured. Fullerenes, molecules that are shaped like soccer balls, are supposed act as carriers for small molecules [5,6]. Other exotic forms of carbon like carbon nanofoam - the solid with the lowest density ever reported is supposed to be ferromagnetic [8] - or carbon nano-onions [9] were also discovered during the last years. Figure 1.1 shows different forms of the element carbon.

Besides these forms of carbon, plenty *carbon materials* (e.g. in form of powders, fibers, foams, fabrics or composites) were described and entered our daily live. Carbon materials are solids with a high carbon content and structurally in a non-graphitic state. For example, activated carbons are widely used to remove harmful contaminates from liquids or the human body and can be made from natural carbon sources such as wood or nut shells. Carbon fibers show excellent mechanical properties and resistance to corrosion combined with low weight and are used e.g. in automobile and aeronautical industry. Other carbon materials are used for thermal insulation, for gas storage or as electrode material [10].

In all cases, it is the carbon structure on the molecular level (*carbon microstructure*) that determines all these properties. It is obvious that an exact

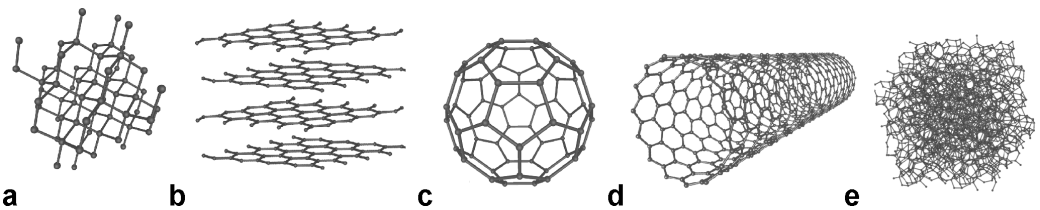

Figure 1.1: Different forms of carbon: *(a)* Diamond, *(b)* Graphite, *(c)* C60 Fullerene, *(d)* Nanotube, *(e)* Amorphous carbon [7].

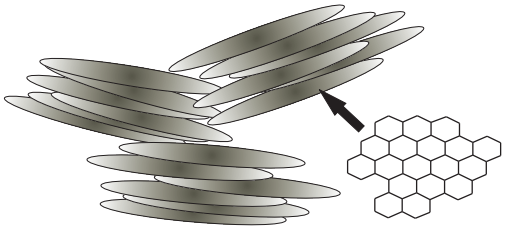

Figure 1.2: Schematic illustration of the carbon microstructure of non-graphitic carbon.

knowledge of the carbon microstructure is highly desirable in order to tune the properties of a carbon material for certain applications.

One focus of this work was to use a wide-angle x-ray scattering model (WAXS model) by Ruland and Smarsly [11] as an advanced technique to obtain very precised information about the carbon microstructure of *non-graphitic carbons.* Briefly, non-graphitic carbons consist of small graphene stacks, usually in the nanometer range. The average dimensions of these stacks (layer size and stack height) determine the degree of order in the material. For example, small stacks of high polydispersity give rise to a very disordered carbon material, whereas large stacks of small polydispersity increase the degree in order. Such differences can be clearly seen in the WAXS pattern of carbon materials. Non-graphitic carbons can be obtained by simple heat treatment of carbon precursors (e.g. organic matter such as sucrose or wood) under reductive atmosphere, yielding an almost pure carbon residue (a process called *carbonization*). Ideally, the carbon precursors transform into graphite if they are heated sufficiently long at temperatures higher than 2000 °C. An illustration of the microstructure of non-graphitic carbon is shown in Figure 1.2.

The standard evaluation techniques (e.g. Raman spectroscopy) give only limited information about the carbon microstructure, whereas the WAXS model allows the determination of several structural parameters, such as polydispersities of the graphene stacks or stresses within the material. Within this work, the model was applied for the first time to a larger series of samples. The evaluation of different carbon precursors regarding their potential use in

the synthesis of new non-graphitic carbon materials is discussed in Chapter 3. In particular, the microstructure of carbon materials derived from *mesophase pitch* is studied in detail, since this carbon precursor is known for its good carbonization behavior and formation of a well-developed carbon microstructure (i.e. large dimensions of the graphene stacks).

Porous Materials

Pores are found everywhere in nature and are crucial for the development of life. As one example, trees transport water and minerals through pores to even the their outermost parts. One can imagine that it is useful to have several huge transport routes from which smaller ones branch off into more distant areas. Such a *hierarchical porous structure* is also found in the human body. The lung is a widely branched porous organ where the exchange of oxygen and carbon dioxide takes place at the interface between lung and air. Clearly, the total uptake of oxygen increases with the total lung / air interface area. The trachea is the main transportation route towards the inner lung, where it finally branches off into around 300.000.000 small pores of around 0.2 mm in diameter creating a surface area of around 70 - 80 m^2 within the comparably small dimensions of a human body.

IUPAC defines pores according to their diameter d as:

- *macropores ($d > 50$ nm)*
- *mesopores ($d = 2$ - 50 nm),* and
- *micropores ($d < 2$ nm)*.

The idea of a large, accessible surface area in a small space is desirable for many chemical processes. Ideally, the chemical compounds are transported in a mobile phase along the hierarchical pore system and react at the interface between mobile and solid phase.

Porous Carbon Materials

One of the main goals of the present work was to synthesize new carbon materials which are particularly useful for energy applications, combining the advantages of a hierarchical porous material with the advantages of carbon itself.

It is found that certain carbon materials can reversibly store lithium ions. Combined with the resistance to corrosion and electrical conductivity, such carbon materials are used as electrodes in e.g. *lithium ion batteries* [12]. Lithium ion batteries are currently the most popular type of secondary batteries used for portable electronic devices such as mobile phones or laptops. Recently, this kind of batteries also attracted attention in the markets of hybrid electric cars, electric cars or in novel transportation systems such as the Segway PT®. In particular, the well-known problem of climate change and global warming boosted the worldwide launch of hybrid cars that are powered by a petrol combustion engine and a battery that drives an electric engine. In particular, the replacement of the classic combustion engine by hybrid systems consisting of batteries on the one side and fuel cells, bio fuel or clean diesel on the other side could help to reduce environmental damage. Also, fuel cell technology still suffers from unsolved engineering and scientific problems making fully electric powered cars a promising technology in the near future [13]. However, electric powered cars still lack feasibility since the cruising range is limited and battery charging times are long. Thus, new materials have to developed in order to satisfy the demand for high performance batteries. Also, so called *supercapacitors* that can quickly store and release energy within seconds could accompany batteries as energy storage devices.

As a major part of this work, new hierarchical porous carbon materials with macro- and mesoporosity were synthesized. Thereto, the so-called *nanocasting* technique was used which allows the synthesis of inorganic nanoporous materials by replication of hard or soft templates [14–16]. In particular, several silica materials with different porosities could be already synthesized that way. Ryoo et al. were the first in 1999 who used mesoporous

silica as a template to create mesoporous carbon by replication of the silica structure [17–19]. Since silica is a solid, inorganic material, this process is called *hard-templating*. The nanocasting of porous carbon materials via the hard-templating approach will be introduced in Chapter 4. As will be shown there, several nanoporous carbon materials could be already synthesized that way. However, the synthesized materials usually exhibited a very disordered carbon microstructure which is particularly undesired for the use as electrode material. Thus, mesophase pitch was used as carbon precursor in this work, in order to obtain a hierarchical porous carbon material that exhibited at the same time a well developed carbon microstructure.

In Chapter 4, a new hard-templating based synthesis procedure is introduced that allowed for the first time the synthesis of a truly hierarchical macro-/ mesoporous carbon monolith using mesophase pitch as carbon precursor. Also, the use or the synthesized material as electrode material (battery) and support material (supercapacitor) is presented.

In Chapter 5, a new synthesis for hierarchical porous carbon materials using the *soft-templating* approach is introduced. The main advantage of soft-templating is that the template is a polymer that can be simply burned off, making the template removal a cheap and easy step. In contrast, hard templates are usually removed by dissolution. One can imagine that soft-templating of carbon materials is a challenge since carbon precursor and template are of organic nature, but only the polymer is supposed to burn off during template removal. Thus, the synthesis of hierarchical macro- / mesoporous carbon materials via soft-templating could be, until now, not realized. The new synthesis takes advantage of the phase separation (spinodal decomposition) between carbon precursor and polymer template. As will be presented, the synthesis also allows the generation of monoliths and could open a new pathway for the synthesis of inexpensive porous carbon materials.

Chapter 2

Analytical Methods

This chapter gives a brief introduction into main analytical methods used in this work.

2.1 Wide-Angle X-ray Scattering (WAXS)

Since the early days of x-ray scattering, structural studies of carbon materials by WAXS were closely linked to the development of theory and experiment since they offer a wide structural variety ranging from perfect 3D order in graphitic carbon to highly disordered non-graphitic carbon with many intermediate states. In recent times, the study of disordered structures by WAXS has been considerably improved due to advances in instrumentation and data processing.

Three different types of scattering are emitted when matter is irradiated by x-rays: coherent (or elastic) scattering, Compton (or inelastic) scattering, and fluorescence radiation. Only the coherent scattering is required for structural studies, the two others are structure independent. Especially for atoms of low atomic number like carbon, the Compton scattering represents a considerable part of the diffuse intensity at higher angles and has to be taken into account in advanced studies of highly disordered structures. Fluorescence radiation (e.g. due impurities of Fe or Co in carbon materials when Cu K_α radiation is used) can be avoided by using an appropriate wave length

of the primary beam.

The basic relationships between an arbitrary structure defined by its electron distribution ρ as a function of the vector $\mathbf{r}$ and the (coherent) scattering intensity I as a function of the scattering vector $\mathbf{s}$ is given by

$$I(\mathbf{s}) = |A(\mathbf{s})|^2 \tag{2.1}$$

The scattering amplitude A is related to ρ by a 3D Fourier transform F of the form

$$A(\mathbf{s}) = F(\rho(\mathbf{r})) = \int_v \rho(\mathbf{r})\, exp\,(2\pi i\, \mathbf{r}\, \mathbf{s})\; dv_r \tag{2.2}$$

$\mathbf{r}\,\mathbf{s}$ is the scalar product of $\mathbf{r}$ and $\mathbf{s}$, dv_r is the volume element in $\mathbf{r}$ space. The vector $\mathbf{s}$ is defined by the scattering geometry

$$\mathbf{s} = (\mathbf{S} - \mathbf{S}_0)/\lambda \tag{2.3}$$

λ is the wave length, $\mathbf{S}$ and $\mathbf{S_0}$ are unit vectors parallel to the directions of the scattering and the primary beam, respectively. All vectors are defined in a sample-fixed coordinate system.

If the structural units in the material are randomly oriented, the scattering (called powder or Debye-Scherrer pattern) represents the spherical average over the intensity contributions of the individual units, the resulting intensity $I(s)$ is thus a function of the absolute value $s = (2sin\theta)/\lambda$ of $\mathbf{s}$ only. 2θ is the angle between $\mathbf{S}$ and $\mathbf{S_0}$.

If the structural units in the material have a uni-axial orientation (texture), the resulting intensity $I(s, \phi)$ is represented by a cylindrically symmetrical distribution in $\mathbf{s}$-space (reciprocal space). ϕ is the polar angle, i.e. the angle between the direction of $\mathbf{s}$ and the principal axis of orientation. If the scattering of such a material is measured in symmetrical reflection on diffractometer and the principle axis of the orientation is perpendicular to the surface of the sample, the observed intensity corresponds to $I(s, 0)$.

Generally, the powder pattern of a material is a characteristic "fingerprint" of the structure. Crystalline materials with large crystallite sizes and low lattice disorder show a series of sharp interference lines and low diffuse

background. These lines are called Bragg reflections, they are centered on s values corresponding to $s_{hkl} = 1/d_{hkl} = (2\,sin\,\theta_{hkl})/\lambda$. θ_{hkl} is the Bragg angle, hkl is the Miller index and d_{hkl} is the Bragg spacing of the corresponding net planes. The concentration of the scattering intensity on $s = s_{hkl}$ requires a perfect lattices of large size. The line profiles increase in width with decreasing size and increasing lattice imperfection. In the latter case, the width also increases with increasing s values. Furthermore, the integral intensity of the lines decreases and the diffuse background increases so that an appropriate line separation becomes eventually impossible.

2.1.1 WAXS pattern of graphitic carbon and non-graphitic carbon

The powder pattern of well-ordered graphite shows a series of sharp reflections at

$$s_{hkl} = \sqrt{4(h^2 + k^2 + hk)\,/(3a^2) + l^2/c^2} \tag{2.4}$$

where a and c are the hexagonal lattice constants. Due to the symmetry of the unit cell, the reflections with odd values of l are absent if $h - k = 3n$. A carbon material is called graphitic if reflections with *(hk)* $\neq$ (00) and l $\neq$ 0, e.g. (101), (103), (112), (114) etc., are clearly visible in the powder pattern. A quantitative characterization separating lattice size and lattice disorder can be performed using standard methods of line profile analysis (Warren-Averbach method) provided the overlap of neighboring line profiles is negligible.

A carbon material is called non-graphitic if only symmetric (00l) and asymmetric (hk) reflections can be detected in the powder pattern. The asymmetry of the (hk) reflections is produced by the anisotropic disorder present in this form of carbon. This disorder is due to statistical rotations and shifts (turbostratic disorder) of the individual carbon layers (graphenes) parallel to each other in a given stack which destroys all interlayer correlation except the parallel stacking. Figure 2.1a shows two WAXS patterns that are typically of non-graphitic carbons.

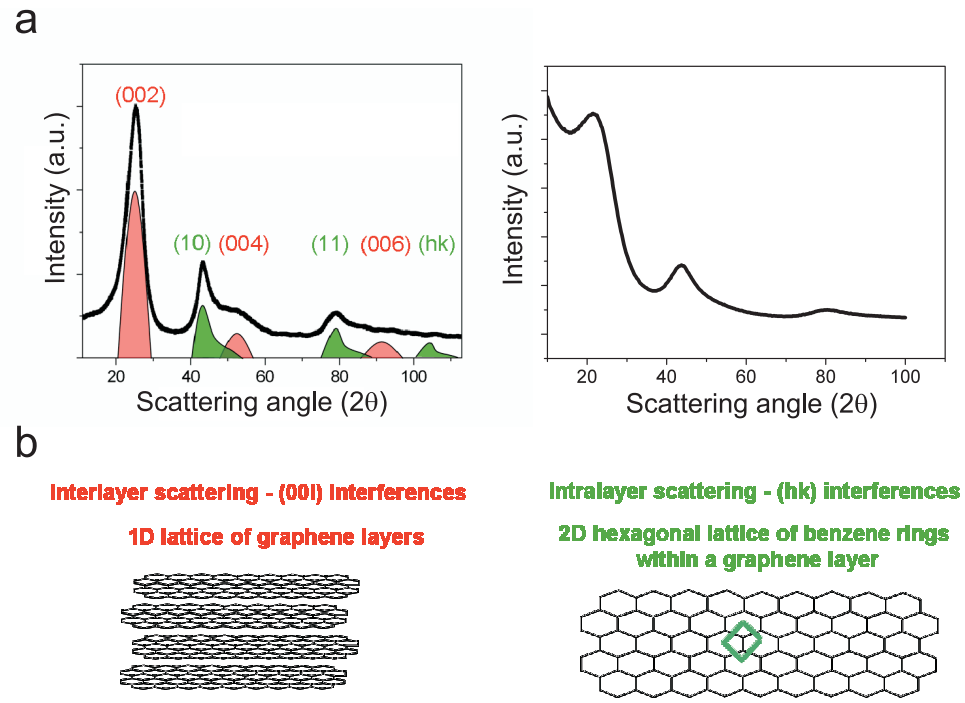

Figure 2.1: *(a)* Typical WAXS patterns of non-graphitic carbons. The (00l) and (hk) reflections are schematically illustrated in red and green color. *(b)* Inter- and intralayer scattering in non-graphitic carbons between and within the graphene layers.

Standard methods of line profile analysis are only possible on (00l) reflections provided they can be effectively separated from neighboring line profiles. The minimum requirement for such an analysis are two complete line profiles of different order, e.g. (002) and (004). This is practically impossible since the (004) profile is, in general, heavily affected by the high-angle tail of the asymmetric (10) line. Although a special method for the analysis of single hk lines exists, the problem of line separation is comparable to that of the (00l) lines [20].

This problem can only be solved by the fitting of theoretical intensity distributions for a structural model containing all relevant parameters over the total range of accessible s values. A model for the improved evaluation of WAXS patterns from non-graphitic carbons is described in the following chapter.

2.1.2 Advanced analysis of WAXS patterns from non-graphitic carbon - WAXS modeling

Within this work, a model for the wide-angle x-ray scattering of non-graphitic carbons developed by RULAND AND SMARSLY [11] was used for the advanced structural analysis of several carbon materials. The basic concept of this model (in the following denoted as *WAXS model*) is described in Ref. [11] as follows:

Considering an intensity distribution I_{obs} obtained experimentally from a sample of non-graphitic carbon without preferred orientation. The relationship to the theoretical intensity distribution normalized in electron units per carbon atom $I_{e.u.}$ is then given by

$$I_{\mathrm{obs}} = kAP(I_{e.u.} \otimes h_b), \tag{2.5}$$

where k is the normalization constant, A the absorption factor, P the polarization factor, and h_b a normalized distribution representing the instrumental broadening. $\otimes$ stands for the operation of h_b on $I_{e.u.}$ which can be expressed as a convolution in small ranges of the scattering angle 2θ. $I_{e.u.}$ is composed of the coherent scattering I_{coh} and the Compton scattering I_{incoh}:

$$I_{e.u.} = I_{coh} + I_{incoh}$$

I_{coh} is composed of the interlayer interferences I_{inter} (i.e. the ensemble of (00l) reflections) and the intralayer interferences I_{intra} (i.e. the ensemble of (hk) reflections).

$$I_{coh} = f_c^2(I_{inter} + I_{intra}) \tag{2.6}$$

f_c is the atomic scattering factor for carbon. No further components of I_{coh} have to be taken into account provided that all carbon atoms are organized in graphenes. If this is not the case, additional components have to be introduced, e.g. for foreign atoms or for structures consisting of sp^3 carbon atoms. This so-called 'non-organized carbon' produces a background scattering without modulation. If the concentration of non-organized carbon is

c_n, and if the normalization of I_{inter} and I_{intra} is kept constant, $\mathrm{I_{coh}}$ is

$$I_{coh} = f_c^2[(1 - c_n)(I_{inter} + I_{intra} - 1) + 1] \tag{2.7}$$

The exact treatment of the inter- and intralayer interferences can be found in the corresponding article [11]. Briefly, following parameters referring to the layer structure can be obtained from the WAXS model:

Symbol	Parameter	
$\mathrm{L_a}$	average layer size	$L_\mathrm{a} := \frac{\langle l^2 \rangle}{\langle l \rangle}$
κ_a	polydispersity of the chord length	$\kappa_a = \frac{\langle l^2 \rangle}{\langle l \rangle^2} - 1$
κ_R	polydispersity of the radii	$\kappa_R = f(\kappa_a)$
$\mathrm{l_{cc}}$	average C-C bond length	
σ_1	disorder parameter	
ε_1	strain parameter	

Table 2.1: Parameters of the WAXS model referring to the layer structure.

With $\langle l \rangle$ being the average chord length.

Parameters referring to the layer stacking are:

Symbol	Parameter	
$\mathrm{L_c}$	average stack height	$L_\mathrm{c} = \overline{a}_3 \frac{\langle N^2 \rangle}{\langle N \rangle}$
κ_c	polydispersity of the stack height	$\kappa_c = \frac{\langle N^2 \rangle}{\langle N \rangle^2} - 1$
$\overline{a}_3$	average interlayer spacing	$\overline{a}_3 = \left\langle \frac{c}{2} \right\rangle$
$a_{3,min}$	minimum of interlayer spacing	
σ_3	disorder parameter (variance of $\overline{a}_3$)	
η	homogeneity of the stacks	

Table 2.2: Parameters referring to the layer stacking.

$\langle N \rangle$ is the average of N, being the number of graphenes per stack.

In the present case, the number distributions of l and N are assumed to be Gamma distributions.

Other parameters determing the intensity function I_{coh} are:

u_3	root mean square displacement of a layer in the direction perpendicular to the layer plane caused by thermal motion
c_n	concentration of non-organized carbon
q	orientation parameter

Table 2.3: Other parameters that determine the intensity function I_{coh}.

The WAXS model considers diffractometer measurements of flat powder samples in symmetrical reflection. Depending on the preparation of the sample, an uniaxial preferred orientation of the carbon layers parallel to the surface of the sample is possible. In this case, the interlayer scattering is increased and the intralayer scattering is reduced. This is of importance, since some samples investigated in this work showed such a preferred orientation. The exact treatment of this effect is rather complicated. However, following approximations can be used when the preferred orientation is relatively small.

The *orientation distribution* (pole figure) $g(\varphi)$ of the $(00l)$ reflections was chosen as

$$g(\varphi) = \frac{(1+q)q^{1/2}}{arctanh\,(q^{1/2})\,[(1+q)^2 - 4q\,cos^2\varphi]} \tag{2.8}$$

where φ is the angle between the perpendicular to the sample surface and the perpendiculars to the layer planes. q is an *orientation parameter*, which varies between zero (absence of preferred orientation) and unity (perfect parallel orientation of the layers).

$g(\varphi)$ is normalized such that

$$\int_0^{\pi/2} g(\varphi)\,sin\varphi\,d\varphi = 1 \tag{2.9}$$

The orientation corrections for an (hk) reflection is approximately (Ru-

land & Tompa, 1968):

$$J_{hk,ori}(s) = J_{hk}(s)\, g\left[arcsin\left(\frac{s_{hk}}{s}\right)\right] \tag{2.10}$$

$$g\left[arcsin\left(\frac{s_{hk}}{s}\right)\right] = \frac{(1+q)q^{1/2}}{arctanh(q^{1/2})[(1-q)^2 + 4qs_{hk}^2/s^2]} \;\; if\ s \geq s_{hk},\ and \tag{2.11}$$

$$g\left[arcsin\left(\frac{s_{hk}}{s}\right)\right] = \frac{q^{1/2}}{arctanh\left(q^{1/2}\right)(1+q)} \;\; if\ s < s_{hk} \tag{2.12}$$

with J_{hk} being the normalized profile of an (hk) reflection.

2.2 Raman spectroscopy of carbon materials

Raman spectroscopy is based on Raman scattering, i.e. the inelastic scattering of photons by phonons due to the change of polarization caused by the phonon mode [21]. The shift in energy gives information about the phonon modes present in the system, and thus information about the structure of the sample. Usually laser light in the visible, near ultraviolet or near infrared range is used for the experiments.

Raman spectroscopy is widely used for the analysis of carbon materials. The most distinct Raman bands that are observed in carbon materials are the D and the G band. Fig. 2.2a shows a typical Raman spectra of non-graphitic carbon. The intensity ratio of D and G band as well as their exact position correlate with the carbon microstructure. The corresponding G and D modes are shown in Figure 2.2b. The D mode (around 1355 cm^{-1}) is forbidden for perfect graphite and appears only when the material exhibits disorder. Thus, the presence of a distinct D band is usually correlated with a more disordered carbon material. The G-mode (in the range of 1500 - 1630 cm^{-1}) is related to the in-plane bond-stretching motion of pairs of C sp^2 carbon atoms and is allowed for perfect graphite. Thus, its appearance is usually correlated with less disorder in the carbon material. However, the G mode does not require the presence of sixfold rings and occurs at all sp^2 sites, e.g. in chains [22].

Tuinstra and Koenig correlated the ratio of these two Raman bands

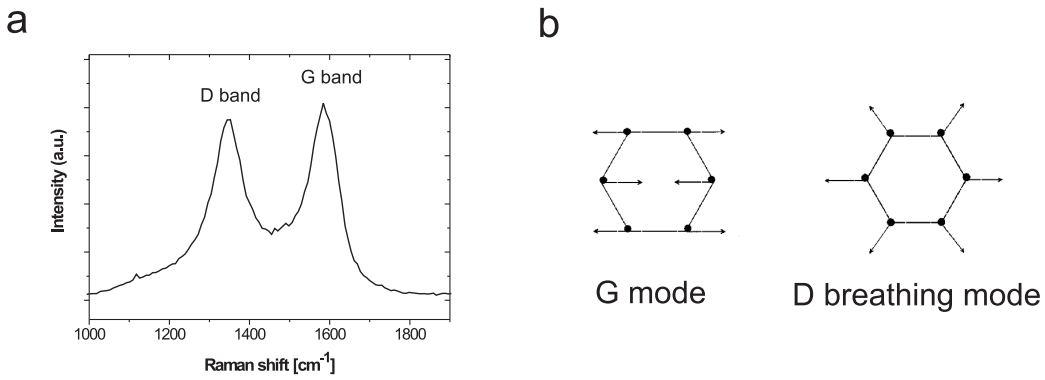

Figure 2.2: *(a)* Typical Raman spectrum of non-graphitic carbon and *(b)* Carbon motions in the different modes (picture taken from Ref. [22]).

with the layer size L_a of the graphenes by the following equation [23]:

$$\frac{I(D)}{I(G)} = \frac{C(\lambda_L)}{L_a} \tag{2.13}$$

FERRARI AND ROBERTSON proposed a modified equation for layer sizes below ∼2 nm [22] :

$$\frac{I(D)}{I(G)} = C'(\lambda_L) L_a^2 \tag{2.14}$$

where I(D)/I(G) is the band intensity ratio, $C(\lambda_L)$ and $C'(\lambda_L)$ wave-length depending pre-factors and L_a the layer size. The absolute values of the pre-factors can be calculated according to MATTHEWS ET AL. [24]

$$C(\lambda_L) \approx c_0 + \lambda_L c_1 \tag{2.15}$$

(3) with c_0 = -12.6 nm and c_1 = 0.033.

One drawback using these formulas is that the determination of the intensity ratio I(D)/I(G) varies in literature. Usually, band heights, band widths or integrated band areas are used for this purpose. Thereto, the experimental data is fitted with profile shape functions. For example, Gaussian, Lorentzian, Breit-Wigner-Fano or pseudo-Voigt functions are commonly used. Also, the number of functions applied (two or multi-peak fit) varies in

literature [25].

2.3 Nitrogen sorption

Nitrogen sorption is a widely used technique for the characterization of porous materials. Adsorption is defined as the enrichment of one or more components in an interfacial layer. The vice versa process is called desorption. The adsorption process is classified into *chemisorption* (adsorption involving chemical bonding) and *physisorption* (adsorption without chemical bonding), whereas the latter process is usually used for adsorption experiments, using different gases such as nitrogen, carbon dioxide or krypton as adsorptive. Physisorption, in contrast to chemisorption, has the advantage to happen comparably fast, allows multilayer formation and is in most cases a reversible process.

The basic principle of this method is that the amount of adsorbed molecules correlates with the surface area and porosity of the material. In a typical experiment, the total amount of adsorbed gas is measured as a function of the relative pressure p/p_0, while keeping the temperature T constant. p_0 is the saturation vapour pressure of the gas at the temperature T. The resulting curves are called *physisorption isotherms*, consisting of an adsorption and a desorption branch. Figure 2.3 shows six main types of physisorption isotherms, according to the IUPAC classification. Type I is typically for microporous materials. A steep increase at low relative pressures is followed by a plateau. Pores of molecular dimensions show enhanced interactions with the gas and are therefore filled at small values for p/p_0. Once the pores are filled, the isotherm reaches the horizontal plateau indicating a very small external surface area. Type II is typically found for nonporous (or macroporous) materials. The point B indicates the completion of the monolayer. At higher pressures, adsorption continues with the formation of more layers. Isotherms of type III and V exhibit convexity towards the relative pressure axis and are characteristic of weak gas-solid interactions. Similar to type II isotherms, type III isotherms are found for nonporous (and macroporous) materials. Type IV (and V) isotherms show a hysteresis loop, i.e. adsorption

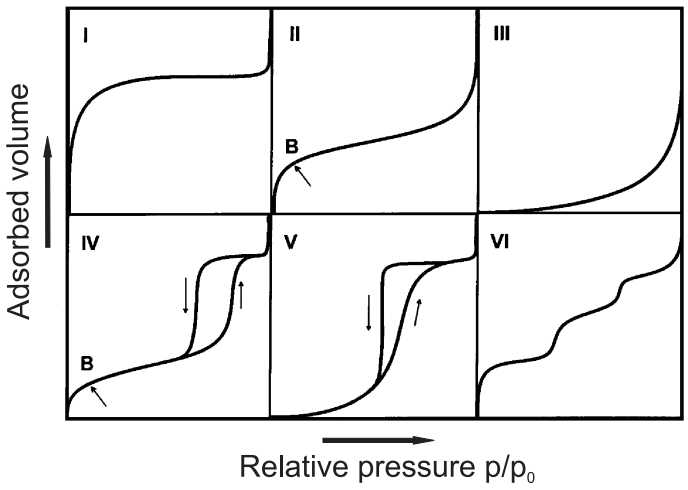

Figure 2.3: The six main types of gas physisorption isotherms, according to the IUPAC classification [26].

and desorption branch do not show an identical curve progression. The steep increase of the curve is usually associated with the presence of mesopores that are filled by capillary condensation. The curve reaches a plateau, when all mesopores are filled. During desorption, the pores empty at lower relative pressures. The shape of the hysteresis loop can give useful indications about the pore structure (e.g. pore shape, uniformity, interconnectivity) but interpretations are difficult and still under discussion, since most mesoporous materials posses complex pore networks of irregular size and shape. In this work, mainly type IV isotherms were found for the synthesized material. Type VI isotherms are seldomly found and represent the step-wise multilayer adsorption on a homogeneous nonporous solid [26–28].

2.3.1 Classical analysis

Various mathematical models were developed to calculate key parameters such as surface area and pore size distribution from the physisorption isotherms. While all sorption models are based on certain assumptions and simplifications, the resulting values have to be carefully interpreted. Especially the classical theories are based on simple, but straight forward models and are still commonly used. The two most prominent classical models for

determination of surface area (BET model, 1938) and pore size distribution (BJH model, 1951) are introduced in the following.

The Brunauer-Emmett-Teller (BET) [29] theory results into the equation

$$\frac{p/p_0}{n(1-p/p_0)} = \frac{1}{n_m C} + \frac{C-1}{n_m C}(p/p_0) \tag{2.16}$$

with the total amount of adsorbed molecules n and the monolayer capacity n_m. C is correlated with the adsorption- and condensation enthalpies. As two important assumptions, the model implies that all adsorption sites for multilayer adsorption are of the same energy and all layers after the first one show liquid-like properties. A straight line is gained by plotting the left side of the equation against p/p_0 (usually in the range between $p/p_0 = 0.1$ - 0.35). n_m and C can be derived from the ascending slope and the axis intercept, respectively. The specific surface area can be calculated from n_m by assuming an average area σ that each adsorbed molecule occupies on the surface. Besides the before mentioned assumptions, the exact value of σ is not accurately known and still under discussion [30,31]. Usually, values for σ around 0.162 nm^2 are assumed for the adsorption of nitrogen. Furthermore, the presence of micropores can strongly affect the results obtained by the BET theory since the model does not account pore filling at low relative pressures.

The classical models of calculating mesopore size distributions are based on the *Kelvin equation*, with the most famous one developed by Barrett, Joyner and Halenda (BJH model) [32]. The BJH model uses the (modified) Kelvin equation as the mathematical expression for the observation that the gas condensates in the pores before reaching its saturation pressure p_0,

$$r_p(p/p_0) = \frac{2\gamma V_m}{RTln(p_0/p)} + t(p/p_0) \tag{2.17}$$

with γ and V_m as surface tension and the molar volume of the liquid, r_p the pore radius and R, the universal gas constant. Besides the presence of cylindrical pores, the model assumes physisorption on the pore walls prior to the condensation. The thickness of the physisorbed film before condensation

is t. However, three main concerns question the validity of this formula [26, 33–35]. Firstly, the exact relation between the meniscus curvature and the pore size, especially when the pore shape does not resemble a cylinder. Secondly, the validity of the formula for smaller mesopores and thirdly, the assumed constancy of the surface tension that probably varies with the pore diameter.

The total pore volume can be obtained by the amount of gas adsorbed at the plateau, provided that the condensate has the same density as bulk liquid at the same temperature.

2.3.2 Advanced analysis - Non-local density functional theory (NLDFT)

Non-local density functional theory (NLDFT) is a more modern approach that resolves many of the aforementioned concerns. In contrast to the "macroscopic" approaches described above that fail on the molecular level, NLDFT models describe the local structure of the fluid close to the curved solid pore walls. Thereto, adsorption isotherms in model pores (e.g. cylindrical, spherical or slit shape) are calculated based on the intermolecular fluid-fluid and solid-fluid interactions.

A *generalized adsorption isotherm* (GAI) can be formulated, assuming that an experimental isotherm consists of a large number of individual "single pore" isotherms weighted by their relative distribution:

$$N(p/p_0) = \int_{W_{min}}^{W_{max}} N(p/p_0, W)\, f(W)\, dW \tag{2.18}$$

where $N(p/p_0)$ = experimental adsorption isotherm data, W = pore width, $N(p/p_0, W)$ = isotherm of a single pore of width W, and $f(W)$ = pore size distribution function.

The set of $N(p/p_0,W)$ isotherms for a given adsorbate/adsorbent system can be determined by (non-local) density functional theory ((NL-)DFT). The pore size distribution is then derived by solving the GAI equation numerically.

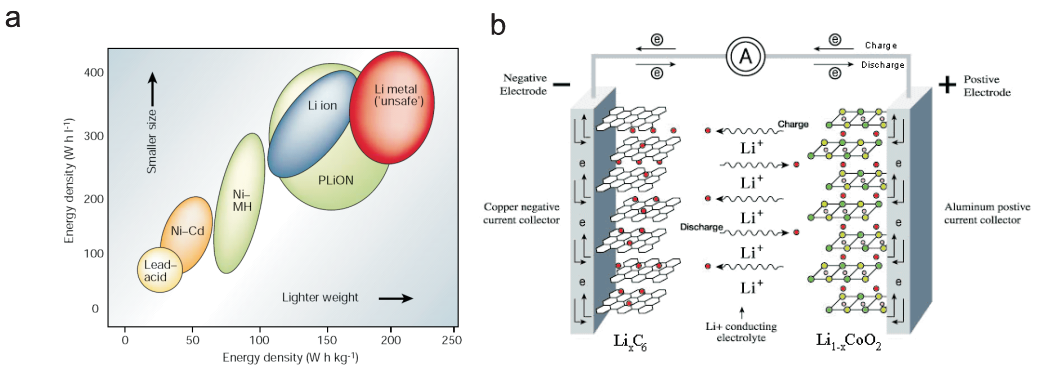

Figure 2.4: *(a)* Energy densities of different battery types expressed in units of weight (Wh kg^{-1}) and of volume (Wh l^{-1}). *(b)* Typical assembly of a lithium ion battery. (Picture *(a)* taken from Ref. [38])

Due to the molecular approach, much more accurate results for the pore size distribution can be obtained by NLDFT models compared to classical methods. In particular, NLDFT models are necessary for the correct investigation of micro- and mesoporous materials. The current NLDFT models for nitrogen are usually applicable for pore sizes between 0.35 - 100 nm [36,37].

2.4 Li insertion / extraction measurements on carbon materials

The total amount of electrical energy that can be stored in a battery is mainly determined by the cell potential (V) and the capacity (mA h g^{-1}). Figure 2.4a shows the energy densities for different battery types that are currently used. Clearly, lithium based batteries show the highest energy densities, mainly due to the fact that lithium is the lightest metal (0.53 cm^3 g^{-1}) and shows the highest electrochemical potential (-3.04 V versus the standard hydrogen electrode). However, the development of rechargeable lithium batteries failed due to safety problems caused by the inherent reactivity of the metal and dendrite formation during cycling. Therefore, lithium ion batteries were developed, substituting metallic lithium by lithium compounds.

The functional principle of a lithium ion battery is based on two electrodes

that can reversibly intercalate lithium ions. Figure 2.4b shows the typical assembly a state of the art lithium ion battery. Graphite is used as negative, an inorganic transition metal oxide (usually $LiCoO_2$ or $LiMn_2O_4$) as the positive electrode material. Both electrodes are separated by a membrane that is soaked in a Li^+ conducting electrolyte (e.g. $LiPF_6$ in a mixture of organic solvents). During the first charge, Li^+ ions are extracted from the transition metal oxide and are inserted between the graphite layers. The opposite process happens during discharge.

For graphite, one Li^+ ion per six carbon atoms can be stored at maximum, forming the compound LiC_6. During insertion, the distance between the graphite layers slightly increases around 10% [39]. The formation of LiC_6 gives rise to a theoretical capacity of 372 mA h g^{-1} for the graphite electrode. The electrochemical reactions are as follows:

$$\text{Positive electrode: } LiMO_2 \rightleftharpoons Li_{1-x}MO_2 + x\ Li^+ + x\ e^-$$
$$\text{Negative electrode: } y\ C + x\ Li^+ + x\ e^- \rightleftharpoons Li_xC_y$$
$$\textit{Overall : } LiMO_2 + y\ C \rightleftharpoons Li_{1-x}MO_2 + Li_xC_y$$

However, higher charge capacities are found for other kinds of carbon materials ("high specific charge carbons"), in particular carbonaceous and non-graphitic carbon materials ($\approx$ 400 - 1000 mA h g^{-1}) [40]. The explanation of such high charge capacities is still under discussion and several mechanisms have been suggested. Some of the mechanisms are shown in Figure 2.5. As described, in graphite the lithium ions are only inserted between the graphite layers (Fig. 2.5a, *Note:* The layer size of graphite is much larger compared to the other carbon materials). Looking at carbon materials of small particle size, additional lithium can be stored on the graphene edges and surfaces (Fig. 2.5b) [41]. Other models propose that additional lithium can be stored in nanoscopic cavities or by $Li \bullet\bullet\bullet H \bullet\bullet\bullet C$ interactions (Fig. 2.5c and d) [42]. In particular, it is still under discussion, whether lithium ions can be inserted between the graphene layers only in graphite or also in non-graphitic carbon materials [40–42]. Despite the higher capacity

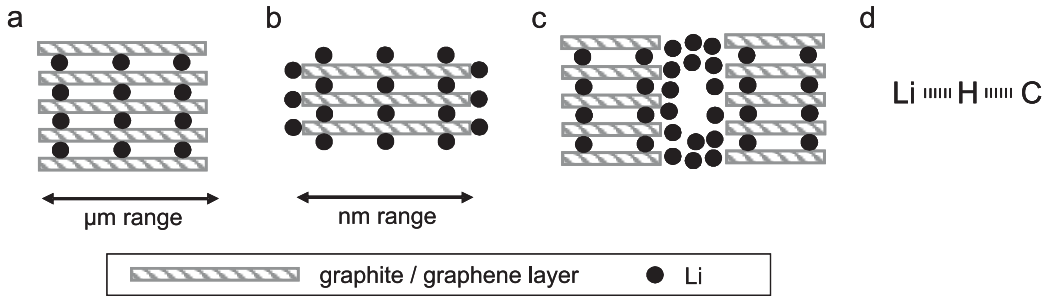

Figure 2.5: Schematic drawings of some proposed mechanisms for the storage of lithium in carbon materials. Redrawn from Ref. [40].

of non-graphitic or carbonaceous materials, graphite is still the commonly used electrode material, because high specific charge carbons show certain disadvantages e.g. poor cycling performance [40].

An important phenomenon that occurs during the first battery cycles is the formation of a thin layer on the electrode surface. Lithium is very reactive and reacts with the electrolyte to form (mostly insoluble) Li salts that deposit on the carbon electrode surface. This effect is known as the "solid electrolyte interphase (SEI) formation". The SEI formation originates from electrolyte reduction at low voltage (e.g. 0.8 V vs. Li/Li^+ for ethylene carbonate). The SEI passivizes the carbon electrode and thus prevents further growth of the layer. The SEI is electronically insulating, but ionically conductive, i.e. the Li ions can easily migrate through the whole layer. The components of the SEI include e.g. Li_2CO_3 or lithium alkyl carbonate and volatile compounds can occur during their formation. Depending on its structure, the SEI strongly influences the battery performance and numbers of electrolyte additives are available in order to influence its formation [43, 44].

A battery can be charged and discharged at different rates, i.e. currents. These rates are given as "C-rates", where C is the capacity of the battery in Ah.[1] A discharge rate of 1C means that the battery is discharged at the same rate as its capacity. For example, a battery with a capacity of 1000 mA h provides 1000 mA for one hour if discharged at 1C. The same battery discharged at C/2 would last two hours, providing 500 mA. A rate of 60C

[1] The unit of the capacity of the electrode material is usually given in mA h g^{-1}.

means charging / discharging in one minute. Of course, it is desirable to develop batteries that can be charged at high C-rates. However, the insertion process of Li ions in the carbon electrode is slower than the extraction process [45, 46]. Thus, lithium ion batteries are usually charged at low C-rates and charging times are comparably long.

Important parameters that determine the performance of a rechargeable battery are:

- specific charge capacity [mA h g^{-1}] –> maximum energy that can be stored
- cyclability, reversibility —> lifetime
- rate performance —> charging and discharging times
- voltage —> cell potential

2.5 Electron microscopy (EM)

Electron microscopes are scientific instruments that use a electron beam to examine objects on a very fine scale. EM can give information about the topography and morphology of a sample as well as its composition and crystallography. The resolution d (the ability to discriminate between two points) of a perfect microscope is limited by the *Abbe equation*

$$d = \frac{\lambda}{2n \sin \alpha} \tag{2.19}$$

with the wavelength λ, index of refraction n and α the half aperture angle in radians. In general, this equation limits the resolution of light microscopy (LM) to around 500 nm. A much better resolution can be obtained by using electrons instead of visible light as imaging radiation. De Broglie proposed that moving particles have wave-like properties and their wavelength can be calculated as follows,

$$\lambda = \frac{h}{m\nu} \tag{2.20}$$

with the Planck's constant h, the particle mass m and the velocity of the particle ν. In an electric field, the electron velocity can be expressed by the voltage field V that accelerates the electrons and the formula for λ can be expressed as

$$\lambda = \frac{1.226}{\sqrt{V}}\, nm \tag{2.21}$$

The basic steps in EM (regardless the type) are: *(1)* Electrons are generated and accelerated towards the sample (electrons that are accelerated by a voltage field of 100 kV have a wavelength of around 0.0039 nm). *(2)* Metal apertures and magnetic lenses are used to focus the electron beam onto the sample. *(3)* The electron beam and the sample interact with each other. *(4)* The interactions are detected and transformed into an image.

The use of electrons requires magnetic lenses in EM instead of optical lenses in LM to direct the imaging radiation. Each lens and aperture has its own set of aberrations and distortions that determine the practical limit of the resolution in electron- and light microscopy. Instruments used in EM have to be carefully evacuated because the electrons are otherwise scattered by the air. The two major types of microscopes used in EM are scanning- and transmission electron microscopes.

Scanning electron microscopy (SEM) uses the scattering of electrons from the sample surface revealing the samples surface topography and morphology. In a typical SEM, the electron beam is focused into a spot of around 1-5 nm in size. The spot is directed over the specimen in a raster fashion whereas the electrons interact with the sample surface, emitting secondary electrons (SE). These electrons are comparatively slow and are deflected from the sample by a weak electric field. The deflected SE are then accelerated by an amplifier and detected by a electron multiplier representing the sample topography. Edges within the sample facilitate the release of SE and appear more bright, making the observed picture spacial and rich in contrast. The yield of SE also depends on the material, making it possible to distinguish

between different phases or crystallographic orientations. Since SE are easily to detect, the intensity of the primary electron beam can be low, preventing the sample from thermal damage. Non-conducting samples have to be coated with a conductive material (usually gold) since the electron beam charges the sample negatively.

A higher resolution can be obtained using transmission electron microscopy (TEM). Here, the electron beam passes through the sample, requiring the preparation of very thin samples. TEM works similar to slide projection, where a light beam transmits a slide and is affected by the picture on the slide. The transmitted beam is then projected onto a big screen, forming an enlarged image. In TEM, the electrons either pass the sample or can be absorbed or scattered by the atoms. The instrument can be then operated in two modes. In the *image mode*, the scattered electrons are suppressed by an aperture under the sample. Only the non-affected electrons pass the further lenses that enlarge the beam and create a magnified image of the sample. The absorption and scattering increases with the sample thickness and the atomic number. Pores, for example, do not absorb electrons and appear darker on the magnified image. Elements of higher atomic numbers, like iron, appear lighter. The elastic scattered electrons are used in the *diffraction mode* to obtain diffraction patterns of the observed spots. Besides the higher resolution, the main advantage of TEM is the possibility to switch between image and diffraction mode. For example, the image mode can be used to observe nanocrystals in a matrix, whereas the diffraction mode can reveal their crystal structures [5, 47].

High-resolution transmission electron microscopy (HRTEM) allows the examination of structures even smaller than 1Å. Such a high magnification allows the visualization of graphite layers, for example. The technique of HRTEM is often accompanied by electron energy loss spectroscopy (EELS) that provides information about the bonding type of the atoms.

Chapter 3

WAXS Modeling of Non-graphitic Carbons - An Evaluation of Different Carbon Precursors

3.1 Introduction

The properties of a carbon material are mainly determined by the carbon microstructure itself. In the following, the term *carbon microstructure* refers to the molecular arrangement of the carbon atoms, in particular bonding type (sp^2 or sp^3) and size and shape of the structural units (polyaromatic ring systems, called "graphenes"). For example, electrical and thermal conductivity, hardness, Young's modulus, thermal expansion, density, resistance to corrosion or the micropore content are directly related to the carbon microstructure. Even when the bonding type is identical, the arrangement of the graphenes can give rise to very different properties. For example, glassy carbons consist of sp^2-bonded carbon atoms like graphite, but the material is harder and shows a much better resistance to corrosion.

Obviously, an exact knowledge of the carbon microstructure is desirable for the development of new carbon materials and the tuning of their properties.

Generally, carbon materials are obtained by a suitable heat treatment

(carbonization) of a carbon precursor. In this chapter, the influence of carbon precursor and heat treatment temperature (HTT) on the resulting carbon microstructure are studied in detail. Thereto, five different carbon precursors were heat treated at different temperatures between 700 and 1500 °C: A disaccharide (sucrose, SUC), a polysaccharide (starch, STA), furfuryl alcohol (FA), naphthol (NA) and mesophase pitch (MP).

The most common techniques used for the determination of the carbon microstructure are wide-angle x-ray scattering (WAXS) and Raman spectroscopy. As described in Chapter 2.1 and 2.2, the evaluation of the experimental data is, in both cases, difficult and thus, a novel model (in the following denoted as WAXS model) was applied in order to interpret the WAXS pattern in a more accurate way. The model, developed by Ruland and Smarsly [11], is based on relevant structural parameters that allow a precise determination of the carbon microstructure (Chapter 2.1.2 on page 17). For the first time, the model was applied on a larger series of samples that exhibited very different carbon microstructures. The results of the WAXS model are also compared with the results that are obtained by Raman spectroscopy.

3.2 Carbonization and non-graphitic carbon

The two most important parameters that determine the microstructure of a carbon material are the *heat treatment temperature HTT* (carbonization temperature) and the choice of the *carbon precursor*. Carbonization is defined by IUPAC as a process "by which solid residues with increasing content of the element carbon are formed from organic material usually by pyrolysis in an inert atmosphere." Figure 3.1a illustrates the the changes in the carbon microstructure with increasing HTT. At relatively low temperatures, the structure is very "disordered". With increasing temperature, the structure arranges to form units that consist of parallel aligned graphene sheets (*graphene stacks*). At temperatures higher than 2500 °C, the structure transforms into the thermodynamically stable form: graphite.

Various terms are used to describe carbon materials of different mi-

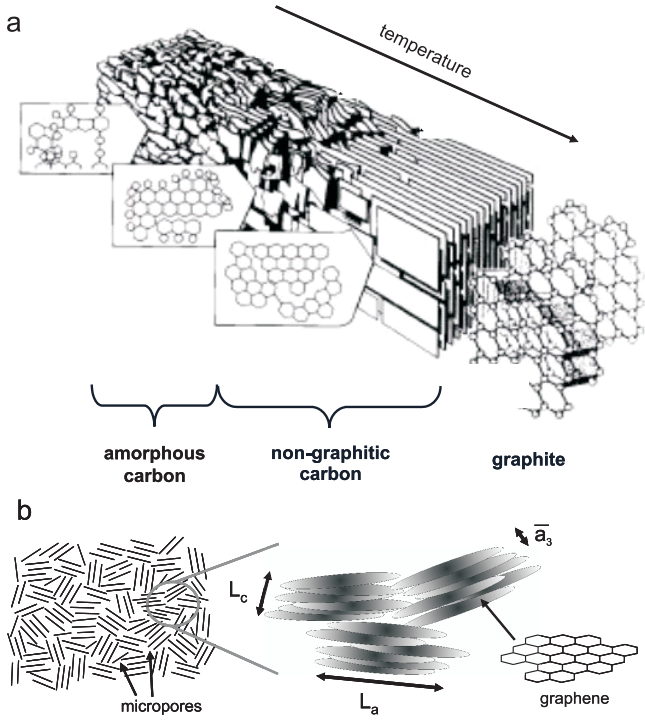

Figure 3.1: *(a)* Changes in the carbon microstructure during carbonization. Picture taken from [6] *(b)* Sketch of the carbon microstructure from a non-graphitic carbon.

crostructure, however they are often applied in an inaccurate fashion. The IUPAC definitions of the most relevant terms are given as follows [48]:

- *Graphite*: An allotropic form of the element carbon consisting of layers of hexagonally arranged carbon atoms in a planar condensed ring system (graphene layers). The layers are stacked parallel to each other in a three-dimensional crystalline long-range order. There are two allotropic forms with different stacking arrangements, hexagonal and rhombohedral. The chemical bonds within the layers are covalent with sp^2 hybridization and with a C-C distance of 141.7 pm. The weak bonds between the layers are metallic with a strength comparable to van der Waals bonding only.

- *Graphitic carbon*: All varieties of substances consisting of the element carbon in the allotropic form of graphite irrespective of the presence

of structural defects. *Note:* The use of the term graphitic carbon is justified if three-dimensional hexagonal crystalline long-range order can be detected in the material by diffraction methods, independent of the volume fraction and the homogeneity of distribution of such crystalline domains. Otherwise, the term non-graphitic carbon should be used.

- *Non-graphitic carbon*: All varieties of solids consisting mainly of the element carbon with two-dimensional long-range order of the carbon atoms in planar hexagonal networks, but without any measurable crystallographic order in the third direction (c-direction) apart from more or less parallel stacking. *Note:* Some varieties of non-graphitic carbon convert on heat treatment to graphitic carbon (graphitizable carbon) but some others do not (non-graphitizable carbon).

- *Amorphous carbon*: A carbon material without long-range crystalline order. Short-range order exists, but with deviations of the interatomic distances and/or interbonding angles with respect to the graphite lattice as well as to the diamond lattice. *Note:* The term amorphous carbon is restricted to the description of carbon materials with localized π-electrons as described by P.W.Anderson (Phys. Rev., 1958, 109, 1492). Deviations in the C-C distances greater than 5% (i.e. $\frac{\Delta x}{x_0} > 0.05$, where x_0 is the inter-atomic distance in the crystal lattice for the sp^2 as well as for the sp^3 configuration) occur in such materials, as well as deviations in the bond angles because of the presence of 'dangling bonds'. The above description of amorphous carbon is not applicable to carbon materials with two-dimensional structural elements present in all pyrolysis residues of carbon compounds as polyaromatic layers with a nearly ideal interatomic distance of a = 142 pm and an extension greater than 1000 pm.

The carbon materials examined in this work were all so-called *non-graphitic carbons*. Fig 3.1b shows a sketch of the typical microstructure found for non-graphitic carbons. Single graphene layers are aligned to stacks that are

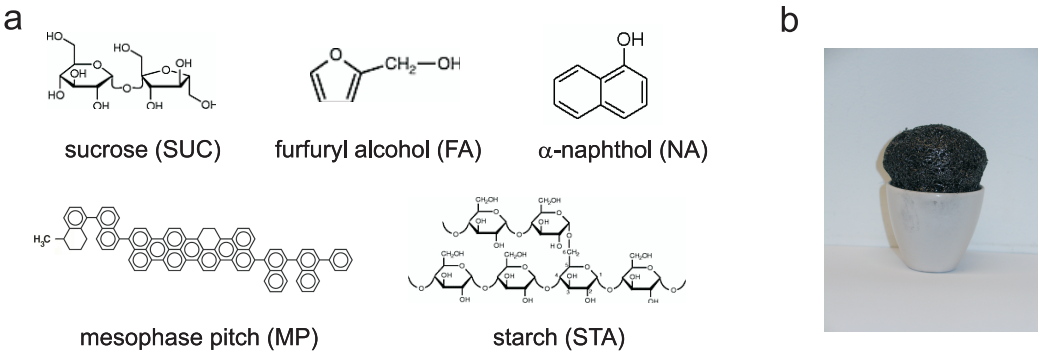

Figure 3.2: *(a)* Chemical structure of the investigated carbon precursors. *(b)* Mesophase pitch after carbonization at 700 °C.

randomly distributed. The key parameters that describe the microstructure are the *average layer size* L_a, the *average stack height* L_c, and the *average interlayer spacing* $\overline{a}_3$.

Here it is important to note, that each graphene and thus the stacks can be of random size and shape. Intrinsic defects in the stacking (gaps or "mis-fits" between the stacks and graphene layers) can lead to microporosity (pore diameter < 2 nm). Obviously, a material with small values for L_a and L_c exhibits more microporosity compared to a material with larger values. Thus, the micropore content is strongly influenced by the choice of the carbon precursor and the carbonization procedure.

The structure of the carbon precursors investigated in this work are shown in Figure 3.2a. Sucrose (SUC), furfuryl alcohol (FA) and starch (STA) were chosen, because they are widely used in the synthesis of mesoporous carbon materials (Chapter 4). Naphthol (NA) and mesophase pitch (MP) were chosen, because they exhibit a high carbon content and already consist of six-fold rings. Furthermore, mesophase pitch exhibits large pre-condensed aromatic systems that transform more easily into non-graphitic carbon than other precursors. A catalyst was required for precursors that otherwise would have been completely decomposed.

Table 3.1 shows the composition of the precursors and their weight loss

	Formula	C [wt%]	H [wt%]	O [wt%]	Weight loss in wt% during carbonization
Mesophase pitch	$C_{91}H_{60}$	94.8	5.2	0	21.9
Furfuryl alcohol*	$C_5H_6O_2$	61.2	6.2	32.6	86.7
Sucrose	$C_{12}H_{22}O_{11}$	42.1	6.5	51.4	75.0
Naphthol*	$C_{10}H_8O$	83.3	5.6	11.1	∼75
Starch	$(C_6H_{10}O_5)_n$	44.4	6.2	49.4	76.6

Table 3.1: Different carbon precursors and their weight loss during carbonization. The samples were heat treated for 6h at 700 °C under nitrogen atmosphere (6h heating ramp). * carbonization was activated by a catalyst: Oxalic acid for furfuryl alcohol and sulfuric acid for naphthol.

during carbonization at 700 °C. SUC, FA, STA and NA carbonize under a huge weight loss since they contain a considerable amount of oxygen and hydrogen atoms. In comparison, the weight loss during the carbonization of mesophase pitch is rather small, due to the structure and the comparably high carbon content of MP.

The weight loss during carbonization is attributed to the release of volatile compounds such as hydrocarbons (in particular methane), hydrogen or carbon monoxide [49,50]. Usually this volatile compounds give rise to the development of a voluminous carbon material, as can be seen in Fig. 3.2b. This behavior is expectable and was found for all carbon precursors investigated.

The carbonization process can be also strongly influenced by the addition of catalysts. The advantage of oxalic acid and sulfuric acid is that they result into minor contamination of the resulting material.

Common catalysts for pitches are *Lewis acids* such as $ZnCl_2$, $AlCl_3$ or $FeCl_3$. It was shown that these catalysts can influence the formation of the volatile hydrocarbons and especially shift the dehydrogenation process towards lower temperatures [51, 52].

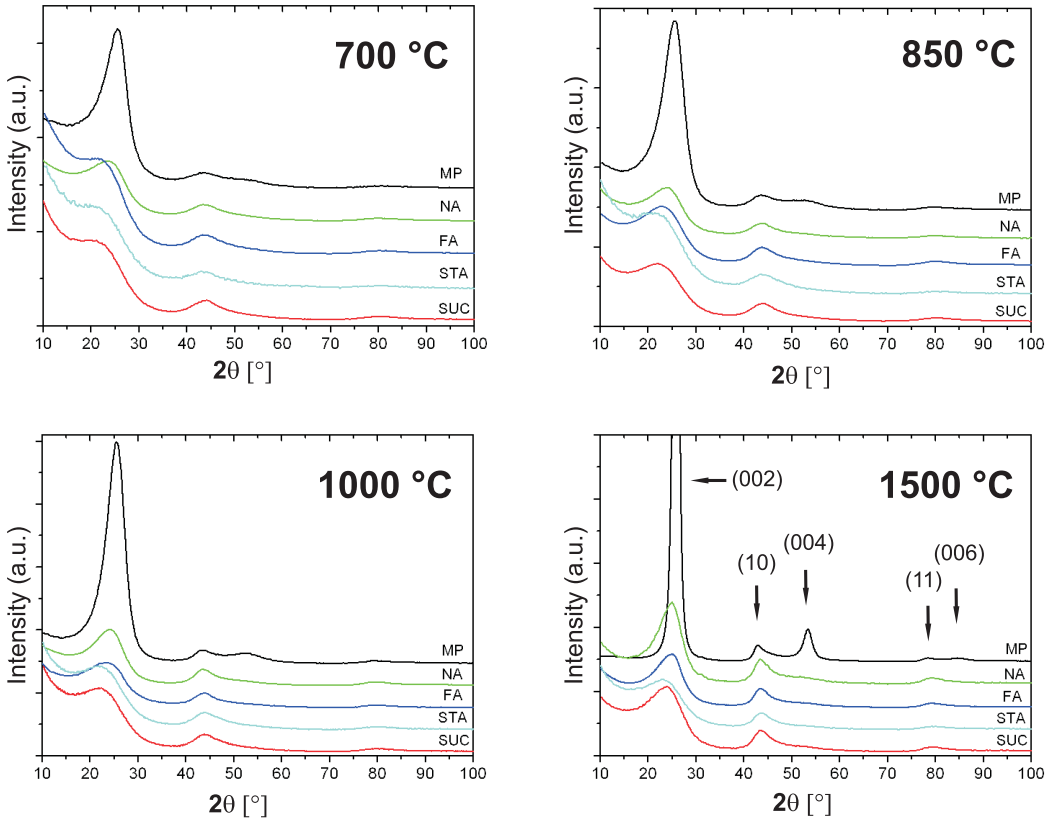

Figure 3.3: WAXS pattern for samples carbonized at different temperatures. MP: mesophase pitch, NA: naphthol, FA: furfuryl alcohol, STA: starch, SUC: sucrose.

3.3 Wide angle x-ray scattering (WAXS)

The WAXS patterns of the different samples are shown in Figure 3.3. As described in Chapter 2.1.2, the WAXS patterns of non-graphitic carbons show relatively broad maxima. The interlayer scattering gives rise to (00l), the intralayer scattering to (hk) reflections.

The shape of the WAXS patterns give already some qualitative information about the carbon microstructures. Obviously, MP based samples show more defined and intense (002) reflections compared to the samples, speaking for higher L_c values or less disorder already at a lower heat treatment temperature (HTT). The other carbon precursors show only weak (002) re-

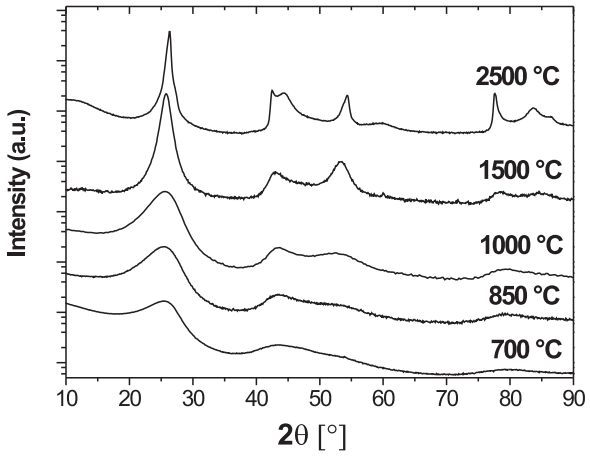

Figure 3.4: WAXS patterns of MP based samples heat treated at different temperatures until graphitization.

flections that slowly develop from a shoulder (700 °C) to a broad peak (1500 °C).

Only small differences can be seen for the (hk) reflections, supposing similar values L_a for all precursors. As expected, the carbon precursors have in common that all reflections get more defined with increasing HTT. This clearly proves that the stacks grow in both dimensions (parallel and perpendicular to the graphenes) during the carbonization process, and a higher HTT gives rise to larger stacks.

Figure 3.4 shows the change in the WAXS pattern as a function of the HTT until graphitization at 2500 °C. At this temperature, the material starts to transform into graphite and thus, additional reflections occur in the WAXS pattern.

The quantitative analysis of the WAXS patterns is presented in the following chapters. Here it should be pointed out that the classical analysis of a WAXS pattern using the *Scherrer equation* is obviously not applicable because the reflections are to broad and cannot be separated unambiguously.

3.4 Modeling of WAXS patterns

Figure 3.5 shows three WAXS patterns and the corresponding fit obtained by the model from Ruland and Smarsly (Chapter 2.1.2).[1] Samples were denoted as "XY" with "X" representing the carbon precursor and "Y" being the HTT (carbonization temperature). MP1500, FA850 and SUC700 were chosen as representative examples since they strongly differ in their WAXS patterns (Note: The scale of the y-axis is logarithmic for the MP1500 sample). The WAXS patterns and corresponding fits of the other samples are shown in Chapter 7.2 on page 121).

The patterns could be well approximated, proving that the model is applicable for non-graphitic carbons of quite different microstructures.

As an important finding, the data could be fitted over a large angular range between 2θ = 10° - 100°, revealing that the carbon microstructure is well described by the assumptions made in the WAXS model. Also, the successful fitting of the WAXS patterns from SUC700 and FA850 prove that the model is applicable even for very disordered carbon materials.

3.4.1 Stack height L_c, layer size L_a and interlayer spacing $\overline{a}_3$

Figure 3.6a shows the change in the stack height L_c with the HTT for the different carbon precursors.

The largest values for L_c were found for the MP samples. Also, the strong increase of L_c from 0.98 nm (700 °C) to 7.38 nm (1500 °C) shows that the stacks significantly grow with increasing HTT. The other samples (NA, FA, STA and SUC) show only small absolute values for L_c ($<$ 0.8 nm even at 1500 °C), speaking for a very disordered carbon microstructure. In this case, the graphenes are of very different sizes and shapes, often interconnected by covalent bonds that hinder the alignment of single graphenes. Starch heat treated at 700 °C shows a comparably large value for L_c, which can partly be

[1] The shift in θ produced by the finite penetration of the primary beam into the sample was corrected using the correction from Keating & Warren, 1952.

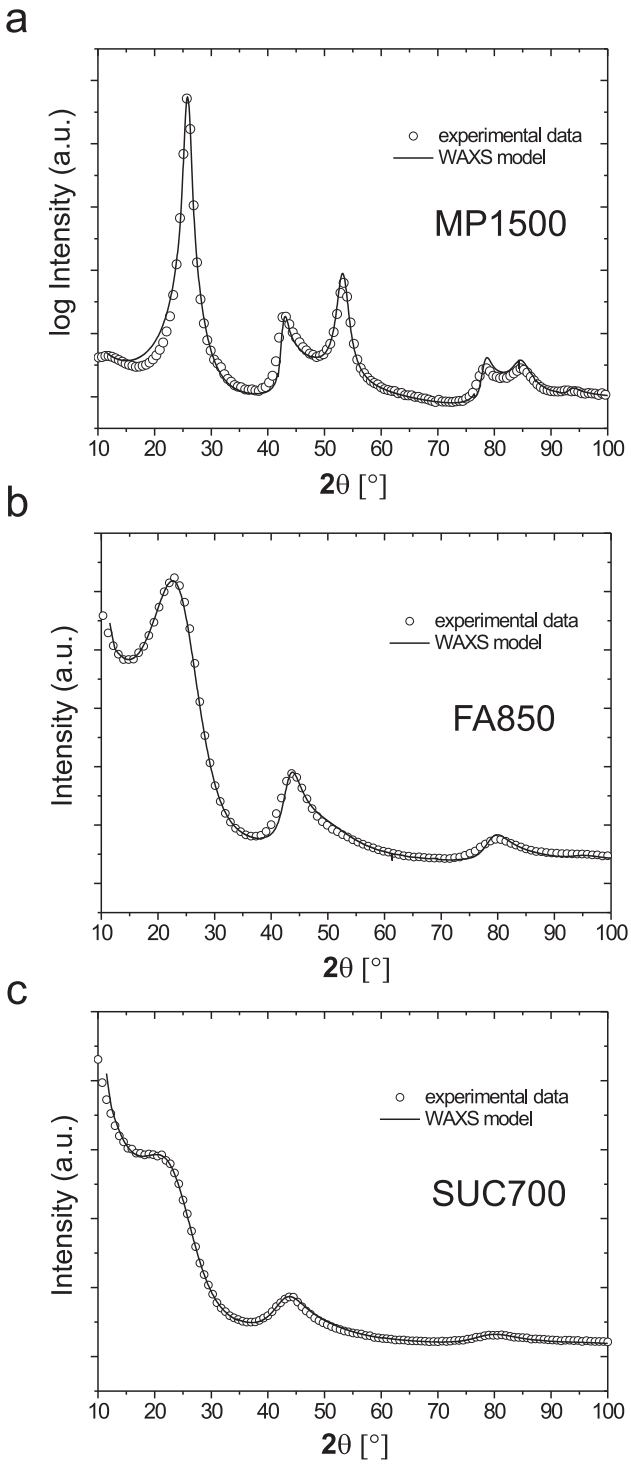

Figure 3.5: WAXS model and experimental data of *(a)* MP1500 and *(b)* FA850 and *(c)* SUC700.

attributed to the large interlayer spacing found for this sample ($\overline{a}_3 = 0.386$ nm). At higher HTT, STA samples show more or less constant values smaller than 0.5 nm for L_c, making starch in this respect the worst carbon precursor.

The average interlayer spacing $\overline{a}_3$ of the different samples is shown in Figure 3.7a. Samples from MP show slightly smaller values for the average interlayer spacings $\overline{a}_3$ compared to the other samples, speaking for the good carbonization behavior and the presence of more regularly aligned graphene sheets. For comparison, the interlayer spacing of graphite ($\overline{a}_3 = 0.335$ nm) is added to the graph. The changes in $\overline{a}_3$ with HTT were found to be rather small for all samples. Only samples derived from starch showed significantly differing values, probably due to large structural changes in the carbon microstructure during carbonization.

The difference between the carbon precursors is even more obvious comparing the *average number of graphene sheets* $\langle N \rangle$ that form one stack in the resulting carbon material. Considering the samples carbonized at 1500 °C, around 20 graphene sheets form one stack in the MP based carbon material. In contrast, samples from the other carbon precursors showed $\langle N \rangle$ values around one (Fig. 3.7b). Here it should be pointed out that $\langle N \rangle$ is an average value, because at least two graphenes per stack are necessary for constructive interferences. It should be taken into account that the number distributions for N are quite broad so that all samples contain at least some stacks with $N > 2$. The pronounced width of the (002) reflections that is found for all samples (except MP) is therefore partly due to the small number of graphenes per stack. The polydispersities κ_a and κ_c are discussed in Chapter 3.4.3.

Figure 3.6b shows the layer size L_a as a function of the HTT for the different samples. Very similar values of L_a between 1.1 and 1.5 nm were found for all samples carbonized at 700 °C. Samples derived from saccharides (sucrose and starch) exhibited the smallest change of L_a with HTT, speaking for a high degree in structural disorder. Small L_a values were also found for the MP samples at temperatures below 1000 °C. The aromatic moieties of mesophase pitch enable the stacks to grow easily in height, but the evenly distributed electron density within the aromatic layers as well as the lack of

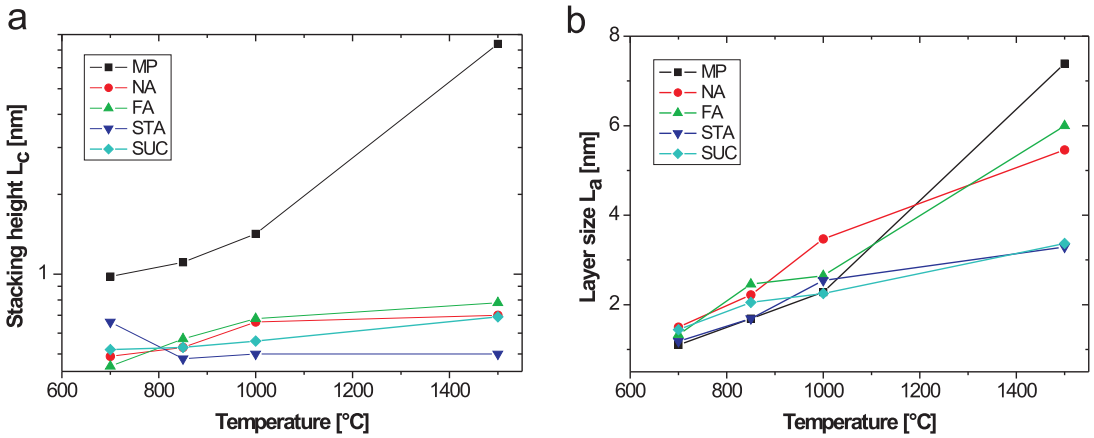

Figure 3.6: Change of *(a)* the average stack height L_c and *(b)* the average layer size L_a as a function of the HTT.

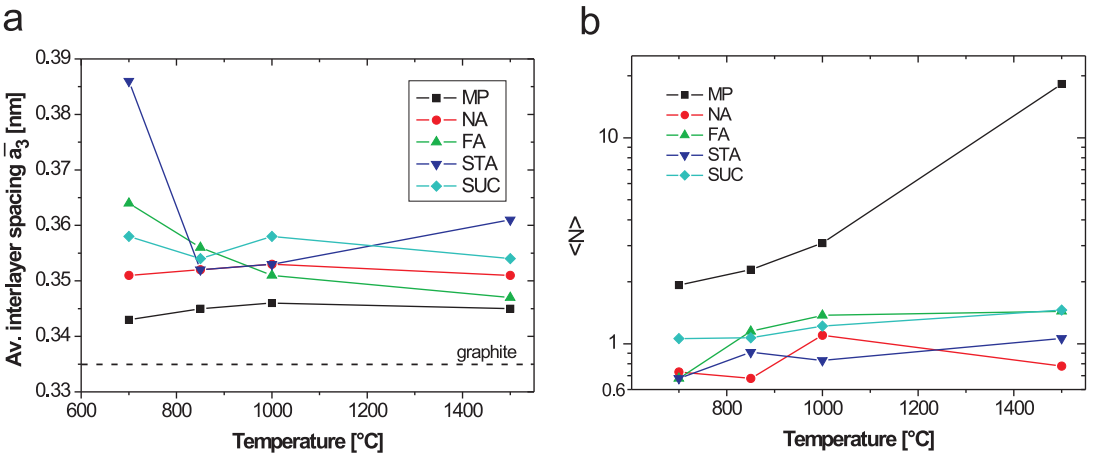

Figure 3.7: *(a)* Change of the average interlayer spacing $\bar{a}_3$ with HTT. *(b)* Average number of graphene sheets $\langle N \rangle$ forming one stack.

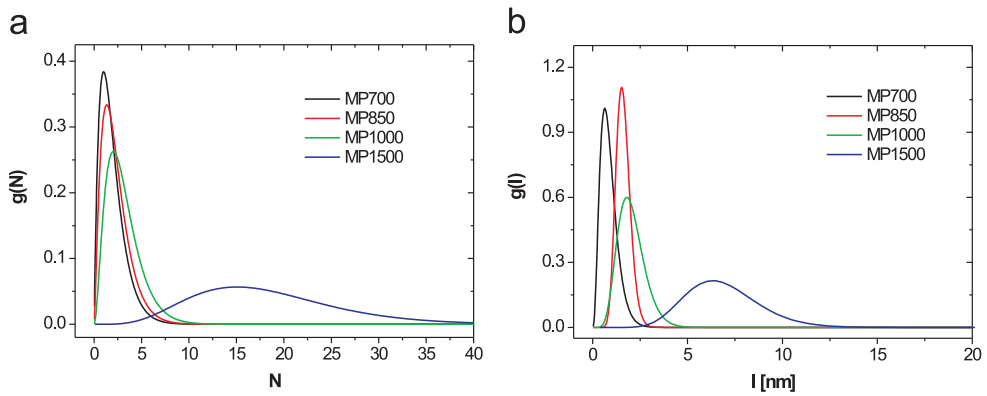

Figure 3.8: Number distribution functions (Gamma distributions) for *(a)* number of graphenes each stack N and *(b)* chord length l for samples from mesophase pitch.

reactive sides probably hinders the layer growth. However, a strong increase in layer size was found when MP was carbonized at 1500 °C.

Comparing the values for L_a and L_c at different HTT, MP and the other precursors show an inverse behavior. For the MP based samples, the stacks grow easier perpendicular to the graphene sheets, whereas carbons from the other precursors grow predominantly within the graphene layer.

The WAXS model also allowed the determination of distribution functions. Figure 3.8 shows the number distribution functions (gamma distributions) of the number of graphenes each stack N and chord length l for samples from mesophase pitch. Since L_c and L_a are average values, the distribution functions give additional information about the true dimensions of the graphene stacks. The broad form of the distributions clearly show that larger graphene stacks are present already at lower carbonization temperatures.

The exceptional carbonization behavior of mesophase pitch (MP) is based on its pre-condensed aromatic systems which can easily transform into non-graphitic carbons with extended stack sizes. Also, the high carbon content and the comparably small weight loss during carbonization facilitate the

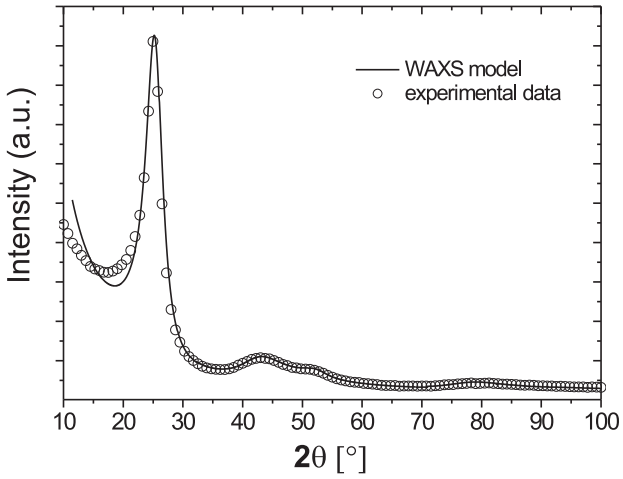

Figure 3.9: WAXS model and experimental data for mesophase pitch before carbonization.

formation of a well-developed carbon microstructure.

The WAXS pattern of mesophase pitch before carbonization is shown in Figure 3.9. Clearly, the pattern resembles the one that is found for non-graphitic carbons, proving that the microstructure of the carbon precursor already shows a distinct graphene structure already before carbonization. This similarity allowed the application of the WAXS model on the carbon precursor itself. The average interlayer spacing $\overline{a}_3$ between the MP molecules was determined to be around 0.35 nm. L_c was found to be around 1.0 nm, and L_a around 1.2 nm.

A summary of the values determined for L_c, L_a and $\overline{a}_3$ is given in Table 3.2.

3.4.2 Texture in non-graphitic carbon from mesophase pitch

The WAXS model assumes diffractometer measurements of flat powder samples in symmetric reflection. If the samples exhibit a texture within the

	L_c [nm]	L_a [nm]	$\overline{a}_3$ [nm]	κ_c	κ_a	l_{cc} [nm]
MP700	0.98	1.1	0.343	0.48	0.26	0.1405
MP850	1.11	1.69	0.345	0.42	0.05	0.1405
MP1000	1.42	2.28	0.346	0.34	0.12	0.1405
MP1500	7.38	7.39	0.345	0.17	0.08	0.1405
$MP_{\text{before carbonization}}$	1.02	1.18	0.35	50	0.28	0.1420
NA700	0.49	1.5	0.351	0.89	0.21	0.1406
NA850	0.53	2.22	0.352	1.22	0.16	0.1404
NA1000	0.66	3.47	0.353	0.70	0.24	0.1402
NA1500	0.7	5.46	0.351	1.56	0.16	0.1404
FA700	0.45	1.33	0.364	0.77	0.24	0.1401
FA850	0.57	2.46	0.356	0.39	0.28	0.1405
FA1000	0.68	2.65	0.351	0.41	0.29	0.1398
FA1500	0.78	6.0	0.347	0.57	0.18	0.1400
STA700	0.66	1.18	0.386	0.60	0.38	0.1399
STA850	0.48	1.69	0.352	0.64	0.26	0.1398
STA1000	0.5	2.54	0.353	0.54	0.16	0.1398
STA1500	0.5	3.29	0.361	1.01	0.11	0.1398
SUC700	0.52	1.44	0.358	0.38	0.23	0.1400
SUC850	0.53	2.05	0.354	0.42	0.19	0.1399
SUC1000	0.56	2.25	0.358	0.30	0.16	0.1402
SUC1500	0.69	3.37	0.354	0.33	0.17	0.1401

Table 3.2: Main results of the WAXS model: Average stack height L_c, average layer size L_a, average interlayer spacing $\overline{a}_3$, polydispersity of stack size κ_c, polydispersity of chord length κ_a and average C-C bond length l_{cc} for different carbon precursors heat treated at different temperatures.

	q
MP700	0.09
MP850	0.157
MP1000	0.2
MP1500	0.384

Table 3.3: Orientation parameter q for MP samples carbonized at different temperatures.

carbon microstructure (e.g. the stacks align preferably along an axis parallel to the graphene planes), an uniaxial preferred orientation of the carbon layers parallel to the surface of the sample is possible compared to samples without texture. In such WAXS geometry, the intensities of inter- and intralayer scattering change relatively to each other [11].

As an important finding, the WAXS patterns of MP samples could be only fitted if preferred orientation is taken into account. As described in Chapter 2.1.2, an *orientation parameter* q is used to describe the *orientation distribution* $g(\varphi)$.[2] Table 3.3 shows the orientation parameter q found for the different MP samples. Clearly, the values for q increase with HTT, speaking for an increase in the orientation with respect to the substrate. No preferred orientation (*q=0)* was found for samples derived from NA, FA, SUC and STA. Figure 3.10 shows the orientation distribution g(φ) of the (00l) reflections for the MP samples using equation 2.8 on page 19. Clearly, g(φ) approximates unity for $q \rightarrow 0$).
This finding can be explained with the different carbonization behavior of mesophase pitch compared to the other carbon precursors. The carbonization behavior of MP and SUC is schematically illustrated in Figure 3.11. The "liquid crystalline" mesophase pitch structure shows preferred orientation with respect to the substrate upon carbonization, whereas the graphenes are more randomly distributed in carbon materials derived from other carbon precursors (e.g. sucrose). Also, the preferred orientation can facilitate the growth of the stacks.

[2] φ is the angle between the perpendicular to the sample surface and the perpendiculars to the layer planes. The orientation parameter q varies between zero (absence of preferred orientation) and unity (perfect parallel orientation of the layers).

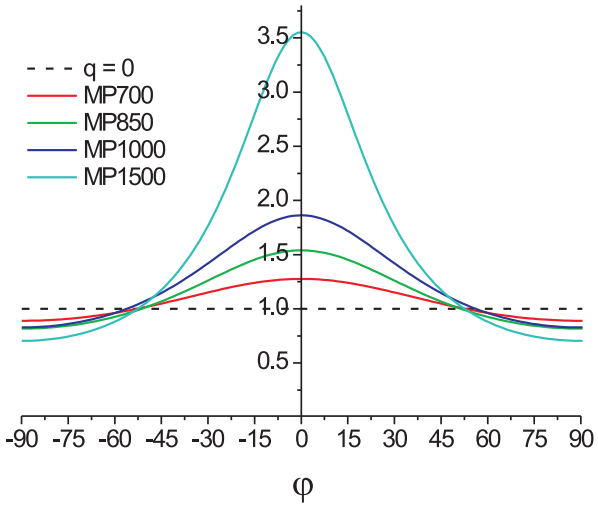

Figure 3.10: Orientation distribution g(φ) between $-90°$ and $+90°$ for different MP samples.

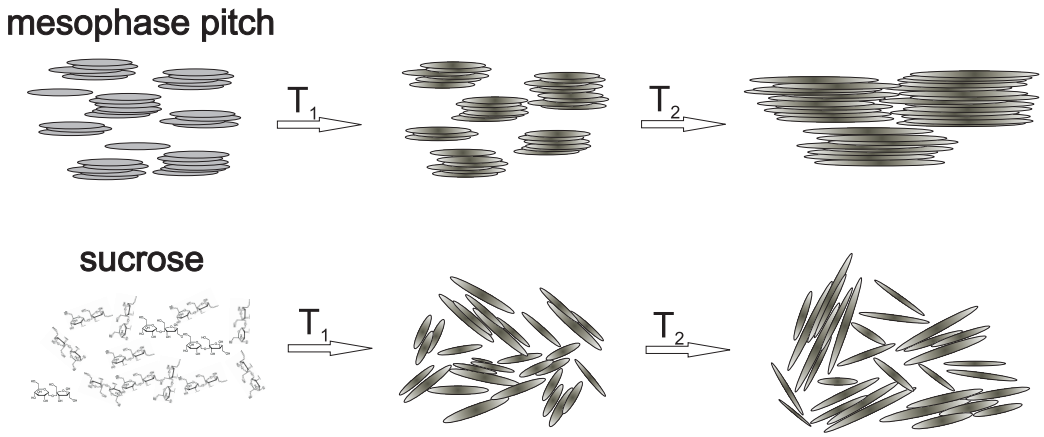

Figure 3.11: Influence of the carbon precursor on the carbon microstructure after carbonization at different temperatures T; ($T_2 > T_1$). Schematic comparison between mesophase pitch and sucrose.

As an important result, the presence of a texture in the MP samples was verified using high-resolution transmission electron microscopy (HRTEM)[3]. Figure 3.12a shows the HRTEM images of MP samples heat treated at different temperatures. In accordance to the WAXS model, the growth of the graphenes in height and length and the development of the texture can be clearly seen by the parallel alignment of the graphene stacks. A HRTEM image of highly oriented pyrolytic graphite (HOPG) is added for comparison. Electron energy loss spectroscopy (EELS) measurements of the carbon-K ionization edge revealed a high sp^2 content in the MP samples. The main features in the ionization edge are the π^* (285 eV) and the σ^* ($>$ 292 eV) peaks, stemming from transitions from 1s into π and σ antibonding states. It can be seen that the intensity ratio $\pi^*/\ \sigma^*$ increases with HTT, indicating that the deviation from a "perfect" sp^2 material decreases. Figure 3.12b shows the sp^2-content (derived from EELS) and the average layer size L_a (derived from the WAXS model) as a function of the HTT. It can be seen that the sp^2-content correlates with increasing values of L_a, proving the progression of the carbonization process. The relative sp^2-content was found to be around 90 % for MP1500.

In summary, HRTEM and EELS measurements clearly confirmed the results from the the WAXS model.

3.4.3 Other parameters

The other parameters used for the WAXS modeling are described in the following. However, their evaluation was partly difficult and some of the parameters were kept constant during fitting in order to maintain physically reasonable results for the parameters that were discussed above. The absolute values of all parameters determined from the WAXS model are summarized in Table 3.2 and in the Appendix (Chapter 7.2).

- *Polydispersities of stack size κ_c and chord length κ_a:* As described in Chapter 2.1.2, the polydispersities of stack size κ_c and chord lengths κ_a

[3]HRTEM and EELS measurements were performed by Dr. Jens-Oliver Müller at the Fritz-Haber-Institute, Berlin.

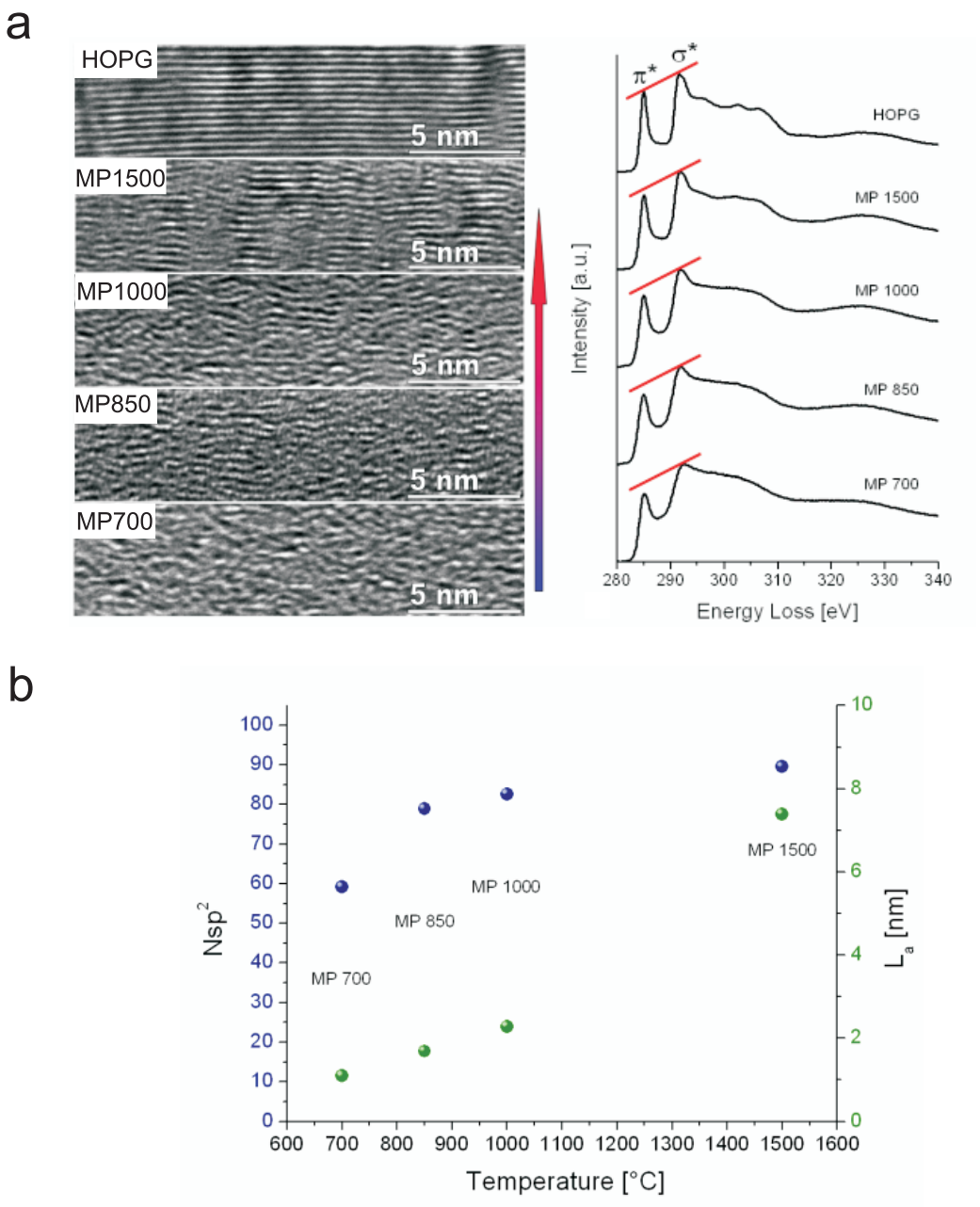

Figure 3.12: *(a)* HRTEM images and corresponding EELS spectra of mesophase pitch carbonized at different temperatures. An image of highly oriented pyrolytic graphite (HOPG) is added for comparison. *(b)* Comparison of the relative sp^2 content derived from the EELS spectra and layer size L_a derived from WAXS modeling.

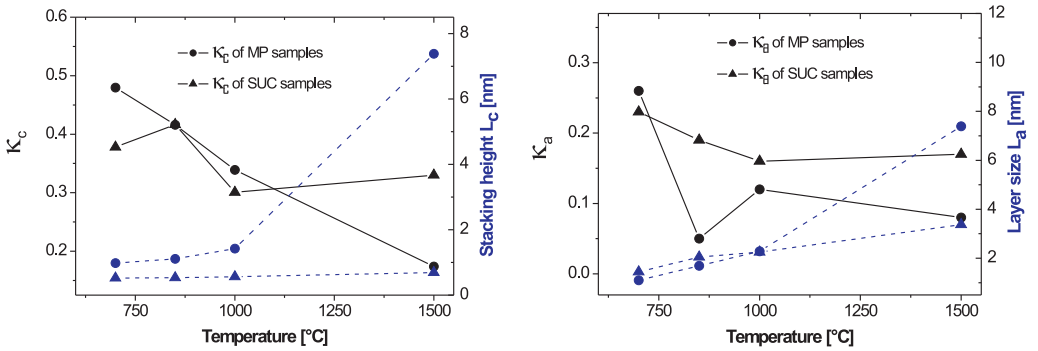

Figure 3.13: Polydispersities of *(a)* stack height κ_c and *(b)* chord length κ_a as a function of the HTT for samples from MP (circles) and SUC (triangles).
a

are defined as $\kappa_c = \frac{\langle N^2 \rangle}{\langle N \rangle^2} - 1$ and $\kappa_a = \frac{\langle l^2 \rangle}{\langle l \rangle^2} - 1$. Figure 3.13a shows κ_c as a function of HTT for SUC and MP samples. MP samples showed a constant decrease in κ_c, speaking for more uniform heights of the stacks with increasing HTT. In contrast, the values κ_c found for samples from the other carbon precursors strongly varied and showed no clear trend within a temperature series (Table 3.2), speaking for huge structural changes during the heat treatment.

Both precursors showed a decrease in κ_a with increasing HTT (Fig. 3.13b), speaking for more uniform sizes of L_a at higher temperatures. Due to the better carbonization behavior, MP samples showed in tendency lower values for κ_a compared to the other carbon precursors.

In summary, the changes of κ_c and κ_a with temperature were slightly more distinct for the MP samples, speaking for a more uniform and less hindered growth of the stacks compared to samples from other carbon precursors.

- *Average C-C bond length l_{cc}:* The C-C bond length in an aromatic system is smaller compared to a single C-C bond ($l_{cc,\ single} = 0.154$ nm). For example, a bond length $l_{cc,\ benzene} = 0.1398$ nm is found for

benzene. However, the extended electron density distribution in the larger aromatic systems of non-graphitic carbons gives rise to slightly larger values for l_{cc} compared to benzene. Thus, larger values for the average layer size L_a should correlate with larger values for l_{cc}.
The highest l_{cc} values were found for the MP samples ($l_{cc,\ MP} = 0.1405$ nm for all samples), confirming the presence of more defined and larger aromatic systems. Values ≤ 0.1405 nm were found for all other samples. The smallest values were found for samples derived from starch, with $l_{cc,\ STA} = 0.1398$ nm.

- The *concentration of non-organized carbon* c_n was found to be small for all samples. The smallest values were found for MP based samples (c_n= 0.01). Larger values were found for FA850 (c_n= 0.10), FA1000 (c_n= 0.11), STA1000 (c_n= 0.09), SUC850 (c_n= 0.08) and NA850 (c_n= 0.08). However, the results did not show a clear trend within the temperature series of the different carbon precursors, but the small values for most of the samples indicate that only few carbon atoms were not part of the layer structure.

- The parameter η describing the *homogeneity of the stacks* strongly influenced the run of the WAXS pattern at angles $2\theta < 20°$. Usually, values close to unity were found for all samples, speaking for a rather homogeneous structure of the stacks. Smaller values around $\eta = 0.9$ were found for SUC700 and some FA samples. Here it should be mentioned that the shape of the WAXS pattern at such small angles was also influenced by the sample preparation. The WAXS model assumes an absolutely plane sample surface, which could not be guaranteed because the samples were measured as a powder. Thus, the evaluation of η is rather ambiguous.

- The following parameters gave minor information about the carbon microstructure, but strongly influenced the whole run of the calculated WAXS pattern. Therefore, the absolute values had to be carefully chosen. The *disorder and strain parameters* σ_1 and ε_1, referring to the

layer structure, were kept at small absolute values between 0 - 0.025. The values were mostly kept constant within the temperature series of each carbon precursor. Also, the *thermal motion parameter* u_3 was kept at very small absolute values ($0.01 < u_3 < 0.029$). The *disorder parameter* σ_3, referring to the layer stacking, was kept at values between $0.0025 < \sigma_3 < 0.09$. The disorder was found to be smaller for samples from the aromatic precursors (MP and NA) compared to the other carbon precursors. The highest values were found for samples from STA and FA. However, a clear trend within the temperature series of the different precursors was not observed.

In summary, it should be emphasized that the WAXS model allows a much more accurate determination of the carbon microstructure compared to Raman spectroscopy. The comparison between both methods is discussed in Chapter 3.6.

3.5 Phenolic resin as carbon precursor

The WAXS model was also used to examine the carbon microstructure from samples derived from phenolic resin (PR). Introduced in the beginning of the 20th century (L. H. Baekeland, 1907), phenolic resins are the oldest thermosetting polymers and are still widely used in industrial applications, e.g. for insulations. Recently, phenolic resins were used for the synthesis of mesoporous carbon materials that can be used for e.g. electrochemical applications (Chapter 5.4). As will be shown, the carbon microstructure is of great importance for electrochemical applications such as lithium storage. Therefore, a good knowledge of the carbon microstructure of PR based materials is desirable.

Figure 3.14a shows the WAXS patterns and corresponding fits of the WAXS model for PR samples heat treated at 600, 800 and 1200 °C. The examined samples were obtained as prepared, thus the exact temperature treatment was unknown.

As can be seen, the (00l) reflections appear only as very broad shoulders,

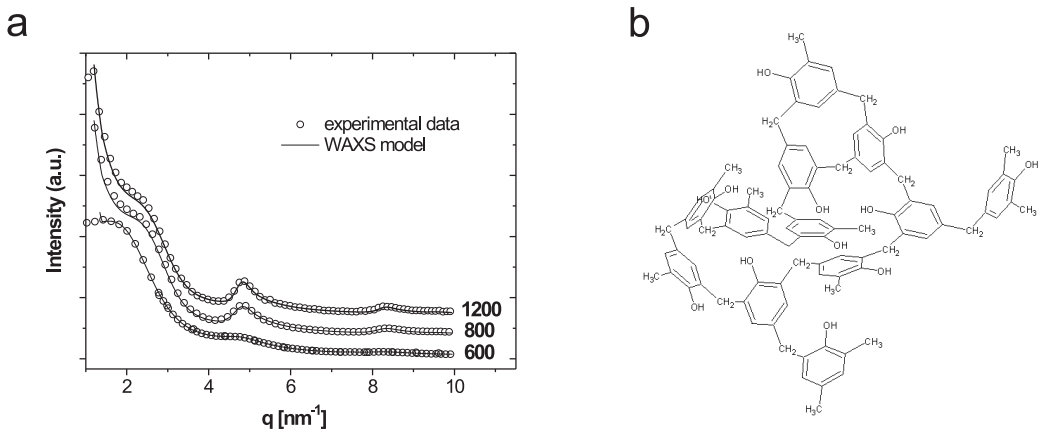

Figure 3.14: *(a)* WAXS patterns from phenolic resin heat treated at 600, 800 and 1200 °C. *(b)* Structure of Bakelite.

speaking for a extremely disordered carbon microstructure. The key parameters of the carbon microstructure are shown in Table 3.4. Large average interlayer spacings $\overline{a}_3$ and quite small values for L_c and L_a were found for all samples. Even at 1200 °C, the layer size L_a was found to be only 1.86 nm.

This behavior is expectable, since phenolic resins consist of covalent connected benzene rings, hindering the formation of extended graphene sheets during the heat treatment. As an example, the structure of *Bakelite,* a resin formed by polymerization of phenol and formaldehyde is shown in Fig. 3.14b.

In summary, it can be stated that the carbonization behavior of phenolic resins is comparably bad, giving rise to a very disordered carbon material, with a huge number of inherent defects (micropores). The use of such a

	L_c [nm]	L_a [nm]	$\overline{a}_3$ [nm]
PR600	0.51	1.2	0.352
PR800	0.63	1.48	0.363
PR1200	0.67	1.86	0.359

Table 3.4: WAXS model results for samples from phenolic resin (PR) heat treated at 600, 800 and 1200 °C: Average stack height L_c, average layer size L_a and average interlayer spacing $\overline{a}_3$.

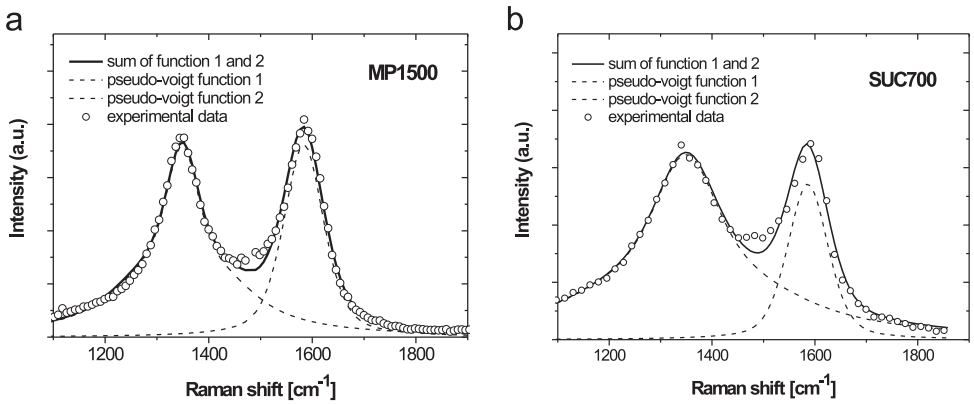

Figure 3.15: Comparison of the Raman spectra and corresponding fit for *(a)* MP1500 and *(b)* SUC700. The spectra were fitted with two pseudo-Voigt functions.

material for electrochemical applications such as lithium storage is limited since these defects can trap lithium ions, giving rise to a huge irreversible capacity. Also, the conductivity of the material is reduced due to the disorder.

Thus, phenolic resins are bad precursors for the synthesis of carbon materials when e.g. low micropore content and good conductivity are desired.

3.6 Comparison with Raman spectroscopy

Raman spectroscopy is commonly used for the analysis of carbon materials, using the correlation found by Tuinstra and Koenig (Chapter 2.2). It should be pointed out that this method only allows an estimation of the average layer size L_a by peak analysis. The influence of other structural parameters influencing the Raman spectra is neglected.

In the following, the results from Raman spectroscopy and WAXS model are compared using samples from MP and SUC. Samples from the other carbon precursors showed similar differences between both methods. The results for all samples are summarized in the Appendix (Tables on page 127 and 128).

The layer size L_a was determined using equation 2.13 on page 21 proposed

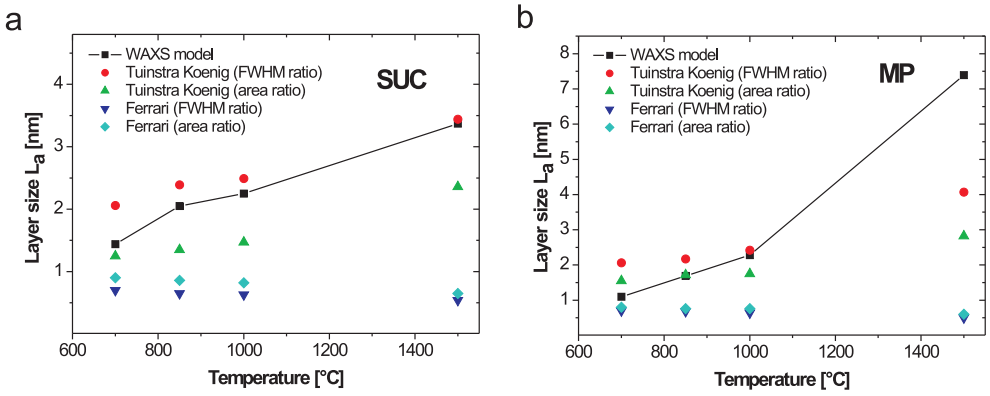

Figure 3.16: Layer sizes L_a deduced from the Raman spectra and WAXS model for samples from *(a)* sucrose (SUC) and *(b)* mesophase pitch (MP). The Raman spectra were evaluated using the correlations from *Tuinstra and Koenig* and *Ferrari*. The intensity ratio I(D)/I(G) was determined using the ratio of the areas and FWHM (full width at half maximum). Raman spectra were fitted with two pseudo-Voigt functions.

by TUINSTRA AND KOENIG. In this equation, the ratio I(D)/I(G) of the two Raman bands is correlated with L_a. In this work, peak area and full width at half maximum (FWHM) were used to determine I(D) and I(G). Also, a modified equation (Equation 2.14 on page 21) by FERRARI ET AL. for layer sizes smaller 2 nm was used for the evaluation.

Figure 3.15 shows the Raman spectra and corresponding fit of MP1500 and SUC700. The Raman spectra were fitted using two pseudo-Voigt functions. A better approximation of the whole spectra, in particular at Raman shifts around 1500 cm^{-1}, can be obtained by introducing additional functions. However, the use of more functions does not implicate more accurate results for the layer sizes L_a, since the fitting itself is not based on a holistic structural model like the WAXS model.

In Figure 3.16, the average layer sizes L_a obtained by analysis of the Raman spectra are compared with the results from the WAXS model. It can be seen, that the choice of the equation and the way to determine I(D)/I(G) strongly influences the resulting values for L_a. For the analyzed samples, the correlation from Tuinstra and Koenig seems more accurate. For SUC700,

better correlation with the results from the WAXS model was found, when I(D)/I(G) was determined by the area ratio. At higher HTT, the use of the FWHM ratio seemed more accurate (Fig. 3.16a). Analogues results were found for carbons derived from the other carbon precursors NA, FA and STA. This finding was less distinct for the samples derived from MP.

The modified equation of Ferrari et al. for layer sizes smaller than 2 nm, gave only a good correlation with the WAXS model for MP700. However, the WAXS model could not verify this equation, even though layer sizes L_a were smaller than 2 nm for all samples carbonized at 700 °C. The use of the equation of Ferrari et al. is therefore not recommended for the present carbon materials when the Raman spectra are evaluated as described.
The advantage of Raman spectroscopy is the fast measurement and easy evaluation by the described equations. However, origin and shape of the Raman bands as well as their evaluation are still under discussion and lack of a clearly defined theoretical background [22, 24, 25, 53]. Also, the penetration depth of the laser is small (around 100 nm [54]), making it difficult to draw conclusions for the bulk material. Another disadvantage is the risk of thermal damage during measurement, due to the strong absorption of light.

Thus, it can be concluded that Raman spectroscopy gives only vague information about the carbon microstructure of non-graphitic carbon materials. Also, only L_a can be determined using this method. However, if Raman spectroscopy is used for the quantitative analysis of non-graphitic carbons, the determination of the intensity ratio using the FWHM seems more accurate compared to when the area ratios are used.

3.7 Thermal stability

Thermogravimetric analysis (TGA) was used to demonstrate the influence of the carbon microstructure on the thermal stability of the carbon material. Figure 3.17 shows the results from TGA for SUC850 and MP850 for comparison. The thermal stability was tested under oxygen flow at a heating rate of 15 K min^{-1}. The onset of decomposition was found to be around 685 °C for MP850 and around 530 °C for SUC850, clearly proving a much better

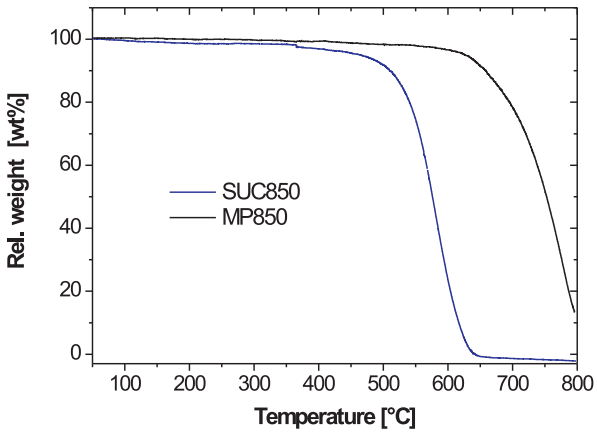

Figure 3.17: Thermal stability of MP850 and SUC850 under oxygen using TGA (oxygen flow 15 ml min^{-1}, heating rate 15 K min^{-1}).

thermal stability of MP850. This finding is expectable, since more energy is needed to break up the larger carbon stacks of the MP based carbon material. Also, the larger stacks reduce the contact area between the carbon atoms and the gas molecules.

3.8 Summary

In this chapter, the carbon microstructure of different non-graphitic carbons was studied in detail. Mesophase pitch proved to be an excellent carbon precursor, if a well-developed carbon microstructure, i.e. comparably large values for stack height, L_c and layer size, L_a are desired at relatively low HTT. In particular, L_c was found to be significantly higher for samples obtained from mesophase pitch, compared to the more disordered carbon materials, derived from the other carbon precursors. Thus, non-graphitic carbon materials from mesophase pitch exhibit only a small inherent micropore content. As can be seen in the following chapters, this property will be of importance for the synthesis of new, porous carbon materials that are in particular useful for the storage of energy.

Also, it was shown that the WAXS model by Ruland and Smarsly is a powerful tool to determine various additional parameters of the carbon microstructure, e.g. polydispersities, distributions or the average C-C bond length. Also, the information obtained exceeds by far the results that are accessible by Raman spectroscopy. It should be pointed out that this traditional method lacks a complete theoretical backup and is applied by *analyzing individual peaks*. Moreover, only absolute values for the average layer size L_a can be determined using this method.

In contrast, the WAXS model enables the *calculation of the whole WAXS pattern* ($10° < 2\theta < 100°$), based on a structural model. That way, the model revealed the presence of a texture in the MP samples that could be verified by HRTEM. Also, the WAXS model could be applied for non-graphitic carbons that exhibited a very disordered carbon microstructure (e.g. carbons from starch or phenolic resin). This also shows that the true carbon microstructure of non-graphitic carbons is well approximated by the assumptions made in the WAXS model.

Chapter 4

Synthesis of Hierarchical Macro- / Mesoporous Carbon Monoliths by Hard-templating using Mesophase Pitch

4.1 Introduction

The major fraction of porous carbon materials that are used in applications are activated carbons for filtration technology. Activated carbons exhibit large surface areas (> 500 m^2 g^{-1}) due to accessible slit-like pores of diameters less than 2 nm. These pores are so-called micropores and are small enough to trap a high number of different substances (in particular contaminants) from a mobile phase. Activated carbons with such a high amount of accessible micropores are obtained by well-established activation procedures, e.g. steam activation of natural carbon sources such as coconut shells.

However, bigger pores are necessary for applications involving larger molecules or nanocrystals, e.g. adsorption of dyes or when the carbon material is used as a catalyst support. On the other hand, the pores should be still small in order to provide a large area of interaction (surface area), thus making pores in the mesorange (2-50 nm) desirable.

As described in Chapter 2.4., carbon materials are also widely used as anode material in lithium ion batteries. An electrode material exhibiting mesopores would increase the interface for ion exchange and therefore would allow better battery performance. At the same time, the micropore content should be as small as possible to prevent irreversible trapping of the lithium ions.

A hierarchical porous carbon material also exhibiting macropores ($>$ 50 nm) would allow easy access to the mesopores and could further improve the material performance. Primarily, a continuous macropore network could work as a transport route for a gas or a liquid (e.g. an electrolyte).

It would be particularly useful, if such a hierarchical macro- / mesoporous carbon material could be synthesized in form of a monolith, since this would supersede the use of a binder or conductive agent. Compared to a powder, a monolith is also useful for chromatography columns since the pressure drop is kept low. Furthermore, only a monolith with a continuous macropore network can ensure the facile transport of a mobile phase over a larger volume.

However, a major challenge in the generation of mesoporous carbon materials still lies in the principal incompatibility of achieving a carbon matrix with a well developed microstructure (i.e. large graphene sizes) and mesoporosity at the same time. The reason is that the carbonization process itself usually leads to pore collapse due to the growth of the graphenes.

In this chapter, we present the synthesis of a new monolithic carbon material by *nanocasting* using a hard template. The material combines for the first time the advantages of a hierarchical macro- / mesoporous structure with a well developed carbon microstructure by choosing mesophase pitch (MP) as the carbon precursor. As described in Chapter 3, mesophase pitch carbonizes very well and ensures a low micropore content of the carbon matrix compared to other carbon precursors.

The performance of the synthesized material as electrode material in lithium ion batteries is discussed in detail and the applicability as support material for supercapacitors is shown.

The following chapter gives a brief introduction into the recent progress

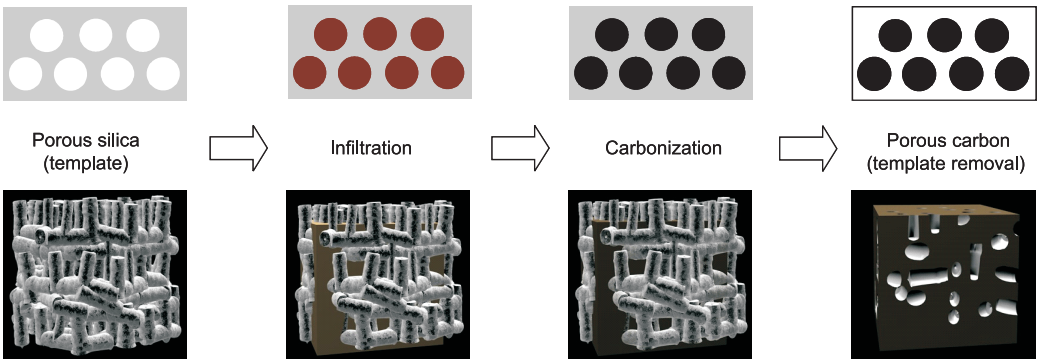

Figure 4.1: Concept of nanocasting by replicating a porous hard template.

in the synthesis of mesoporous carbon materials via the nanocasting route using a hard template.

4.2 Current state of research - Nanocasting of mesoporous carbon materials using hard-templating

A huge variety of mesoporous materials, in particularly silica, could be synthesized during the last years, using the *nanocasting* approach. The most prominent example is probably MCM-41 (Mobil composition of matter No. 41), discovered by Kresge et al. in 1992 [55]. However, it took some more years until Ryoo et al. were the first ones who succeeded in synthesizing ordered mesoporous carbon materials. Hereto, they used nanocasted mesoporous silica as hard template [17].

The major concept of nanocasting using a hard template is shown in Figure 4.1. A porous, inorganic template (usually silica) is infiltrated with a carbon precursor, e.g. sucrose in aqueous solution. Then the hybrid material is carbonized under protective atmosphere, typically between 600 and 1000 °C. After carbonization, the porous carbon replica is obtained by dissolving the silica template. The pore diameter of the replica is mainly determined by the wall thickness of the template. In their work, Ryoo et al. used a cubic mesoporous silica molecular sieve (MCM-48) as template and sucrose

as carbon precursor. The resulting carbon material was denoted as CMK-1 (carbon mesostructured by KAIST, Korea Advanced Institute of Science and Technology) and exhibited periodically aligned mesopores.

The same concept was also applied for other porous silica materials. For instance, SBA-1 (cubic pore structure) and SBA-15 (2D hexagonal) were used to synthesize CMK-2 and CMK-3, the exact inverse replica of the templates. This proved that the silica structures can be faithfully replicated on the nanometer scale. Various porous silica materials could be synthesized via the nanocasting approach and thus also a considerable number of carbon replicas could be synthesized [19]. However, it has to be taken into account that a successful structural replication can be only obtained when the silica template exhibits a 3D pore connectivity. Otherwise, the structure collapses as it is the case for MCM-41 (1D channel-like pores). Not only porous silica materials but also silica nanoparticles were successfully used as hard template. Hereto, the nanoparticles are dispersed in a carbon precursor [56].

Hierarchical macro- / mesoporous silica monoliths can be synthesized using the Nakanishi process and the material is already commercially used in high-pressure liquid chromatography (Chromolith® , Merck KGaA) [57]. The Nakanishi process takes advantage of the polymerization induced phase separation of inorganic sol-gel systems. The principle will be further discussed in Chapter 5.2. Smaller hierarchical porous carbon monoliths could be synthesized by replication of these porous silica systems using repeated infiltration and carbonization [58, 59]. Due to the nature of the template, the carbon replicas exhibited a continuous macroporous network. Another group succeeded by using two hard templates of different size (SBA-15 for mesopores, NaCl crystals for macropores) that were pressed to pellets with the carbon precursor prior carbonization [60]. However the macropores did not form a continuous structure.

Motivation

All of these synthesis have in common that they rely on furfuryl alcohol (FA) or sucrose (SUC) as carbon precursors. However, FA and SUC give rise to

a carbon material with less developed carbon microstructure. As shown in Chapter 3, particularly small values for the stack height L_c were found for samples from FA and SUC, leading to inherent microporosity that is not desired for electrochemical applications [61]. A higher HTT *(high temperature treatment)* would increase the quality of the carbon microstructure, i.e. growth of the graphenes and closure of the micropores. But the use of silica as hard template limits the HTT to around 1200 °C, due to the formation of SiC.[1] Alternatively, the carbon replica could be carbonized a second time on its own, but the growth of the graphene sheets would close the mesopores and the surface area would be strongly reduced.

In general, it is very difficult to synthesize a mesoporous carbon material with both, a high surface area and a well developed sp^2 carbon microstructure, and only limited progress could be achieved in terms of the aforementioned challenges. Pitches are far better carbon precursors, but infiltration of a nanoporous material is difficult since pitches are hard to dissolve and their melt is highly viscous.

Only a few pitch based mesoporous carbon materials are reported and were synthesized via hard-templating by melt impregnation [63], colloidal imprinting [64], or through catalytic conversion of aromatic compounds to pitch in the silica template itself [65]. Alternative syntheses via vapor deposition were also reported [66]. However, all these pitch-based mesoporous carbon materials are powders and lack a hierarchical porosity.

One aim of this work was to develop a nanocasting procedure that allows for the first time the generation of a hierarchical macro- / mesoporous carbon monolith using mesophase pitch as carbon precursor and a porous silica monolith as hard template. Furthermore, the use of the synthesized material as anode material in lithium ion batteries and catalyst support for supercapacitors was studied.

[1] This finding was used for the synthesis of hierarchical porous SiC materials. The results are published in *"Synthesis and characterization of SiC materials with hierarchical porosity obtained by replication techniques"* [62].

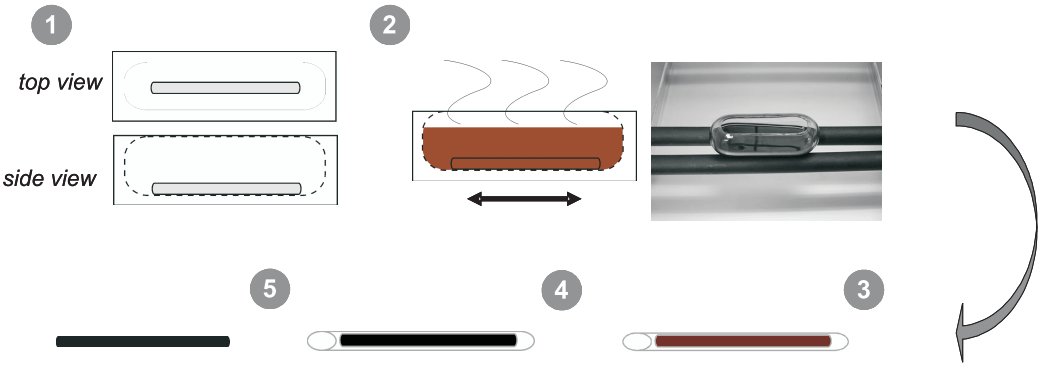

1. *A hierarchical porous silica monolith is placed into an opened glass vessel.*
2. *The diluted MP solution is added. The monolith is infiltrated by mild horizontal agitation while the solvent evaporates and the MP concentration increases.*
3. *The silica-MP hybrid is slowly dried in a quartz tube to prevent cracking.*
4. *The hybrid material is carbonized.*
5. *The hierarchical porous carbon monolith is obtained by dissolution of the template.*

Figure 4.2: Nanocasting of hierarchical porous carbon monoliths using silica as a hard template.

4.3 Synthesis and analysis

For the synthesis, mesophase pitch (MP) was chosen as carbon precursor and hierarchical porous silica monoliths as hard template. The main advantage of the commonly used carbon precursors (furfuryl alcohol and sucrose solution) is that they exhibit a low viscosity. This property makes the infiltration easy, especially due to the capillary action that occurs in pores on the nanometer scale. In contrast, pitches are a solid and show only little solubility. Therefore, it is difficult to infiltrate a whole monolith, and an appropriate infiltration method had to be developed. The used mesophase pitch is quite viscous as a melt ($T_{softening}$ = 275 °C) and thus a successful infiltration could be only accomplished using a solution of MP.

Figure 4.2 shows the principle of the synthesis procedure. First, the hierarchical porous silica monolith is placed into an opened glass vessel. MP is dissolved in THF to obtain a solution (10 wt% MP) of low viscosity. Thereto, the MP has to be stirred in the solvent for at least 3 days. The solution is then poured into the vessel and the porous silica monolith is infiltrated un-

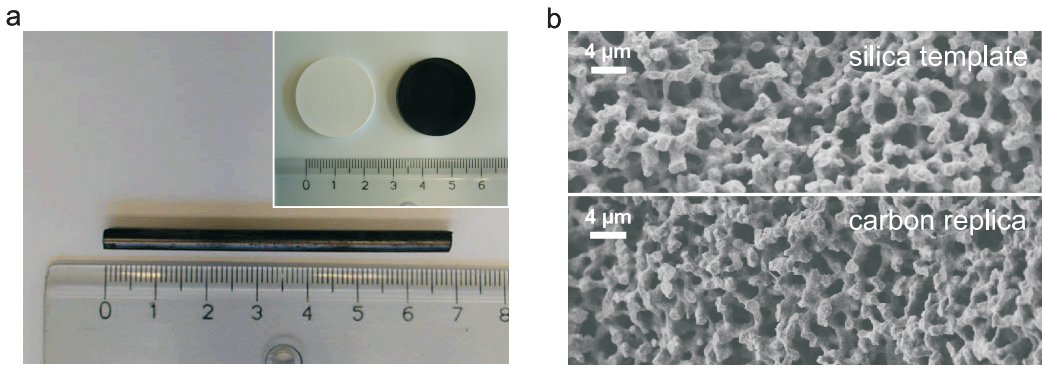

Figure 4.3: *(a)* Photograph and *(b)* SEM image of the silica template and the synthesized carbon replica.

der horizontal agitation. The agitation and slow evaporation of the solvent allows a continuous accumulation of the mesophase pitch molecules in the porous template. After evaporation of the solvent, the infiltrated silica / MP hybrid material is taken out of the vessel and dried in a quartz tube. This ensures a slow drying process that prevents cracking and also helps to retain the macroscopic shape of the monolith. The hybrid material is then carbonized under nitrogen flow between 700 - 1000 °C. The carbon replica is then obtained by dissolving the silica template in a solution of ammonium hydrogen difluoride. All synthesized monoliths were mechanically stable and in most cases crack-free.

Figure 4.3 shows photographs and SEM images of the silica template and the carbon replica. The photographs show that the macroscopic shape of the silica templates could be maintained during the synthesis. Cylindrical monoliths with a diameter of about 4.5 mm and a length of several centimeters could be synthesized that way. Also, carbon replica in the shape of a disk could be synthesized by using an appropriate silica template. Figure 4.3b shows the fully interconnected sponge-like macroporous structure of the silica template and the carbon replica. The SEM images prove that the high quality of the silica structure could be successfully transformed to its carbon replica. Figure 4.4 shows SEM and TEM images of the carbon replica at higher magnifications. It can be seen that the carbon matrix itself is highly porous exhibiting pores in the mesopore range (2 - 50 nm) that are uniformly

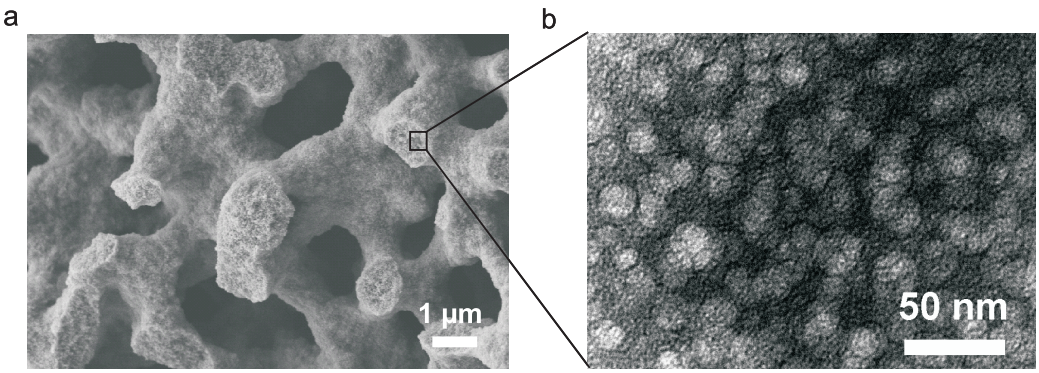

Figure 4.4: *(a)* SEM and *(b)* TEM image of the synthesized carbon monolith.

distributed.

The hierarchical porosity was also determined using Hg-porosimetry. It is important to note that this technique allows the determination of pore diameters over several magnitudes, but the results get less exact for pores in the meso-range. Also, small mesopores cannot be detected with this technique.

Figure 4.5a and b show the cumulative pore volumes and the pore size distributions of the silica template and the carbon replica. The graphs reveal a well defined hierarchical (bimodal) porosity with narrow pore size distributions for template and replica. Mesopores between 6 - 8 nm and macropores in the range of 2 μm were found for the carbon monolith, whereas the mesopore volume contributed around 20 % to the total pore volume $V_{tot,\ Hg\text{-}Por.}$.[2] Slightly larger pore diameters were found for the silica template. Here the mesopores contributed around 17 % to $V_{tot,\ Hg\text{-}Por.}$. The results from Hg-porosimetry are summarized in Table 4.1.

The results also gave a better insight into the replication process. For a successful synthesis, it is crucial that the carbonization of the carbon precursor mainly occurs in the mesoporous silica skeleton and not in the macroporous network. Otherwise the carbon replica does not exhibit the desired macroporous transport system. Fig. 4.5c shows the results from Hg-

[2]Within this work, Hg-porosimetry and nitrogen sorption experiments were used for the determination of pore volumes. In the following, the referring pore fraction and used method are indicated with indices. E.g. $V_{tot,\ Hg\text{-}Por.}$ for total pore volume determined by Hg-porosimetry or $V_{meso,\ N2\text{-}Sor.}$ for mesopore volume determined by N_2 sorption.

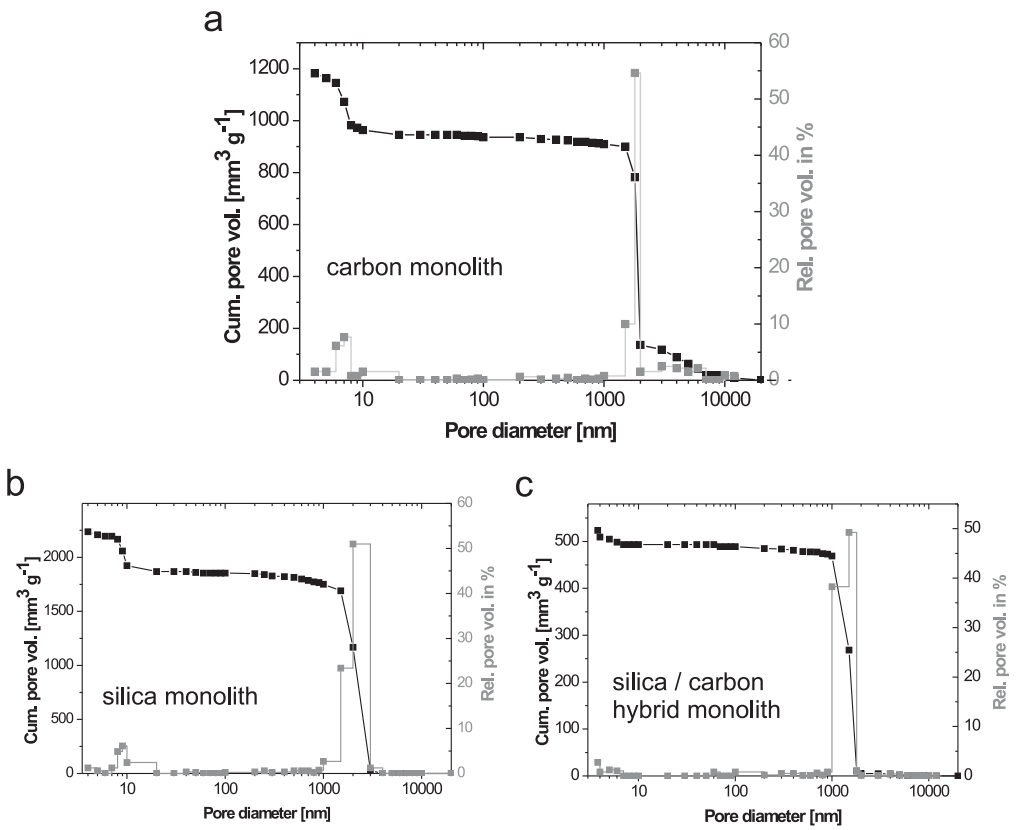

Figure 4.5: Mercury porosimetry results of *(a)* the carbon replica *(b)* the silica template and *(c)* the dried hybrid after infiltration.

	$V_{tot,\ Hg\text{-}Por.}$ [cm^3g^{-1}]	$V_{meso,\ Hg\text{-}Por.}$ [cm^3g^{-1}]	mesopore fraction [%]	$d_{macropore}$ [μm]	$d_{mesopore}$ [nm]
Carbon replica	1.18	0.24	20.0	1.5 - 2	6 - 8
Silica template	2.24	0.38	16.8	1.5 - 3	8 - 20
Silica template after infiltration	0.52	0.03	5.8	1 - 2	< 7

Table 4.1: Results from Hg-porosimetry. $V_{tot,\ Hg\text{-}Por.}$ and $V_{meso,\ Hg\text{-}Por.}$ are the total pore volume and the mesopore volume derived from Hg-Porosimetry. d is the average diameter of the pores.

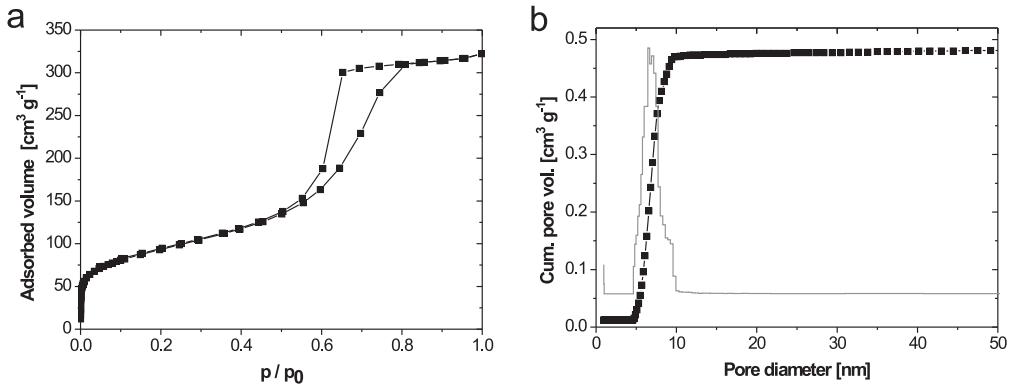

Figure 4.6: Results from nitrogen sorption experiments. *(a)* Typical isotherm of the synthesized carbon monoliths, *(b)* Cumulative pore volume and corresponding pore size distribution using NLDFT model (adsorption branch). The sample was carbonized at 700 °C.

porosimetry for the silica template after the infiltration step. Clearly, the cumulative pore volume was significantly lower compared to the silica template itself. Only a small fraction of mesopores was detected, speaking for an almost complete filling with mesophase pitch. Also, the average macropore size of the infiltrated template was found to be slightly smaller compared to the silica template, revealing that a part of the macroporous network was filled with mesophase pitch.

As a result, the average macropore size and the total pore volume (assuming similar densities) of the carbon replica were smaller compared to the silica template. The overall infiltration process can be described as a combination of volume templating of the silica skeleton and surface templating of the macroporous network.

Sorption experiments were used to further investigate the porosity in the meso- and micropore range. Figure 4.6a shows an isotherm of type IV that is typical of a mesoporous material. The isotherm reaches nearly a plateau at higher relative pressures, also speaking for narrow pore size distributions. The presence of smaller macropores would otherwise result into an increase at this high rel. pressures. BET surface areas of around 330 m^2 g^{-1} were

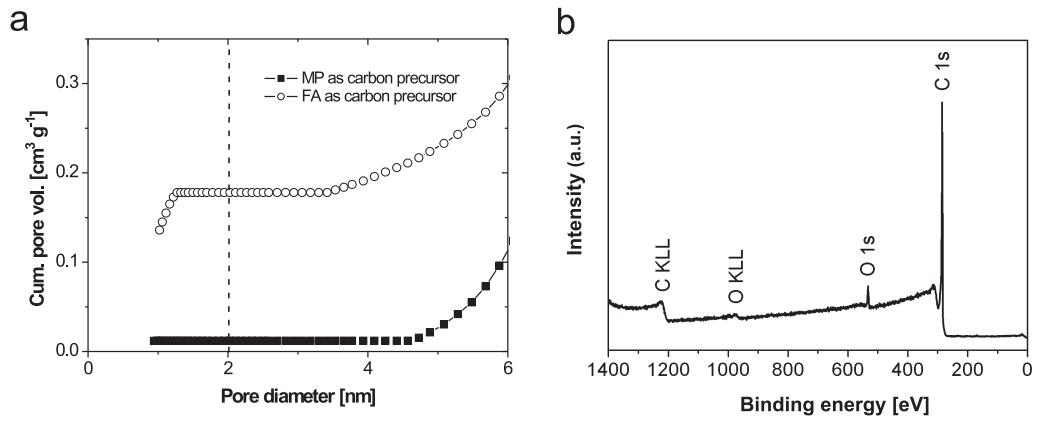

Figure 4.7: *(a)* Micropore analysis (NLDFT model) of the synthesized carbon monolith (using MP as carbon precursor). The result for a carbon monolith using FA as carbon precursor is added for comparison. The dotted line indicates the border between the micro- and mesopore regime. *(b)* XPS analysis of the carbon monolith (carbonized at 700 °C).

typically found for samples carbonized at 700 °C. NLDFT analysis was used to determine the pore size distribution and the micropore content. The cumulative pore volume showed a steep increase for diameters between 5 - 10 nm that corresponded well to the Hg-porosimetry results. The pore size distribution was very narrow with an average diameter of 7.3 nm. The total pore volume was measured to be $V_{tot,\ N2\text{-}Sor.} = 0.55\ cm^3\ g^{-1}$ (Tab. 4.3).

For an exact micropore analysis, several additional points at very low relative pressures (35 points at $p\ /\ p_0 < 0.1$) were recorded during the adsorption process. Figure 4.7a shows the cumulative pore volume drawn to a larger scale for small diameters. For comparison, a silica monolith was also replicated using FA as a carbon precursor. The difference between both precursors can be clearly seen. The MP based carbon replica exhibited a significantly smaller micropore content compared to the FA based replica. For the MP based sample, the micropores contributed only 2.55 vol% to the total pore volume of all pores smaller than 50 nm. In contrast, 19 vol% were found for the FA based sample. The contribution of the micropores to the surface area was 21 % (MP based) compared to 57.7 % (FA based). Thus,

the results clearly evidenced that the choice of the carbon precursor strongly effects the final porosity of the carbon replica and MP proved to be highly advantageous if micropores are undesired. Furthermore, closed porosity should be kept in mind and it can be assumed that, especially for the FA based replica, a substantial amount of additional micropores could not be detected by the sorption experiments.

The sheet resistivity of the MP based monolith was measured to be 0.011 Ωcm compared to 0.771 Ωcm for the FA based monolith, also proving the better carbonization behavior of MP.

X-ray photoelectron spectroscopy (XPS) measurements stated the pureness of the synthesized material (Fig. 4.7b). No traces of Si could be found, revealing that the template could be completely removed by dissolution. A carbon content of 95.5 at.% and oxygen content of 4.5 at.% were determined from the XPS pattern. The low content of contaminants made the carbon monolith an ideal model system to study the material properties. Also, elemental analysis (EA) and energy dispersive x-ray spectroscopy (EDX) proved the high pureness. Elemental analysis was also used to determine the H/C ratio at different HTT (Tab. (4.3)).

As a prove of the mechanical stability, the carbon monoliths were successfully encased by a poymer jacket that is used for HPLC columns (Fig. 4.8).[3]

4.3.1 WAXS analysis

The local structure of the carbon matrix was characterized by wide-angle x-ray scattering (WAXS) measurements. Figure 4.9a shows the WAXS pattern and the corresponding fit of the WAXS model (Chapter 2.1.2) for a carbon monolith carbonized at 1000 °C. As expected, the peaks are well defined due to the use of MP as carbon precursor (Chapter 3). However, the carbon microstructure of the monolith differed from the one that was found for MP carbonized as a bulk (in the following denoted as bulk material). This

[3]The potential application of the synthesized material as separation medium for HPLC was not further pursued within this work.

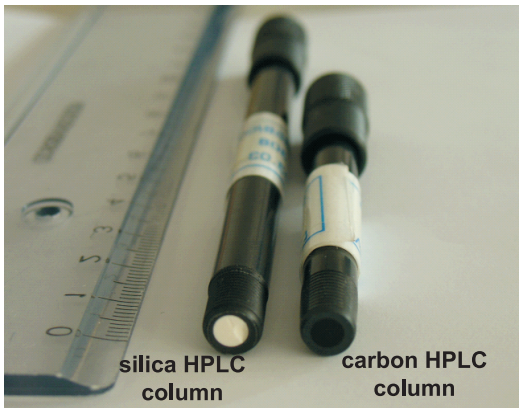

Figure 4.8: Commercial silica HPLC column (Merck) and a potential column from the synthesized carbon material.

	Layer size L_a [nm]	Stack height L_c [nm]	Interlayer spacing $\overline{a}_3$ [nm]	q
Bulk material	2.28	1.42	0.345	0.2
Carbon monolith	2.48	0.81	0.349	0.0

Table 4.2: Dimensions and parameters of the graphene stacks for carbonization with and without confinement. Bulk material: Carbonization of MP without template. Carbon Monolith: Carbonization of MP in the silica template. Both samples were carbonized at 1000 °C. q is the orientation parameter as introduced in Chapter 3.4.2. L_a, L_c and $\overline{a}_3$ are average values.

observation was reasonable, since the carbonization process in a bulk material is significantly different compared to the carbonization process in the confinement of the silica template. One can imagine that such a nanometer confinement can hinder the growth of the graphenes. This effect was clearly observed by the WAXS model.

Table 4.2 shows the key parameters derived from the WAXS model for the carbonization of mesophase pitch in a confinement (carbon monolith) and without confinement (bulk material). The average dimensions of the graphene stacks within the carbon monolith were determined to be 2.48 nm for the layer size L_a and 0.81 nm for the stack height L_c. Comparing these values with the corresponding bulk material (L_a = 2.28 nm, L_c= 1.42 nm), it

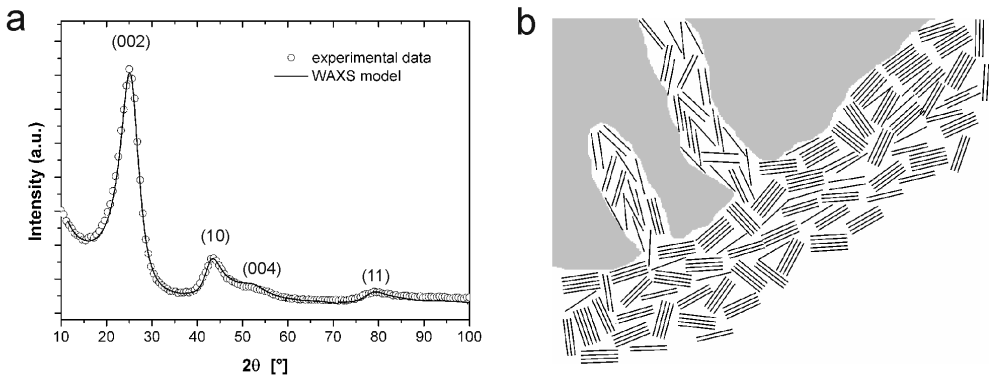

Figure 4.9: *(a)* WAXS measurement and corresponding WAXS modeling of a carbon monolith (carbonized at 1000 °C). *(b)* Proposed model for the infiltration process.

can be seen that especially the growth perpendicular to the graphene planes is strongly hindered by the confinement. Instead, the graphene stacks seem to grow more along the planes, because the average layer size was found to be slightly larger compared to the bulk material.

The possible situation after the infiltration process is shown in Figure 4.9b. The main proportion of the mesopores in the silica monoliths were in the range of 6-16 nm (nitrogen sorption, NLDFT model applied on the adsorption branch). One can imagine that only single MP molecules could enter these small pores, whereas molecules forming a mesophase deposited only on the macropore wall of the silica template. For an increase in stack height L_c, the molecules have to "slide" over each other, but the mobility inside the mesopores was very limited and thus, growth occurred predominantly along the graphene layers. The relative disorder within the silica mesopores also explained why the orientation parameter q (as introduced in Chapter 2.1.2) was found to be zero for the carbon monolith. This finding speaks for the absence of a texture within the carbon microstructure (here, preferred alignment of the stacks among each other and with respect to the sample holder surface). This finding also correlates well with the average interlayer spacing $\overline{a}_3$ that was found to be slightly larger compared to the bulk material.

Despite the confinement effect, WAXS measurements proved that the

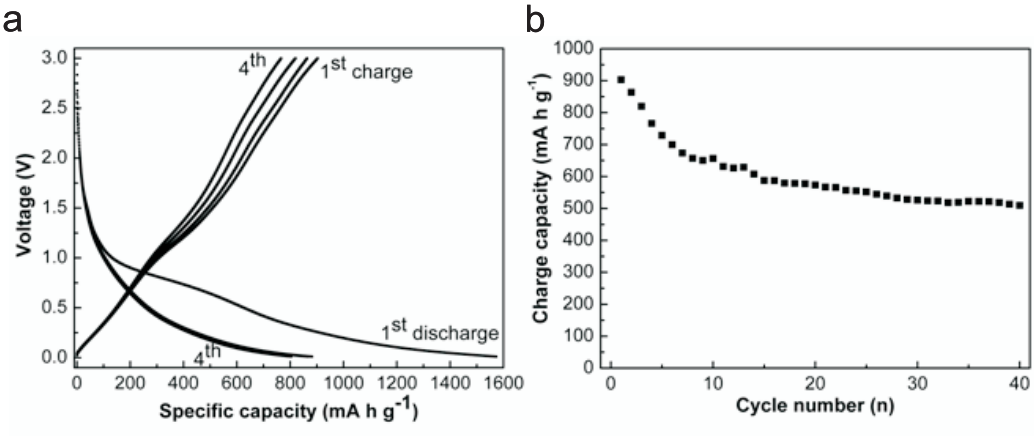

Figure 4.10: *(a)* Galvanostatic discharge (Li insertion, voltage decreases)/charge (Li extraction, voltage increases) curves and *(b)* cycling performance of a sample carbonized at 700 °C. The sample was cycled at a rate of C/5.

carbon monoliths still exhibited a well developed carbon microstructure confirming the micropore analysis results from sorption experiments.

4.4 Li insertion / extraction measurements[4]

The use of mesophase pitch was proven to be an excellent carbon precursor that gave rise to the low micropore of the synthesized material, making the carbon monoliths interesting for certain electrochemical applications. As a possible application, the carbon monoliths were tested as anode material for lithium ion batteries. Figure 4.10a shows the first four discharge (Li insertion) / charge (Li extraction) curves for a sample carbonized at 700 °C (C-Rate = C/5). A huge irreversible loss of about 700 mA h g^{-1} was measured mostly due to the formation of the solid electrolyte interphase (SEI) during the first cycle. As described in Chapter 2.4, such a loss is typical of all carbon materials with high surface area. The first reversible capacity was as high as 900 mA h g^{-1} (Fig. 4.10a).

As an important finding, the reversible capacity stabilized after around

[4]The Li insertion / extraction measurements were performed by Dr. Yong-Sheng Hu at the Max-Planck-Institute for Solid State Research, Stuttgart.

Samples	BET surface area [m^2 g^{-1}]	$V_{tot,\ N2\text{-}sorption}$ [cm^3 g^{-1}]	H / C atomic ratio
700 °C	330	0.55	0.257
850 °C	327	0.59	0.094
1000 °C	277	0.47	0.018
1500 °C*	150	0.20	—
2500 °C*	61	0.13	—

Table 4.3: Results from nitrogen sorption experiments and elemental analysis for carbon monoliths heat treated at different temperatures. The total pore volume $V_{tot,\ N2\text{-}sorption}$ was determined by the last point of the adsorption branch. * The samples were first carbonized at 1000 °C. The carbonization at higher temperatures followed in a second step after removal of the silica template.

15 cycles at values around 500 mA h g^{-1} which is significantly higher than the theoretical capacity of graphite (372 mA h g^{-1}) (Fig. 4.10b).

Several samples were prepared to study the influence of the HTT on the Li insertion and extraction. Table 4.2 shows the porosity and H / C ratio for the different samples. Due to the formation of SiC at temperatures higher than 1200 °C, the monoliths could be only carbonized at 1500 °C and 2500 °C without the silica template. Thereto, the samples were first carbonized at 1000 °C and the silica template was removed afterwards as usual. Then the samples were carbonized again at 1500 °C and 2500 °C. The few micropores close due to graphene growth and thus, the surface area decreases with higher HTT. Since the template was already removed, the decrease in surface area and total pore volume was very pronounced for the samples carbonized at temperatures higher than 1000 °C.

Figure 4.11a shows the first discharge/charge curves of the samples carbonized at different temperatures. The small plateau between 0.8 and 0.7 V can be attributed to the SEI formation and decreases with HTT. Both irreversible charge and reversible charge capacity decrease with increasing HTT.

As described in Chapter 2.4, the mechanisms of lithium storage in non-graphitic carbons are still under discussion, and different models were devel-

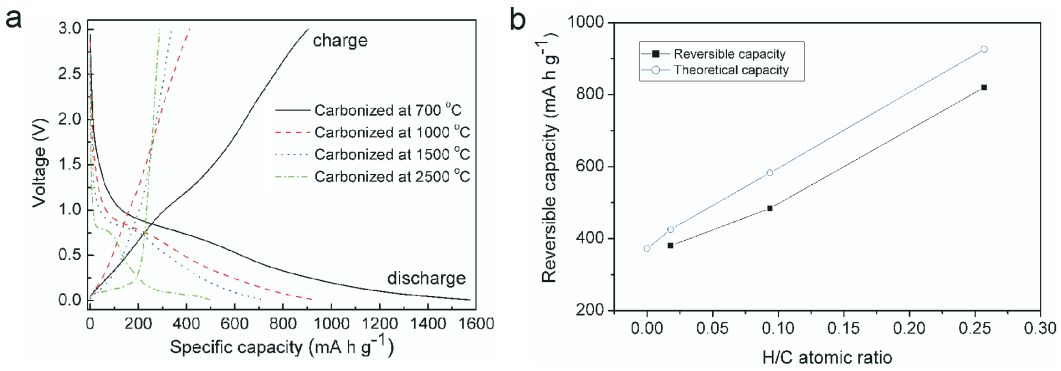

Figure 4.11: *(a)* Influence of the HTT on the (galvanostatic) discharge/charge process (C-Rate = C/5). *(b)* Reversible capacities (3. discharge / charge cycle) as a function of the H/C atomic ratio.

oped in order to explain the higher charge capacity compared to graphite. In the following, the different models are compared with respect to the reversible charge capacity observed for the samples carbonized at different temperatures.

One model suggests that the hydrogen content plays a major role in the lithium storage of non-graphitic carbons. The observed decrease in reversible capacity can be correlated with the H / C atomic ratio and follows the theoretical capacity that assumes each hydrogen atom binding to one lithium atom via $Li \bullet\bullet\bullet H \bullet\bullet\bullet C$ interactions (Fig. 4.11b) [42]. However, the nature of these interactions could not be well explained yet.

Another model attributes the additional capacity to the huge number of additional graphene edges and surfaces that occur in non-graphitic carbons. Higher HTT give rise to larger graphene stacks, and thus the decrease in reversible capacity would be a consequence of the decrease in graphene stack surface and number of graphene edges. Furthermore, the growth of the graphene stacks would be accompanied by further dehydrogenation and thus the proposed correlation with the hydrogen content would be only indirect. Therefore, the growth of the graphene stacks is the more probable explanation for the decrease in reversible capacity with HTT.

Also, nanoscopic cavities are suggested to store additional lithium. However, the total mesopore volume remained more or less constant for the

samples carbonized between 700 °C and 1000 °C (Tab. 4.3). Therefore, additional lithium storage in the mesopores seems rather improbable.

Furthermore, the micropore content also decreases with higher HTT, additionally contributing to the decrease in irreversible capacity. However, a complete separation of all the proposed models and the effects remains difficult.

In summary, the results clearly show that a significant stationary capacity (500 mA h g^{-1} (700 °C)) can be achieved by using mesophase pitch as carbon precursor. While few reports have been recently published reporting similarly high values, it has to be taken into account that the measurements were conducted at a relatively small rate of C/5, i.e. commonly used for such experiments [67].

Here it is important to note that the advantage of the hierarchical pore system takes effect at higher C-rates, giving rise to a unique rate performance at much higher currents:

Figure 4.12 shows the rate performance of the carbon samples carbonized at different temperatures. Rates of up to 60C were employed at which a high capacity was maintained. In the experiment, the battery was first cycled at 1C for four cycles. Then the discharge / charge rates were stepwise increased up to 60C. The effect of the HTT can be clearly seen. The sample carbonized at 700 °C showed the best performance, with reversible capacities of around 540 mA h g^{-1} at 1C (after 4 cycles), 260 mA h g^{-1} at 10C and 145 mA h g^{-1} at 30C. Even at a rate of 60C, a capacity as high as 70 mA h g^{-1} was found. In practical terms, a rate of 60C means to charge/discharge a battery in only one minute (1C corresponds to a charging time of 1 hour). Surprisingly, the cycling performance improves with increasing current density and more constant capacities are measured at high C-rates. For comparison, only 25 mA h g^{-1} were measured for graphite when rated at 10C.

At the end of the experiment, the battery was cycled again at 10C whereas the measured charge capacity corresponded well to the initial value of around

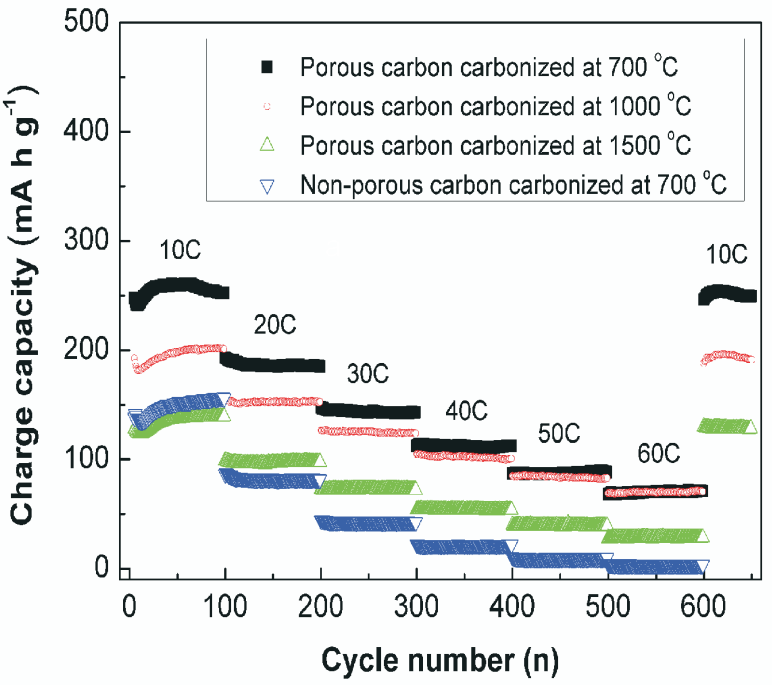

Figure 4.12: Rate performance of carbon samples carbonized at different temperatures. The given C-rate was applied for the charging and discharging process. The non-porous carbon is mesophase pitch carbonized as a bulk without template.

260 mA h g^{-1}. This proves that the cycling was reversible and the material was stable enough to withstand extreme C-rates. In total, the samples were cycled for more than 600 times within this experiment, underlining the excellent cyclability. In comparison, the life time of current commercial lithium ion batteries is around 500 cycles.

As described in Chapter 2.4, the Li-insertion process generally takes longer time than the Li-extraction process. Thus, low C-rates such as C/5 are usually applied for the Li insertion process. Higher C-rates (presuming reasonable high charge capacities), can be only applied for the Li extraction process. By using such different C-rates for insertion and extraction, only one group recently reported a higher capacity at 14C (Li extraction) compared to the presented material [68].

However, *the high C-rates in the presented experiments were applied for both, the Li-insertion and the extraction process.*

It can be assumed that it is the hierarchical porous structure that gives rise to this superior rate performance. The continuous macropore network and the present mesopores allow fast diffusion of the lithium ions into and out of the carbon matrix. The high surface are of the material leads to a high electrode / electrolyte interphase that provides a large number of active sites for charge-transfer reactions. At the same time, the strains that occur in the carbon matrix during the Li insertion and extraction can be well accommodated by the pores, thus improving the battery life time.

It is rather unusual for non-graphitic carbons to be practically free of micropores, and hence for the present context, it is important to note that the systems described here demonstrate otherwise. An increased micropore volume would have lead to an enhanced irreversible Li storage and thus a bad cycling performance would have been measured.

The influence of the hierarchical pore structure can be clearly seen by comparing the rate performance between a porous and a non-porous sample. Here, the non-porous carbon sample is mesophase pitch carbonized as a bulk without template. Even though the performance of the non-porous sample is still better than graphite, the rate performance at very high C-rates is by

far not as good as for the porous samples.

4.5 Macro- / mesoporous carbon monoliths as support material for supercapacitors[5]

The synthesized carbon monoliths could be also successfully used as support material for supercapacitors. This chapter gives a brief introduction into the topic and a short summary of the results.

Supercapacitors are electrical storage devices that can deliver a huge amount of energy in a very short time. Due to their nature, supercapacitors have potential applications in hybrid transportation systems whenever high power densities are needed, e.g. release of extra energy during acceleration or storage of energy during deceleration. Thus, the high power density of supercapacitors could complement to the higher energy densities of batteries in applications that require a flexible energy supply.

Based on the charge-storage mechanism, supercapacitors can be divided into two categories: One is the electrical double layer capacitor (EDLC), where the capacitance arises from the charge separation at an electrode / electrolyte interface, e.g. carbon; the other is the redox capacitor, where the capacitance origins from Faradaic reactions at the electrode / electrolyte interface of e.g. metal oxides or conducting polymers. Compared to EDLC, redox capacitors exhibit higher specific capacitances [69].

The highest value for specific capacitance of metal oxide based redox capacitors was found for hydrous RuO_2 with about 982 F g^{-1} [70]. However, the high costs limit an industrial upscale. Conducting polymers, such as polyaniline (PANI) have advantageous properties with respect to low cost, high conductivity as well as facile synthesis through chemical and electrochemical methods. However, they exhibit low cycle life because of swelling and shrinkage effects that occur during cycling [71].

The use of a suitable support material in the nanometer scale (e.g. car-

[5]The measurements were performed by Dr. Li-Zhen Fan at the Max-Planck-Institute for Solid State Research, Stuttgart.

bon nanotubes) can reduce this effect. Also, nanometer-sized electroactive materials with high porosities in contact with liquid electrolytes can exhibit enhanced electrode / electrolyte interface areas, providing high electroactive regions and decreased diffusion lengths within the active material.

Thus, the combination of PANI and a (conductive) porous carbon support seems promising for supercapacitors of high specific capacitance and improved cycle life. The highest capacitance reported for PANI in a PANI / carbon composite (i.e. capacitance per mass of PANI) is 1221 F g^{-1}, where whisker-like PANI was grown on mesoporous carbon by a chemical polymerization method [72].

In the present project, PANI was electrodeposited onto the synthesized carbon monolith. Following features of the carbon monoliths were supposed to be advantageous for their use as support material: *(1)* Monoliths can be used as synthesized making the use of a binder and / or a conductive agent redundant that otherwise would lead to a decrease in power density. *(2)* The defined mesopore size of about 7 nm (NLDFT model) can limit the grain growth of the active PANI material, thus leading to a higher specific capacitance. *(3)* The interconnected macropore network can render the electrolyte diffusion towards the mesopores, providing fast transport channels for the conductive ions.

Figure 4.13 shows a comparison between the specific capacitance C_{PANI} measured for PANI deposited on the porous carbon monolith and PANI deposited on a non-porous carbon monolith *(Note:* The specific capacitance C_{PANI} refers to the mass m of PANI deposited on the carbon monolith). As can be seen in Figure 4.13a, C_{PANI} was found to be around 2200 F g^{-1} at a current density of 0.67 A g^{-1}, much higher than previously reported [72]. Even at very high current densities of 66.7 A g^{-1}, the specific capacitance was still very high (1270 F g^{-1}). Comparably small values were found for PANI on non-porous carbon, proving that the synthesized carbon monoliths are an excellent support material.

Also, the cyclability was found to be excellent (Fig. 4.13b). Constant values for C_{PANI} were found even after 1200 cycles, while PANI on non-

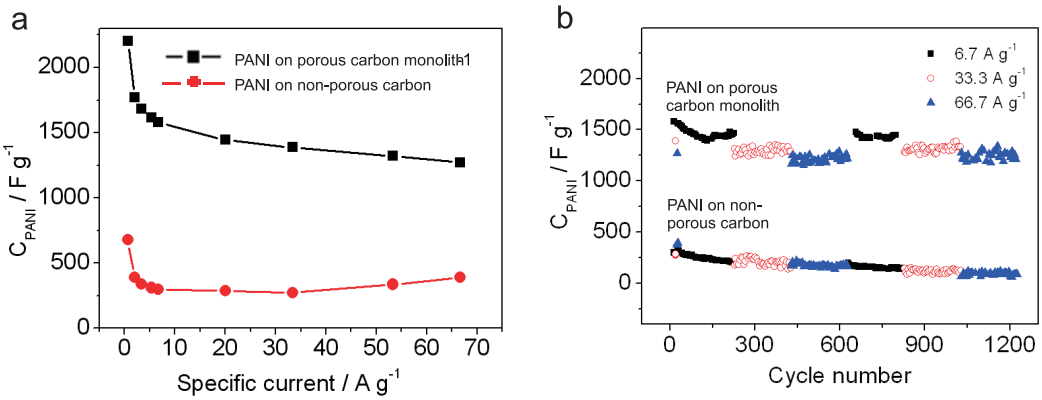

Figure 4.13: Comparison of the supercapacitor performance between PANI deposited on a porous and a non-porous carbon monolith. *(a)* Change of C_{PANI} with specific charge/discharge current for PANI. *(b)* Cycling performance at different specific currents.

porous carbon showed a constant decay in specific capacitance.

In addition, a carbon monolith based on naphthol (NA) was used as support material. As shown in Chapter 3.2, the use of naphthol as carbon precursor gives rise to a more disordered carbon microstructure. The supercapacitor performance of this material was found to be bad compared to the MP based carbon monolith, underlining the importance of the carbon microstructure and the choice of a suitable precursor.[6]

In summary, it can be concluded that the exceptional performance of the electrodeposited PANI origins from the hierarchical porosity and the microstructure of the synthesized carbon monoliths.

4.6 Summary

In this chapter, the synthesis of a new porous carbon material was presented using a hard-templating approach. As the new feature, mesophase pitch was used as carbon precursor for the synthesis of hierarchical porous carbon monoliths with a continuous macroporous network and mesopores of defined size. The use of mesophase pitch gave rise to a carbon material with a

[6]The results are discussed in detail in the corresponding article [73].

well developed carbon microstructure and thus negligible microporosity. The synthesized monoliths were mechanically stable and could be produced in the form of cylinders of several centimeters in length without the need of a binder.

The advantages of the synthesized material could be demonstrated by Li insertion / extraction measurements. The high reversible charge capacity was attributed to the carbon microstructure, whereas the hierarchical porosity gave rise to the unique rate performance.

A possible battery using the synthesized material as electrode would exhibit

- a reversible charge capacity much higher than the currently used graphite materials, and
- a high rate performance that would allow not only very short discharging but also very short charging times.[7]

Also, the material proved to be an excellent support material for the electrodeposition of supercapacitive materials.

[7] In the presented experiments, metallic lithium was used as cathode material. Thus, Li insertion into the carbon material was denoted as the discharging process and extraction as the charging process. In an actual battery, other materials are used as cathode material. Thus, Li insertion into the carbon material means charging the battery, extraction means discharging the battery.

Chapter 5

Synthesis of Hierarchical Macro- / Mesoporous Carbon Materials using Soft-templating and Mesophase Pitch

5.1 Introduction

Soft-templating is, besides hard-templating, the second important method used for nanocasting of porous materials. In this technique, decomposable molecules or polymers are used as template. Such templates can be in most cases completely burned off, making the template removal an easy and cheap step.

However, it was primarily the hard-templating approach that has been intensely used during the last years for the synthesis of (hierarchical) porous carbon materials. Despite the success, the hard-templating approach exhibits some inherent drawbacks: First, an appropriate hard template has to be synthesized before (usually also by nanocasting); and second, acids or bases are necessary for the often time-consuming template removal. Silica, for example, is the most widely used hard template and is usually removed by hydrofluoric acid. The extra step of synthesizing the hard template, and its

dangerous removal makes the overall synthesis a costly multi-step procedure. This is why those systems, despite the promising properties, are likely to stay scientific model systems.

In contrast, nanocasting via the soft-templating route allows the synthesis of porous materials at lower costs. For example, the hierarchical porous silica monoliths that were used as hard templates in this work (see Chapter 4.1) are produced via soft-templating and are commercially available, proving that such materials can be produced at costs that allow an industrial upscale. But the soft-templating of (meso-) porous carbon materials faces two problems:

1. Both, the template and the carbon precursor are of organic nature. The "classical" template removal under air (burning off the template) is therefore not applicable. Instead, the carbonization of the carbon precursor requires a reductive atmosphere. Under this condition, *the organic template can act as a carbon precursor as well,* which is undesired because the formation of pores is then impeded. It is therefore crucial to find an organic template that thermally degrades to a high extent under a reductive atmosphere and in the presence of the carbon precursor. Furthermore, the carbonization of the carbon precursor is often spurred by addition of a catalyst, which can negatively influence the level of degradation of the template.

2. The carbonization process is always accompanied by huge microstructural changes due to the development, growth and rearrangement of the graphene sheets (see Chapter 3). If the template degrades too early, these structural changes can close desired mesopores. *It is therefore crucial that the template does not degrade before the carbon matrix reaches a stable configuration.*

In this chapter, we present a novel soft-templating based methodology to create a carbon material with meso- and macroporosity in a simple process. Hereunto, we were inspired by the synthesis of the hierarchical porous silica monoliths that were used for the nanocasting of the porous carbon monoliths in Chapter 4. These silica monoliths are synthesized via the Nakanishi

process using *spinodal decomposition* between a soft template and a silica precursor. The resulting silica material exhibits a well-defined bicontinuous macropore network and mesopores. The principles of spinodal decomposition and the Nakanishi process are discussed in the following chapters.

The synthesized carbon material was also tested for its electrochemical performance in lithium batteries. The versatility of the synthetic process was demonstrated by manufacture of monoliths and by incorporation of Si nanoparticles into the carbon material. Furthermore, hollow carbon nanofibers were observed.

5.2 Nakanishi process for the synthesis of hierarchical porous silica monoliths

The main concept of the Nakanishi process can be briefly described as follows:

The synthesis is based on a sol-gel process that starts with a homogeneous (acidic) aqueous solution of a silica precursor (alkoxysilanes) and a block copolymer (poly(ethylene oxide). The hydrolytic polycondensation of the alkoxysilanes gives rise to an increase in the Gibbs free energy that finally induces the phase separation into co-continuous fluid and gel domains via *spinodal decomposition*. The inorganic sol-gel transition can freeze this domain structure as a permanent gel morphology, preventing the system from further phase separation.

The final porous silica material is obtained by drying of the gel and removal of the polymer template via calcination. The pore structure in the micrometer range (macroporous network) is hereby determined by the fraction of the fluid phase. The gel phase is mainly composed of polymerized silica and the block copolymer and later forms the mesoporous silica skeleton.

The calcined material then exhibits a hierarchical macro- / mesoporosity. The form of the gel is determined by the shape of the reaction vessel, and thus silica monoliths of different shapes and sizes can be easily synthesized. Temperature treatment and pH value strongly effect the synthesis

procedure, and thus only exact conditions allow the generation of a defined product. [57, 74–76].

Similar to this process, we developed a synthesis for the generation of a hierarchical macro- / mesoporous carbon materials. The principles of spinodal decomposition as the driving process of the synthesis are described in the following chapter.

5.3 Spinodal decomposition

A binary phase diagram shows a miscibility gap below a critical temperature T_c when the two components A and B do not completely mix with each other. The miscibility gap is hereby defined by the *binodal curve*. Figure 5.1 shows a sketch of such a phase diagram and the corresponding Gibbs free energy of mixing $\Delta\overline{G_{mix}}$ of the mixed phase at the temperature T'. In the miscibility gap, the system can separate into its equilibrium phases by two different mechanisms, depending of the curvature of $\Delta\overline{G_{mix}}$. Starting from the equilibrium points (that define the binodal curve), the curvature within the miscibility gap is positive until the two inflection points (spinodal points that define the spinodal curve). The *spinodal curve* therefore borders the area of negative curvature values for $\Delta\overline{G_{mix}}$. Imagine a homogeneous mixture of the composition x and entering the miscibility gap from elevated temperatures, stopping at the temperature T'. The system is now about to separate into its equilibrium phases. Supposing very small fluctuations in the composition x into x^+ and x^- (Figure 5.1b). When the curvature of $\Delta\overline{G_{mix}}$ is negative, the fluctuation leads to an decrease in Gibbs free energy and therefore the system will phase separate further. This process is called *spinodal decomposition*. When the curvature of $\Delta\overline{G_{mix}}$ is positive, the fluctuation leads to an increase in Gibbs free energy. Obviously the system is "metastable" against very small fluctuations and requires larger fluctuations to start the phase separation. Such a large fluctuation occurs through the formation of a nucleus.

Summarized, no nucleation is necessary for the phase separation process

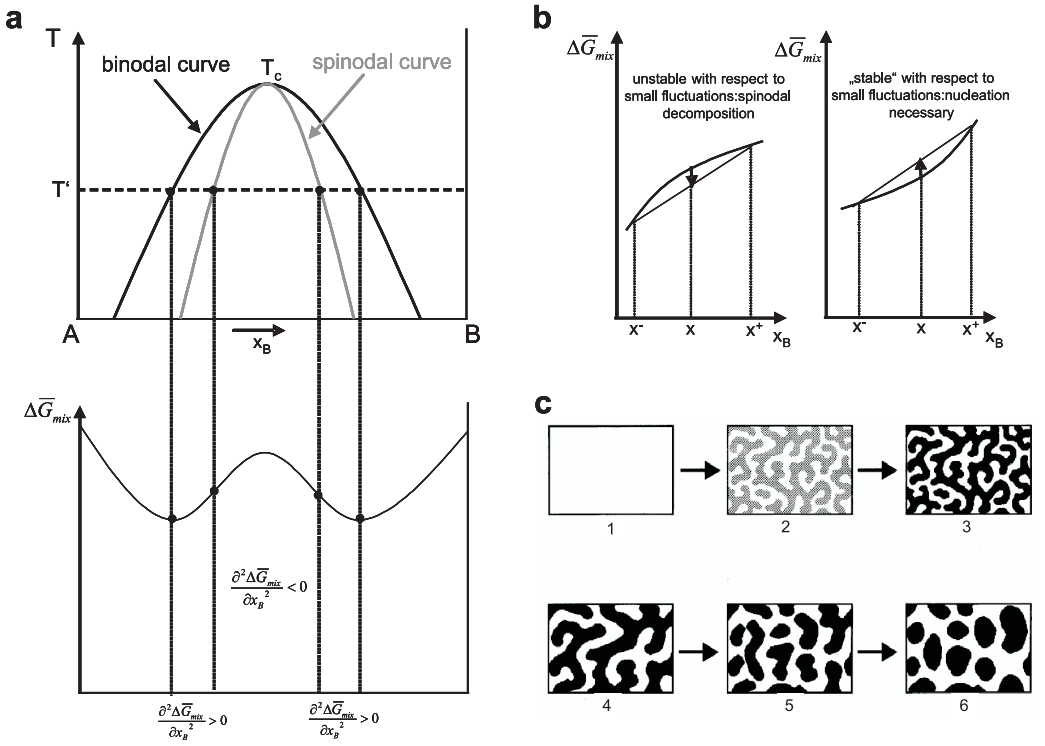

Figure 5.1: *(a)* Sketch of a phase diagram with a miscibility gap. *(b)* Small fluctuations in composition for spinodal and the binodal decomposition. *(c)* Early stages (1-3) and coarsening stages (4-6) of the structure development process by spinodal decomposition. (Fig. 5.1 *c* taken from Ref. [57])

within the spinodal curve whereas nucleation and growth mechanisms determine the area within the binodal curve [77, 78]. The final morphology of the system strongly depends on the phase separating mechanism. Spinodal decomposition leads to the formation of a co-continuous (sponge like) domain structure which ages by time (Figure 5.1c).

Imagine now a ternary system at a temperature $T < T_c$ where the components A and B are completely dissolved in a solvent C. Starting from a homogeneous solution, the spinodal decomposition can then be induced by evaporation of the solvent. The latter case was used for the synthesis of the novel hierarchical macro- / mesoporous carbon material.

5.4 Current state of research - Nanocasting of mesoporous carbon materials via soft-templating

During the last years, only few mesoporous carbon materials were synthesized by soft-templating using different strategies. For example, Ozaki et al. [79] produced porous carbon fibers starting from a polymer blend. The blend consisted of a carbonizable carbon precursor (phenolic resin) and a pyrolizable polymer (poly(vinyl butyral, PVB). After carbonization, the product exhibited notably microporosity but also showed pores in the mesopore regime. More recently, several groups reported the synthesis of ordered mesoporous carbons via self-assembly. Zhao et. al. [80] reported the formation of ordered carbonaceous mesopore structures by condensation of phenolic resin around micelles and subsequent transformation into the porous form by heat-treatment. Dai et al. [81] synthesized mesoporous carbon materials via enhanced hydrogen bonding interaction between the polyethyleneoxide (PEO) chains of F127 and different phenolic resin monomers.

Motivation

In spite of the recent progress, these strategies all rely on carbon precursors that implicate a less developed carbon microstructure (very small graphene sizes L_a and stack heights L_c), making the synthesized materials microporous and rather difficult to use for electrochemical applications. Also, the synthesized materials exhibited, until now, no hierarchical macro-/ mesoporosity.

As described in Chapter 4, a carbon material exhibiting a hierarchical macro- and mesoporosity and small micropore content is highly advantageous for electrochemical applications. To the best of our knowledge, there is no soft templating based method yet that allows the synthesis such a carbon material and thus we tried to develop one under the aforementioned challenges.

5.5 Synthesis and analysis

The novel soft-templating based method takes advantage of the phase-separation between mesophase pitch (MP, carbon precursor) and polystyrene (PS, soft template), both dissolved in tetrahydrofuran (THF). MP was chosen once more because of its exceptional carbonization behavior (Chapter 3). Polystyrene was chosen, because it exhibits the appropriate thermal behavior for the soft-templating process.

Thermogravimetry (TGA) was used to elucidate the thermal behavior of MP and PS under reductive atmosphere. As can bee seen in Figure 5.2a, polystyrene decomposes almost completely whereas carbonization of the mesophase pitch starts only at higher temperatures. The weight loss during the carbonization process can be attributed to the release of different volatile compounds (e.g. hydrocarbons, H_2 or CO). However, a successful templating is only possible when the carbonization temperature of MP is lower than the decomposition temperature of PS. Therefore, a *Lewis acid* (iron chloride, $FeCl_3$) was added as a catalyst to start the carbonization process already at lower temperatures. Figure 5.2*b* shows TGA measurements of MP and PS under the presence of $FeCl_3$. Several steps that smear out over a large temperature interval occur during the heat treatment of mesophase pitch. Unfortunately, the used TGA machine did not allow further characterization of the released compounds, but several studies showed that *Lewis acids* strongly effect the carbonization process and initiate reactions (particularly the dehydrogenation) already at lower temperatures [51,52]. Thus, the start of the cross-linking between the mesophase pitch molecules is shifted towards lower temperatures. Also, the presence of the catalyst prevents the huge volume expansion that occurs during the carbonization of mesophase pitch due to the release of volatile compounds.

As an important finding, the decomposition process of polystyrene is basically unaffected by the presence of the catalyst, and only a small residual mass of around 5 wt% was observed. The structure of this residue substance is discussed in Chapter 5.8. The weight loss at lower temperatures can be explained by evaporation of residual THF (the solvent was used to homoge-

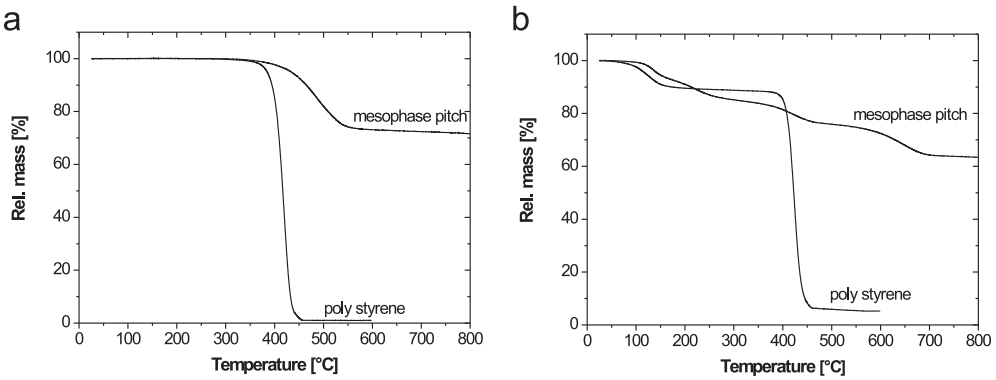

Figure 5.2: TGA measurements of mesophase pitch and polystyrene under nitrogen. *(a)* without catalyst and *(b)* with 10 wt% $FeCl_3$ as catalyst. (Heating rate of 10 K / min)

neously distribute the catalyst in the samples). Table 5.1 shows the results of the TGA measurements for the given conditions.

Thus, the chosen system consisting of MP, PS and $FeCl_3$ as catalyst fulfills the important condition that the carbon precursor starts to carbonize at temperatures below the decomposition of the soft template. It should be mentioned that decomposition and carbonization can already occur at lower temperatures when the heating rate is reduced or a constant temperature is maintained over a longer time. For example, polystyrene decomposes already at temperatures as low as 300 °C into many volatile compounds [82].

The principle and proposed mechanism of the synthesis is shown in Figure 5.3. Firstly, a template solution (PS and $FeCl_3$ in THF) and a precursor solution (MP in THF) are prepared. The solutions are then mixed together and stirred for a sufficiently long time to obtain a homogeneous solution. This solution is then poured into crucibles and the THF is evaporated at room temperature. During evaporation, the mixture enters the miscibility gap, inducing a continuously increasing incompatibility between MP and PS and the system starts to phase separate. In the spinodal case, the microphase-separation leads to the formation of a bicontinuous, sponge-like structure.

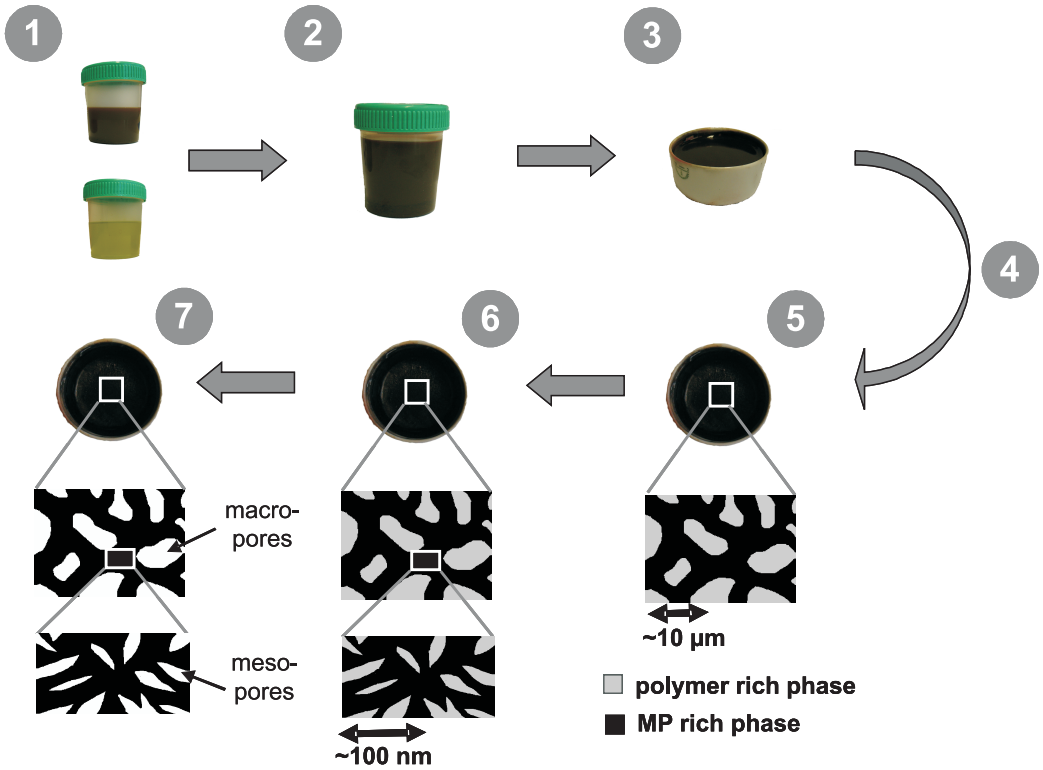

1. *Precursor solution (MP in THF) and template solution (PS + $FeCl_3$ in THF) are prepared.*
2. *Both solutions are mixed together and thoroughly stirred.*
3. *The solution is poured into a crucible.*
4. *The solvent is evaporated at room temperature.*
5. *Phase separation occurs in the macrometer scale.*
6. *First temperature treatment: Continuation of the phase separation and transformation of the MP domains into a stabilized carbon matrix.*
7. *Second temperature treatment: Decomposition of the template and final carbonization of the carbon matrix.*

Figure 5.3: New synthetic strategy and proposed mechanism for the generation of hierarchical macro- / mesoporous carbon via soft templating.

	Onset temperature [°C]	Residual mass [wt %]
Decomposition of PS	399	1.0
Carbonization of MP	426	71.5
Decomposition of PS with $FeCl_3$	408	5.22
Carbonization of MP with $FeCl_3$	$>$ 100 and $<$ 700	63.4

Table 5.1: TGA results for residual mass and onset temperatures of samples with and without catalyst. The onset temperatures refer to decomposition for PS samples and carbonization for MP samples. The heating rate was 10 K / min. The content of $FeCl_3$ was 10 wt %.

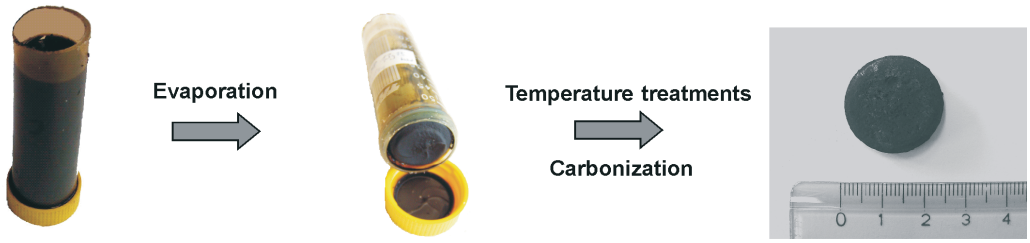

Figure 5.4: Synthesis of a monolithic carbon body (*MPPS-66-600) using the technique described in Figure 5.3.

Similar to the Nakanishi process, the phase separation is then further controlled by a suitable heat treatment. During the first heat treatment at 300 °C (stabilization step), the carbonization process of the mesophase pitch is initiated, resulting into further incompatibility between MP and PS and thus further phase separation occurs. This process is probably facilitated by the decrease in viscosity due to the increased temperature (PS melts at around 240 °C). The resulting system then consists of PS-rich and MP-rich domains on the macro- and nanometer scale. The heat treatment is maintained for a duration of 10 h. This ensures that the MP molecules slowly start to cross-link and transform into a more and more stable carbon matrix. After stabilization, the temperature is increased towards higher temperatures (600 - 800 °C). As shown in Figure 5.2, polystyrene decomposes at such high temperatures, leaving behind the desired macro- and mesoporosity. The higher

temperature also leads to the final carbonization of the carbon matrix. Due to the stabilization step, the microstructural changes within the carbon matrix remain small and closure of the mesopores is prevented.

Looking back at the different stages during spinodal decomposition (Fig. 5.1c) it is noteworthy that, on one hand, the phase separation must continue up to a certain extend to create the desired phase domains on the micro- and nanometer range. On the other hand, phase separation must be, at some point, hindered. Otherwise the phase separation would proceed in order to minimize the domain interface. The final mesoporosity would then diminish by coarsening effects.

In the present system, the different stages during spinodal decomposition can be effected during the evaporation process and during the heat treatment. In the first case, during evaporation of the solvent, the viscosity of the system increases until solidification, hindering further phase separation of the MP-rich and PS-rich domains. In the second case, during heat treatment, the phase separation is mainly determined by the $FeCl_3$ induced cross-linking of the MP molecules and the decrease in viscosity.

As an important feature, the porosity can be adjusted by variation of the soft-template content.

Alternatively, porous materials can also obtained by a single heat treatment at 340 °C for 48 hours. Due to the reduced temperature, the material is not fully carbonized and therefore a carbonaceous material.

Usually, the synthesized material was obtained in form of flakes but the use of special scaffolds also allowed the generation of monolithic carbon bodies with dimensions of up to several centimeters (Fig. 5.4). By use of a taller scaffold (here a centrifuge tube), the resulting sample was thicker, giving rise to a porous carbon monolith after the carbonization process. One can imagine that the material can be produced in various monolithic shapes either by appropriate evaporation scaffolds or also by a molding step between evaporation and carbonization. Such a process could be conducted by molding the material when it gets viscous at increasing temperatures.

Samples were denoted as MPPS-u-v, where MP and PS are mesophase

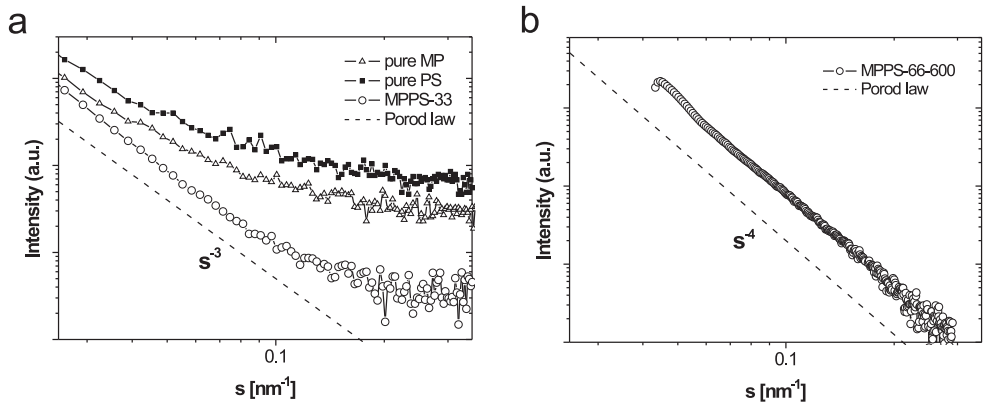

Figure 5.5: SAXS measurements of *(a)* the pure compounds and a phase separated sample after evaporation of the solvent (MPPS-33) and *(b)* a sample carbonized at 600 °C (MPPS-66-600). A *Kratky camera* with slit smearing was used for the samples shown in *(a)*, therefore the Porod law obeys s^{-3} compared to s^{-4} when a *rotating anode* was used *(b)*.

pitch and polystyrene, u the fraction of polystyrene in wt% and v the HTT (in °C). Monolithic samples are marked with the symbol "*" (e.g. *MPPS-66-600). If not specified, polystyrene with an average molecular weight of 250.000 (Acros) was used.

Since the changes in the material during phase separation obviously could not be studied in-situ by techniques such as light-scattering (the solution is black), the morphology was investigated by various techniques at the different stages of the synthesis. Small angle x-ray scattering (SAXS) allowed us to study the structural evolution on the nanometer scale throughout the process. Already the comparison of SAXS data of the mixtures after evaporation with the scattering of pure PS and pure MP showed pronounced differences (Fig. 5.5a). An almost ideal *Porod law* was observed, indicating the presence of a well-defined microphase-separated two-phase system (MP - PS) on the nanometer scale already after evaporation. The Porod law was also observed for a sample carbonized at 600 °C, proving the presence of a two-phase system between, in this case, carbon matrix and pores (Fig. 5.5b). The extend

of the Porod law up to high values for the scattering vector s supported the assumption that the phase separation process continued during the heat treatment and indicated a large surface area due to the presence of pores in the nanometer regime.

The porosity was further characterized by sorption analysis. Nitrogen sorption evidenced the presence of a reasonable concentration of mesopores, depending on the template concentration. Figure 5.6a shows the isotherms of samples templated with different relative amounts of PS. The isotherms are clearly from type IV and show distinct hysteresis. Lower polymer contents produced accordingly lower mesoporosity, thus proving that the mesoporosity originated indeed from a templating process and not from inherent porosity of the components. For instance, MPPS-66-600 showed a total pore volume $V_{tot,\ N2\text{-}Sor.} = 0.45\ cm^3\ g^{-1}$ and a BET surface area of 170 $m^2\ g^{-1}$. As an important finding, high precision nitrogen sorption analysis at low adsorption pressures indicated a minimal content of undesired micropores only. Figure 5.6b shows the corresponding cumulative pore volume, using a NLDFT model. The porosity increases significantly in the mesopore range, whereas the samples show only little porosity in the micropore range.

	BET surface area [$m^2\ g^{-1}$]	$V_{tot,\ N2\text{-}Sor.}$ [$cm^3\ g^{-1}$]	Micropore content [%]
MPPS-66-600	170	0.45	5.2
MPPS-50-600	90	0.21	6.2
MPPS-33-600	20	0.07	5.3

Table 5.2: Nitrogen sorption data for different samples MPPS-u-v, with u the fraction of template in wt%, and v the carbonization temperature. The total pore volume $V_{tot,\ N2\text{-}Sor.}$ was determined by the last point of the adsorption isotherm. The micropore content is the contribution of micropores (determined by NLDFT model) to $V_{tot,\ N2\text{-}Sor.}$ in vol%.

Also, these mesopore features strongly resembled the structural properties found for porous silica generated by the Nakanishi process. The continuous increase of porosity speaks for a relatively broad size distribution of the

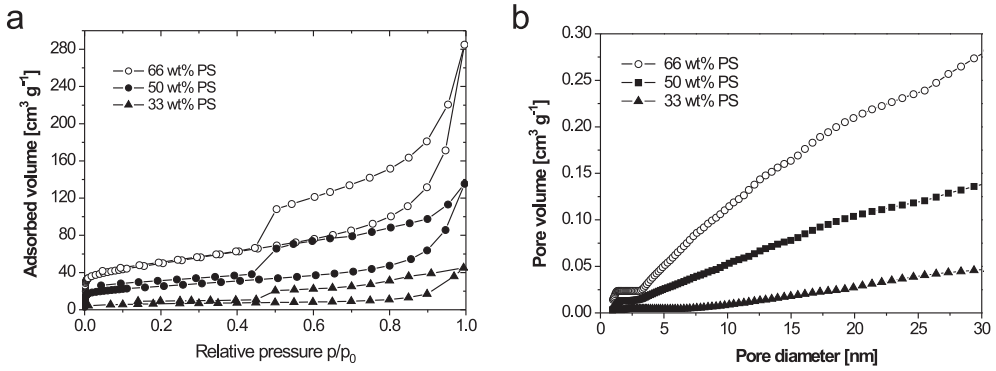

Figure 5.6: *(a)* Isotherms (obtained by nitrogen sorption) of samples with varying template concentrations. *(b)* Cumulative pore volumes applying a NLDFT model on the adsorption branch of the isotherms (assuming silica as adsorbent. *Note:* A NLDFT model assuming carbon as adsorbent was only available for the desorption branch).

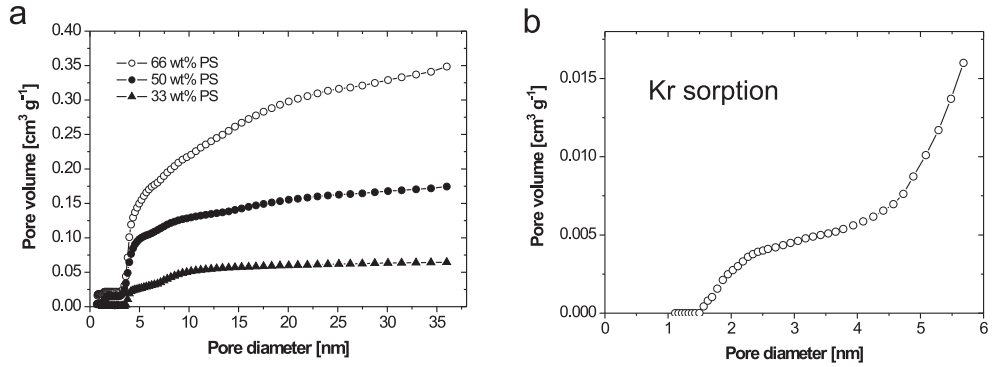

Figure 5.7: *(a)* Cumulative pore volumes for samples of different template concentration using a NLDFT model for carbon as adsorbent (desorption branch of the isotherm). *(b)* Cumulative pore volume obtained by krypton sorption for MPPS-66-600 (NLDFT, adsorption branch).

mesopores. A summary of the nitrogen sorption data is given in Table 5.2.

Further sorption analysis was done by applying a special NLDFT model that was developed for the sorption of nitrogen on carbon. Although the model could be only applied to the desorption branch of the isotherm, the results also confirmed a very low micropore content and reasonable mesoporosity (Figure 5.7a).

The low micropore content could be also verified using *Krypton sorption*. The main advantage of krypton as adsorptive is that it allows the detection of additional micropores that cannot be entered by the bigger N_2 molecules. The experiment was carried out at 77 K, which limited the maximum relative pressure to $p/p_0 = 0.6$. The used kernel therefore provided data up to a maximum pore diameter of around 6 nm. As can be seen in Figure 5.7, the fraction of pores smaller than 2 nm is very small.

Scanning electron microscopy (SEM) revealed the presence a 3-D bicontinuous structure of micrometer sized pores (macropores), quite similar to porous SiO_2 obtained by the Nakanishi process (Figure 5.8). A picture of such a porous silica is added to the figure for comparison. Hence, the morphology of the final carbon material itself provided strong evidence that the underlying transformation corresponded to spinodal decomposition of mesophase pitch and the polystyrene. SEM proved that the bicontinuous structure could be maintained throughout the carbonization process.

Figure 5.9 shows a TEM image of MPPS-66-600. The image proves the presence of nanometer sized pores in a continuous carbon matrix. The dark spots could be attributed to iron residues. The lamellar structures that can be seen in the image (pointed out by an arrow) probably originated from exfoliated carbon, also speaking for a carbon material of extended graphene sizes.

Hg porosimetry was used to characterize the porosity over a extended length scale. Figure 5.10a shows the cumulative pore volume and pore size distribution for a monolithic carbonaceous sample templated with 33 wt% PS (*MPPS-33-340). The sample exhibited a broad bimodal pore size distri-

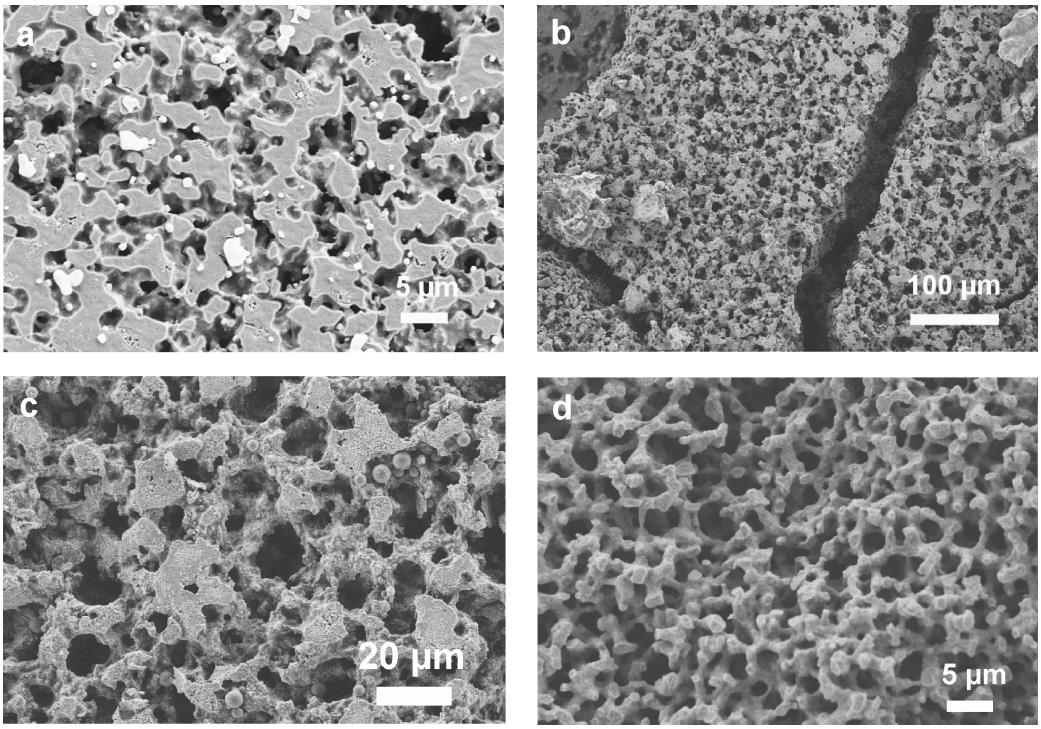

Figure 5.8: SEM images showing the macroporous structure of samples carbonized at *(a)* 600 °C (MPPS-66-600) and *(b), (c)* 340 °C (MPPS-33-340). *(d)* SEM image of porous silica made by the Nakanishi process for comparison.

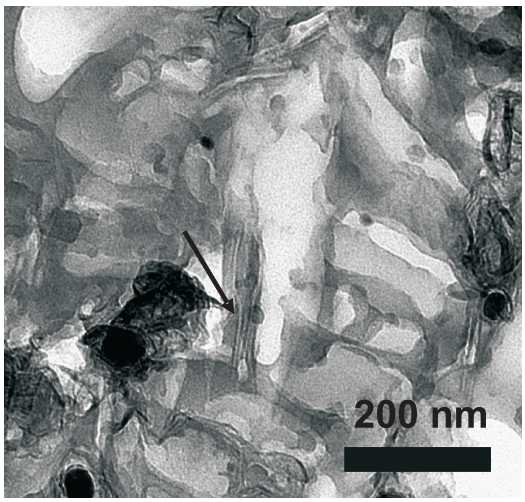

Figure 5.9: TEM (microtomy) image from MPPS-66-600

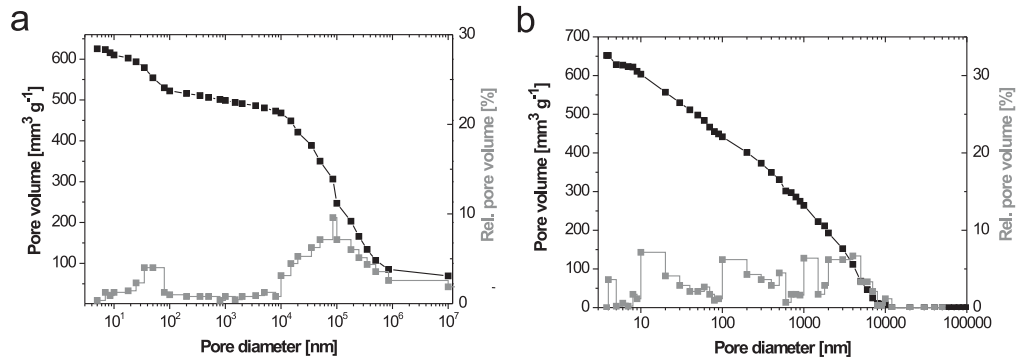

Figure 5.10: Mercury porosimetry of two samples (a) MPPS-33-340 and (b) MPPS 66-600.

bution with the first maximum in the mesopore region between 10-100 nm, confirming the N_2 sorption data. The second maximum was found in the macropore range with diameters of about 10-1000 μm. The measured total pore volume of $V_{tot,\ Hg\text{-}Por.}$= 0.63 cm^3 g^{-1} probably also resulted from cracks within the monolithic sample. However, the presence of a bimodal porosity also speaks for a phase separation similar to the NAKANISHI process.

A much broader pore size distribution was found for the samples heat treated at higher temperatures, probably due to the changes in the carbon microstructure that occurred during the heat treatment (Fig. 5.10b). A total pore volume of $V_{tot,\ Hg\text{-}Por.}$= 0.65 cm^3 g^{-1} was found for MPPS-66-600.

It has to be taken into account that the technique does not allow the detection of smaller mesopores and micropores. Thus, the most accurate way of to determine the total porosity of the sample is to add the mesopore volume derived from nitrogen sorption and the macropore volume derived from Hg-porosimetry: $V_{tot,\ sample} = V_{meso,\ N2\text{-}Sor.} + V_{macro,\ Hg\text{-}Por.}$.[1] This way, a total porosity of around 0.90 cm^3 g^{-1} was found for the sample MPPS-66-600. Elemental analysis stated a carbon content of about 72 wt%, whereas the main proportion of the rest can be attributed to iron residues. Estimating

[1] $V_{meso,\ N2\text{-}Sor.}$: The NLDFT model allowed the determination of the pore volume of pores $<$ 35 nm (Fig. 5.7a).
$V_{macro,\ Hg\text{-}Por.}$: The contribution of pores $>$ 35 nm was determined from Fig. 5.10b.

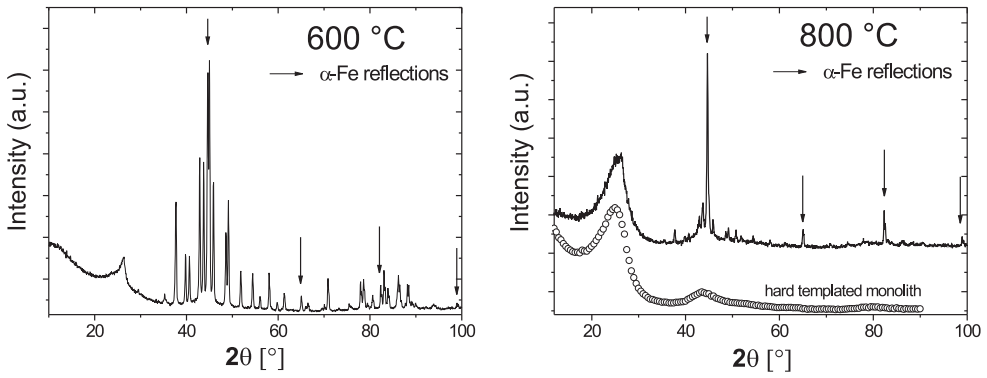

Figure 5.11: WAXS of samples carbonized at *(a)* 600 °C and *(b)* 800 °C. A WAXS pattern of a carbon monolith derived from hard templating is added for comparison (○). Reflections from $\alpha - Fe$ are marked with arrows. The other reflections originate from carbon and Fe_3C.

similar densities for carbon precursor and template and taking into account the iron residue it can be stated that the porosity indeed originated from the templating process.

In conclusion, SEM, TEM, nitrogen sorption and Hg-porosimetry clearly proved that the synthesized material exhibited a bimodal macro- / meso-porosity.

WAXS measurements were used to determine the different phases present in the samples. Figure 5.11 shows the presence of Fe_3C (Cohenite) and α-Fe as side products after heat treatment at 600 °C. α-Fe was formed by carbothermal reduction of Fe_3C. The well defined maximum around $2\theta = 26°$ revealed the good carbonization behavior of the mesophase pitch. If desired, the fraction of Fe_3C could be transformed almost completely to α-Fe by carbonization at higher temperatures (800 °C), while maintaining porosity.

Figure 5.11b also shows the WAXS pattern of a porous carbon material synthesized via the hard templating approach (Chapter 4) for comparison. The (002) reflections of both curves show a similar shape, proving that the present carbon materials originated from the same carbon precursor, i.e.

	MW 350.000	MW 250.000	MW 200.000 + 4.000
BET surface area [m^2 g^{-1}]	7	170	26
Tot. pore volume [cm^3 g^{-1}]	0.047	0.45	0.084

Table 5.3: BET surface areas for samples (MPPS-66-600) synthesized with polystyrene of different average molecular weights.

mesophase pitch. A substantial carbon residue from polystyrene would have give rise to a much broader peak. This also evidenced that most of the template decomposed during the carbonization of the mesophase pitch. The similarity between both curves also showed that the addition of $FeCl_3$ did not significantly effect the final size of the graphene stacks, in particular the stack height L_c. However, the presence of the catalyst was crucial to shift the carbonization processes towards lower temperatures.

A sheet resistivity of 14.2 Ωcm was measured for monolithic samples heat treated at 600 °C, proving that the carbon material was well carbonized and showed good electrical conductivity.

It was found that the molecular weight of the template was important for a successful templating process. Different molecular weights of PS were used to synthesize samples under otherwise identical conditions. Table 5.3 shows the influence of the molecular weight on the surface area for the different samples. Polystyrene of higher molecular weight (MW 350.000) showed a lower solubility in the solvent and probably precipitated too early so that the final mesoporosity remained small. PS of lower molecular weight (bimodal 4.000 + 200.000 (50:50 mixture)) dissolved easier but the phase separation process also did not result into a material of reasonable mesoporosity.

Thus, it seemed that within a limited set of experiments, only PS of certain molecular weight (av. MW 250.000) gave rise to the right thermodynamical behavior that allowed the appropriate (spinodal) phase separation under the given conditions i.e. evaporation at room temperature and reasonable fraction of the template.

5.6 Incorporation of Si nanoparticles into the synthesis procedure

The specific capacity of an electrode material for lithium ion batteries is mainly determined by its ability to take up lithium ions. Silicon is also part of the current research on better anode materials, since it exhibits the highest specific capacity known (4200 mA h g^{-1}) by forming an $Li_{4.4}Si$ alloy [83]. However, silicon suffers a maximum volume increase of 310 vol% during the Li uptake, resulting into internal stresses that fracture the electrode [84]. One attempt to overcome this problem is to disperse nanosized Si particles in a relatively soft carbon matrix. Such a hybrid material could resist the volume changes during cycling and would also prevent the nanoparticles from agglomeration.

An advantage of the presented synthesis is that the procedure allows the incorporation of nanoparticles from the very first step. As a prove of principle, Si nanoparticles of 50 nm in diameter were added and mixed with the precursor solution. The relative amount of Si to MP in the precursor solution was 10 wt%. The Si nanoparticles were polycrystalline with average crystallite sizes between 12-18 nm, as determined by the Scherrer equation. The synthesis was then continued as described in Chapter 5.5. WAXS measurements proved that the Si nanoparticles persisted the carbonization process at 600 °C (Fig. 5.12). The electrochemical performance of this material (MPPS-66-600_Si) is discussed in the following chapter.

5.7 Lithium insertion / extraction measurements

In order to demonstrate a potential application of the synthesized carbon materials, the samples MPPS-66-600 and MPPS-66-600_Si (including the "impurities" Fe and Fe_3C) were investigated regarding their Li insertion / extraction behavior. Fe and Fe_3C do not intercalate Li ions and thus did not contribute to the charge capacity of the material. As mentioned before, the

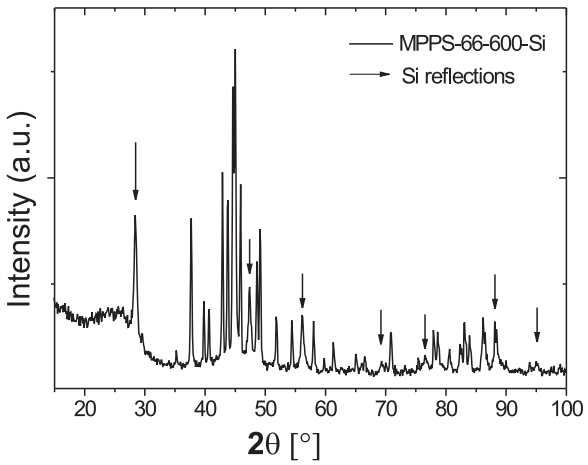

Figure 5.12: *(a)* Wide angle x-ray scattering (WAXS) of sample MPPS-66-600 containing Si nanoparticles. Si reflections are marked with arrows. The other reflections originate from carbon and Fe_3C.

carbon content of MPPS-66-600 was found to be around 72 wt%.

5.7.1 MPPS material (MPPS-66-600)

Figure 5.13a shows the discharge (Li insertion) / charge (Li extraction) curves of the sample MPPS-66-600 at rates of C/5 (one lithium per six formula units (LiC_6) in 5 hours), 1C and 5C. At a discharge / charge rate of C/5, the first charge capacity was around 470 mA h g^{-1}. As described in Chapter 2.4, the pronounced irreversible capacity in the first cycle is found in all high surface area electrode materials.

When the discharge / charge rates were increased to 1C and 5C, reversible capacities as high as 320 and 200 mA h g^{-1} were stably achieved. Furthermore, it is important to note that the cycling performance was excellent at such high rates (as shown in Fig. 5.13b), e.g. after 50 cycles, the reversible capacity retention at 1C and 5C was almost 100 % and ca. 95 %, respectively. This can be explained with the well developed carbon microstructure of MP based carbon materials (Chapter 3). Usually, non-graphitic carbons

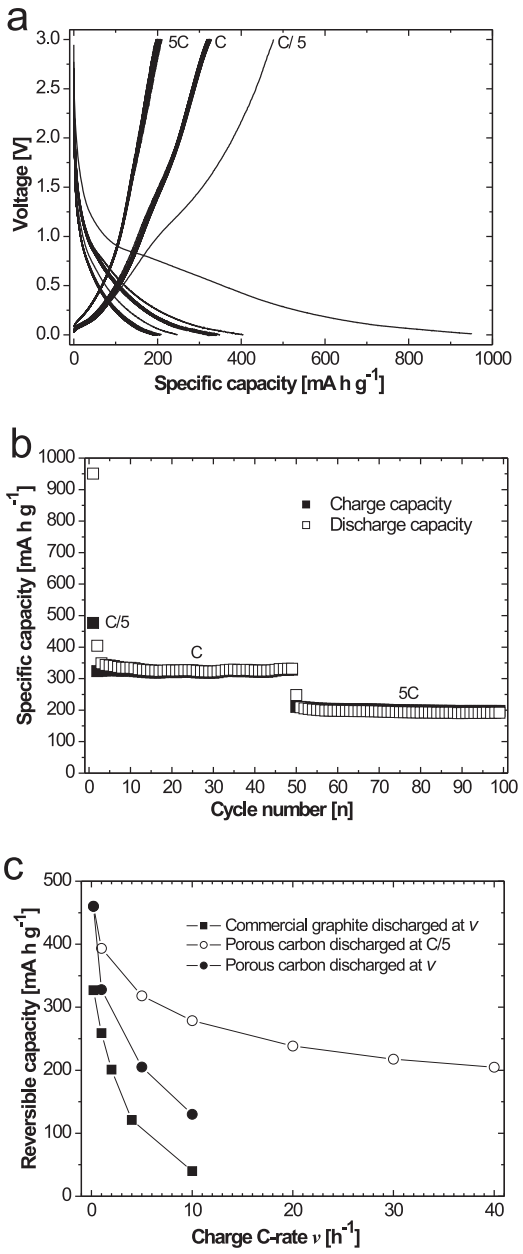

Figure 5.13: *(a)* Galvanostatic discharge (Li insertion, voltage decreases) / charge (Li extraction, voltage increases) curves the sample (MPPS-66-600) cycled at rates of C/5, 1C and 5C (electrode cycled in 1 M LiPF6 ethylene carbonate/dimethyl carbonate (1:1 by volume)), *(b)* cycling performance of porous carbon sample cycled at rates of 1C and 5C, and *(c)* comparison of rate performance between the sample and commercial natural graphite under different electrochemical conditions.

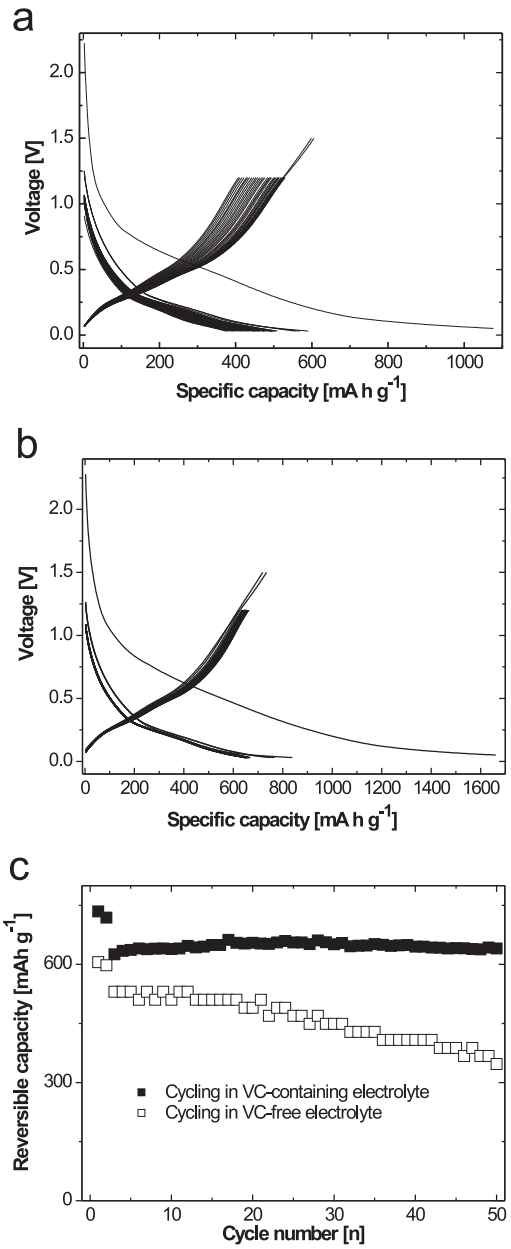

Figure 5.14: Galvanostatic discharge (Li insertion, voltage decreases) / charge (Li extraction, voltage increases) curves for the sample MPPS-66-600_Si. *(a)* Electrode cycled in the standard electrolyte. *(b)* Electrode cycled in a electrolyte containing 5 wt% vinylen carbonate (VC). *(c)* Comparison of the rate performance in both electrolytes. The C-Rate was approx. C/3.

exhibit microstructures with a much higher degree in disorder, and thus show a continuous and progressive capacity decay on cycling [42]. Figure 5.13c compares the rate performance of the synthesized material with commercial natural graphite under different electrochemical conditions. At the same discharge / charge rate, the material showed higher reversible capacity than that of commercial natural graphite. If the discharge rate was set at C/5 and the charge rate was varied from C/5 to 40 C, as shown by the open circles, much higher reversible capacities at high charge rates were observed. For instance, even at a charge rate of 40 C, a charge capacity of ca. 200 mA h g^{-1} was obtained. Applying a low C-rate for the lithium insertion process is typical for carbon materials (Chapter 2.4).

Here, it should be pointed out that the capacity of the electrochemical active carbon material was much higher, because the presence of Fe and Fe_3C lowered the total capacity of the material. For example, by excluding the weight fraction of iron (around 28 %), the first charge capacity (at C/5) referring to the active carbon material was around 650 mA h g^{-1} compared to the 470 mA h g^{-1} described above.

5.7.2 MPPS material with Si nanoparticles (MPPS-66-600-Si)

Figure 5.14a shows the discharge / charge curves for the sample MPPS-66-600-Si using the standard electrolyte. The first cycle also showed a large irreversible capacity, similar to the one observed for the sample without Si. A reversible charge capacity of around 592 mA h g^{-1} was found, proving that the addition of the Si nanoparticles gave rise to a significant increase in capacity. However, the stability was not satisfying and the experiments had to be conducted within a smaller voltage range of 1.5 V instead of 3.0 V. Furthermore the cycling performance showed a continuous decrease in capacity.

As discussed in Chapter 2.4, the battery performance can be improved by adding electrolyte additives for control of the solid electrolyte interface (SEI) formation. Here, the addition of vinylen carbonate (VC) strongly improved

the Li cycling. Figure 5.14b shows the discharge / charge curves for the VC-containing electrolyte. The influence on the SEI formation can be clearly seen by looking at the first discharge curve. The curve reaches values higher than 1600 mA h g^{-1}, but also the irreversible capacity (around 800 mA h g^{-1}) was higher compared to the standard electrolyte. The reversible charge capacity was measured to be around 726 mA h g^{-1}, which was significantly higher compared to the VC-free electrolyte. The cyclability of the material for both electrolytes is compared in Figure 5.14c. As described, the reversible capacity constantly decreased when the standard electrolyte was used. But the addition of VC gave rise to a stable cycling at a charge capacity of around 650 mA h g^{-1}.

As described in Chapter 5.7.1, the capacity of the active material (here carbon and Si) was much higher, since a substantial amount of Li insertion inactive Fe and Fe_3C was present in the sample.

5.8 Hollow carbon nanofibers from polystyrene

As shown by the TGA measurements (Chapter 5.5), polystyrene almost completely decomposed under nitrogen even in the presence of the used catalyst ($FeCl_3$). However a small fraction of around 5 wt% remained as residual. Elemental analysis showed that this residual substance consisted of 54.5 wt% C (0.6 wt% N, 0.6 wt% H, 0.0225 wt% S). It can be assumed that the remaining portion mainly consisted of iron residues.

WAXS measurements (Fig. 5.15 a) showed a pointed peak at $2\theta = 26.3°$, revealing that the carbon microstructure was highly developed and larger values for L_c could be expected. Moreover, α-Fe was detected. Figure 5.15 shows SEM and TEM images of samples heat treated for 6 hours at 700 °C. It can be seen that the fibers were hollow and appeared as bundles. The TEM image (Figure 5.15 d) shows that irons particles were found at the tip of the hollow fibers. Furthermore these fibers were also found at lower HTT (i.e. 600 °C). Nitrogen sorption experiments showed an isotherm with hysteresis. The BET surface area of the material was measured to be 390 m^2 g^{-1} (heat treated at 600 °C) indicating that the fibers were very likely to be hollow.

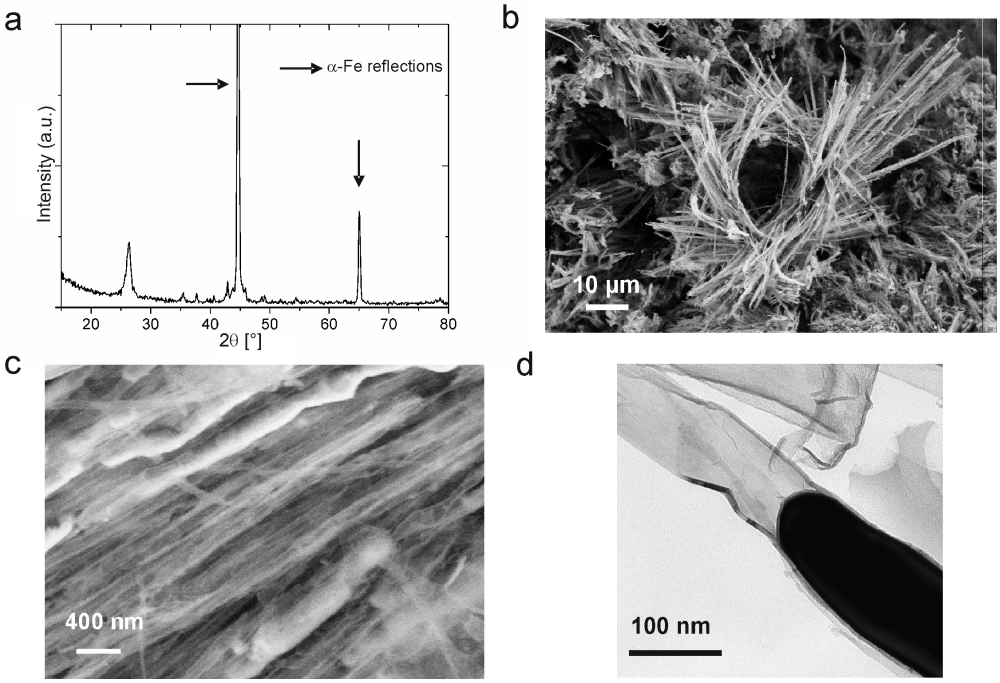

Figure 5.15: *(a)* WAXS pattern, and *(b, c)* SEM images of the carbon nanofibers. *(d)* TEM image of a carbon nanofiber with an iron particle on its tip. The sample was heat treated at 700 °C.

It is known that small metal particles (in particular Fe, Co and Ni) can catalyze the formation of carbon fibers in the nanometer range. Such fibers are of interest due to their chemical similarity to carbon nanotubes or fullerenes [85]. The mechanism can be briefly described as follows: Hydrocarbons decompose on the surface of a small metal particle into hydrogen molecules and carbon atoms. The carbon atoms diffuse through the bulk metal and precipitate on the other site in form of graphite or a similar structured carbon material. The fiber then grows through the continuous accumulation of the carbon atoms on the carbon structure. In the present case, the hydrocarbons are provided by the decomposition of the polystyrene. Hollow fibers can be observed when the graphene sheets align parallel to each other, especially when iron is used as catalyst.

So far, it could be not concluded if or to which extend these hollow fibers were present in the synthesized MPPS samples. But preliminary results

from Li insertion on these nanofibers (not shown here) suggested that their presence would have even improved the electrochemical performance.

5.9 Summary

In this chapter, the development of a new soft-templating based synthesis for the generation of porous carbon materials was presented. As the new feature, the synthesis yielded a hierarchical macro- / mesoporous carbon material, taking advantage of the phase separation between a carbon precursor (mesophase pitch) and a soft template (polystyrene). The use of a soft template allowed an easy synthesis, avoiding the expensive multi-step procedures based on hard-templating.

The porosity could be tailored by varying the weight fractions of carbon precursor and polymer template. Samples with BET surface areas up to 170 m^2 g^{-1} and a total porosity of 0.95 cm^3 g^{-1} could be synthesized.

Inexpensive chemicals were used in order to demonstrate that such porous materials can be produced at lower costs compared to hard-templated systems. As an additional feature, the synthesis allowed the generation of monolithic materials.

The low micropore content of the carbon material and the hierarchical porosity gave rise to a remarkable electrochemical performance as anode material for lithium ion batteries even including the residues of iron and iron compounds.

Additionally, it was demonstrated that the synthesis procedure allows the incorporation of nanoparticles from the very first step. In the present study, Si nanoparticles were incorporated into the carbon material that gave rise to an overall reversible charge capacity higher than 600 mA h g^{-1} for lithium storage.

Chapter 6

Conclusion

Within this work, new strategies for the synthesis of novel porous carbon materials were developed. The aim was to generate materials with high surface area in order to increase the available interface for reactions / interactions of e.g. molecules or ions with the carbon matrix. Micropores ($<$ 2 nm) are inherent defects in most of the carbon materials but had to be avoided for the current purpose, since they can act as irreversible trapping sites for ions or small molecules. Thus, a carbon material exhibiting mesopores (2 - 50 nm) was desired. Additionally, the accessibility of the mesopores was facilitated by a macroporous network, allowing fast transport of a mobile phase. Also, the synthesis of a monolithic material is beneficial, since it makes the use of a binder or e.g. conductive agents redundant. Thus, the synthesis of *hierarchical macro- / mesoporous carbon monoliths* was the main task within this work.

Since it is generally difficult to avoid micropores in carbon materials, the choice of the right carbon precursor was crucial for a successful synthesis. Thereto, different carbon precursors were evaluated in the first part of this work regarding their carbonization behavior (Chapter 3). The WAXS model proposed by Ruland and Smarsly was applied for the first time to a larger series of samples in order to determine the microstructure of the resulting carbon materials on the molecular level, i.e. the sizes of the graphene stacks. Layer size and height of the stacks were the key parameters used to de-

scribe the carbon microstructure. It was shown that the results obtained were much more accurate compared to the standard evaluation method (Raman spectroscopy). Additionally, the WAXS model allowed the determination of several other parameters such as stack height, distribution functions and polydispersities. One particular precursor, mesophase pitch, showed an exceptional carbonization behavior, yielding a carbon material with a well developed microstructure and a small content of inherent defects, i.e. micropores.

Using mesophase pitch as carbon precursor, two templating strategies were successfully developed that allowed the synthesis of the desired macro- and mesoporous carbon materials.

In the first case (Chapter 4), the porosity was generated by replication of hierarchical porous silica monoliths. The resulting carbon monoliths exhibited a very defined porosity with narrow pore size distributions for macro- and mesopores, while keeping the micropore content very low. Also, the macropores formed a 3D interconnected pore system. The synthesized material showed exceptional performance in electrochemical applications. When used as an anode material in lithium ion batteries, the carbon monoliths showed an overall performance (charge capacity, rate performance, cyclability) far better than commercial materials. The versatility of the carbon monoliths was also demonstrated by using them as support material in supercapacitors.

In the second case (Chapter 5), hierarchical macro- mesoporous carbon materials were generated by a soft-templating approach. The material was synthesized by spinodal decomposition between mesophase pitch and polystyrene, followed by a stepwise thermal treatment, and exhibited a continuous 3D macroporous network and mesopores. Also, the micropore content was very low. The synthesis procedure was comparably simple and also allowed the generation of monolithic samples. As discussed in Chapter 5.7, the performance as an anode material in lithium ion batteries was remarkable, in particular when Si nanoparticles were incorporated into the material.

Within this work, the advantages of the described hierarchical pore system were for the first time combined with the advantages of mesophase pitch

used as carbon precursor. Present carbon materials with similar porosity exhibited, until now, notable microporosity. In particular, there is no soft-templating based method reported that allows the generation of a comparable carbon material.

It was clearly shown that the synthesized materials could help to meet the demands of better materials for energy storage. Comparing both synthesis developed, the hard-templating approach yielded the more defined carbon material with better performance. On the other hand, the soft-templating based synthesis leaves much room for further improvement. The simple synthesis and the use of low-cost chemicals could open a new pathway for the production of inexpensive carbon electrode materials. One can imagine that e.g. the pore structure can be designed by varying polymer type and molecular weight. Ideally, the phase separation is conducted starting from a melt of template and carbon precursor, making the use of a solvent redundant.

Chapter 7

Appendix

7.1 Experimental details

7.1.1 Synthesis of hierarchical macro- / mesoporous carbon monoliths using hard-templating and mesophase pitch

Carbon monoliths were made by nanocasting using silica monoliths synthesized by the Nakanishi process as a hard template. Mesophase Pitch (AR, Mitsubishi Chemical Company) was used as the carbon precursor. Infiltration was performed with a concentrated precursor solution of MP in THF. MP was mixed with THF in a closed vessel in a ratio of 1:3 by weight. The mixture was first ultrasonicated for 20 min and then shaken vigorously for 3 days. The resulting dispersion was centrifuged, and the MP saturated supernatant was used for infiltration. The solution contains then about 10 wt% of the mesophase pitch. Then, the silica monolith was placed into an opened glass vessel and the solution was added (m_{silica}: $m_{MP\ solution}$ 1 : 80). Due to capillary action, the silica monoliths were easily filled with the solution. The silica monoliths were infiltrated on a horizontal shaker and were removed after almost complete evaporation of the solvent. The loaded monoliths were then slowly dried (at room temperature, over night) in quartz tubes of similar size to avoid deformation and cracking.

For carbonization, the silica / MP hybrid monoliths were heat treated with the quartz tubes at different temperatures under nitrogen flow. Temperatures between 700 °C and 1000 °C were chosen (6 h heating ramp and 6 h plateau). To remove the SiO_2 template, the monoliths were treated for 3 days with a 4 M ammonium hydrogenfluoride solution in a closed vessel under mild agitation on a horizontal shaker. Afterwards, the monoliths were washed twice with water. To remove residues of NH_4HF_2 , the monoliths were further washed one day under mild agitation with water (also in a closed vessel). The monoliths

were then rinsed with ethanol and dried at 70 °C. The obtained carbon monoliths were used as synthesized or were further carbonized at higher temperatures (1500 °C and 2500 °C).

Carbon monoliths using FA as carbon precursor were made by repeated infiltration and drying (two times) of the silica monolith. The infiltration was conducted by soaking the monolith in FA. Oxalic acid was used as catalyst (weight ratio FA : oxalic acid 230 : 1) Carbon monoliths using NA as carbon precursor were made by infiltration at 200 °C using a solution of naphthol and sulfuric acid in ethanol (weight ratio EtOH : NA : H_2SO_4 30 : 6.5 : 1). The silica monoliths were preheated in the oven. For infiltration, the monolith was covered with the solution.

7.1.2 Synthesis of hierarchical macro- / mesoporous carbon using soft-templating and mesophase pitch

Polystyrene of different molecular weights (MW 350.000, MW 250.000, MW 200.000 + 4.000) from Acros Organics was used as the polymer template. Mesophase pitch AR (Mitsubishi Chemical Company) was chosen as carbon precursor. Mesophase pitch (MP) was dissolved in THF under vigorous shaking for 3 days. The solution was centrifuged (10 min, 6500 rpm) and the supernatant solution was used for the synthesis. The supernatant contained then about 10 wt% mesophase pitch. The solution was further diluted with additional THF. Polystyrene of different molecular weights and amounts of $FeCl_3$(Aldrich) were dissolved in THF. The $FeCl_3$ content was 7 wt% compared to the weight of MP and polystyrene.

For a typical synthesis, 5 g of the mesophase pitch supernatant was diluted with 20 g of THF. 1 g of PS and 0.105 g of $FeCl_3$ were dissolved in 60 g THF. After dissolving, both solutions were mixed and stirred for 24 hours in order to gain a homogeneous solution. The long stirring time is necessary because the solution is not homogeneous after mixing. The resulting solution was then poured into crucibles (4.5 cm in diameter, 2 cm in height) and the the solvent was evaporated at room temperature in a fume hood. The evaporation and therefore the phase separation is sensitive towards external influences such as temperature changes. Also the varying air circulation at different places in the fume hood influences the speed of evaporation and it had to be taken care to maintain similar conditions for the phase separation process. After evaporation, the samples were heat treated in the same crucibles at different temperatures.

The samples were first annealed for 12 h at 300 °C under nitrogen flow (heating rate 1 K min^{-1}) for pre-condensing the mesophase pitch. For full carbonization, the samples were heated at 600 °C (or higher) under nitrogen flow for 6 hours (heating rate 1 K min^{-1}).

For synthesis of a monolith, the precursor solution was poured into a centrifuge tube with a diameter of 2.7 cm and height of 10 cm. Thereto, the bottom of the tube was cut

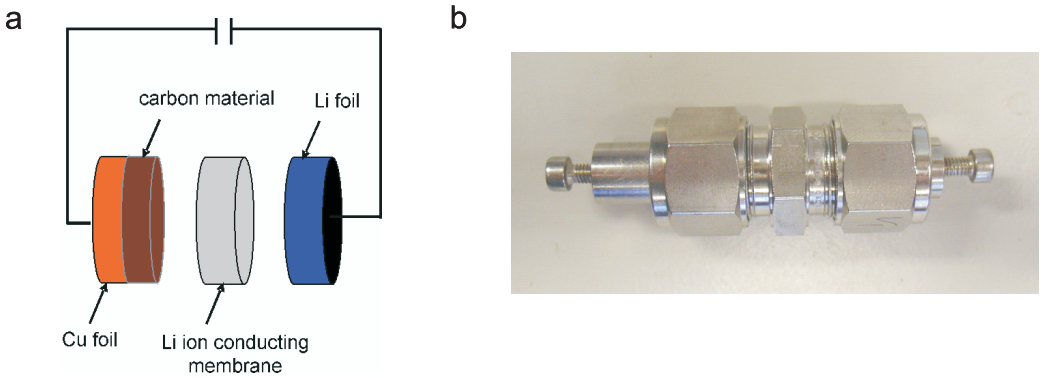

Figure 7.1: *(a)* Principle of measurement. Lithium was chosen as positive electrode. *(b)* Photograph of an assembled cell.

off and the tube was turned upside down (screw top on bottom). After evaporation of the solvent, the monolith was taken out be removing the screw top. The sample was then heat treated in a crucible of appropriate diameter that retained the shape of the monolith.

The carbonaceous material was synthesized by annealing the samples for 48 hours at 340 °C, with a heating rate of 1.5 K min^{-1}.

The software Autosorb-1 (V.1.52) was used for the NLDFT calculations. Cylindrical pores and silica as adsorbent were assumed when the model was applied for calculations from the adsorption branch. The NLDFT model for carbon as adsorbent was used for calculations from the desorption branch (the kernel is not available for the adsorption branch). Due to their conductivity, samples were not sputtered for SEM.

Hollow carbon nanofibers were obtained by heat treating a mixture of PS (MW 250.000) and 10wt% $FeCl_3$. Thereto, both compounds were mixed by dissolving them in THF. After drying, the samples were heat treated for 6h at temperatures between 600 °C and 800 °C (6h heating ramp). For a typical synthesis, 3g PS and 0.3g $FeCl_3$ were used.

7.1.3 Li-insertion / extraction measurements

Figure 7.1a shows a sketch of the principle of measurement. Metallic lithium was chosen as the positive electrode. The experiments were carried out using two-electrode Swagelok-type® cells. The photograph (Fig. 7.1b) shows an assembled cell. The working electrodes were prepared by mixing the carbon and poly (vinyl difluoride) (PVDF) at a weight ratio of 90:10 and pasting the mixture on pure Cu foil (99.6 %, Goodfellow). The geometric area and mass of the working electrode are ca. 0.79 cm^2 and 1-2 mg, respectively. The glass fiber (GF/D) from Whatman® was used as a separator. Pure lithium foil (Aldrich) was used as a counter electrode. The electrolyte consisted of a solution of 1 M $LiPF_6$ in ethylene

carbonate (EC)/dimethyl carbonate (DMC) (1:1 by volume) obtained from Ube Industries Ltd. The content of vinylen carbonate (VC) was 5 wt% for the modified electrolyte. The cells were assembled in an argon-filled glove box. Electrochemical performances were tested at different current densities in the voltage range of 0.01 - 3 V on a Arbin MSTAT battery test system.

Experiments were performed by Dr. Yong-Sheng Hu at the Max-Planck-Institute for Solid State Research, Stuttgart, Germany.

7.1.4 High temperature treatment (HTT) for WAXS analysis

Mesophase pitch, sucrose, starch were heat treated without catalyst. Sulfuric acid was added catalyst to spur the carbonization of naphthol. Thereto, naphthol was dissolved in ethanol. After adding sulfuric acid (weight ratio naphthol : H_2SO_4 6.48 : 1), the solution was dried. Oxalic acid was added as catalyst to spur the carbonization of furfuryl alcohol (weight ratio furfuryl alcohol : oxalic acid 230 : 1).

7.2 Results from WAXS modeling and Raman spectroscopy

Computation and fitting of the WAXS patterns were carried out using the software GNUPLOT. The model functions were programmed in C++ and were dynamically linked to GNUPLOT, which was installed under a Linux operation system. The Gauss-Newton fitting procedure gave only satisfactory results, thus the experimental WAXS patterns were mostly fitted manually. The Raman spectra were fitted with two pseudo-Voigt functions using the free software Fityk (Version 0.7.6.) under Windows XP.

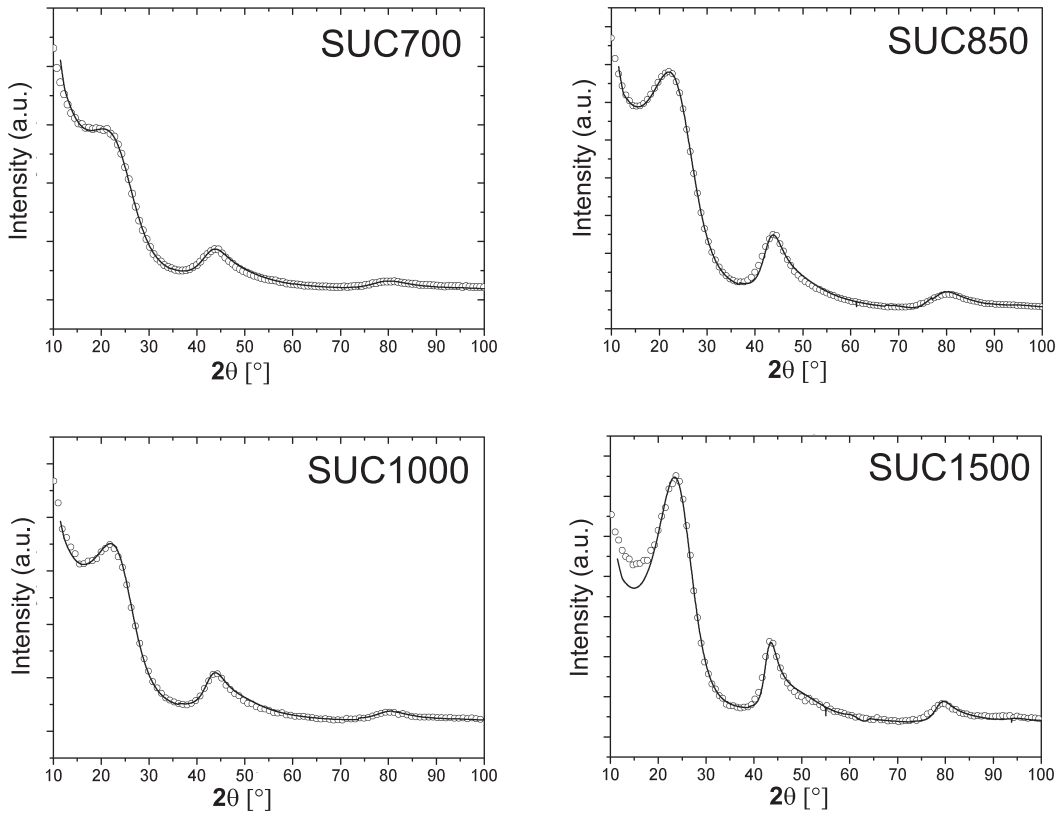

Figure 7.2: WAXS model and experimental data for samples from sucrose.

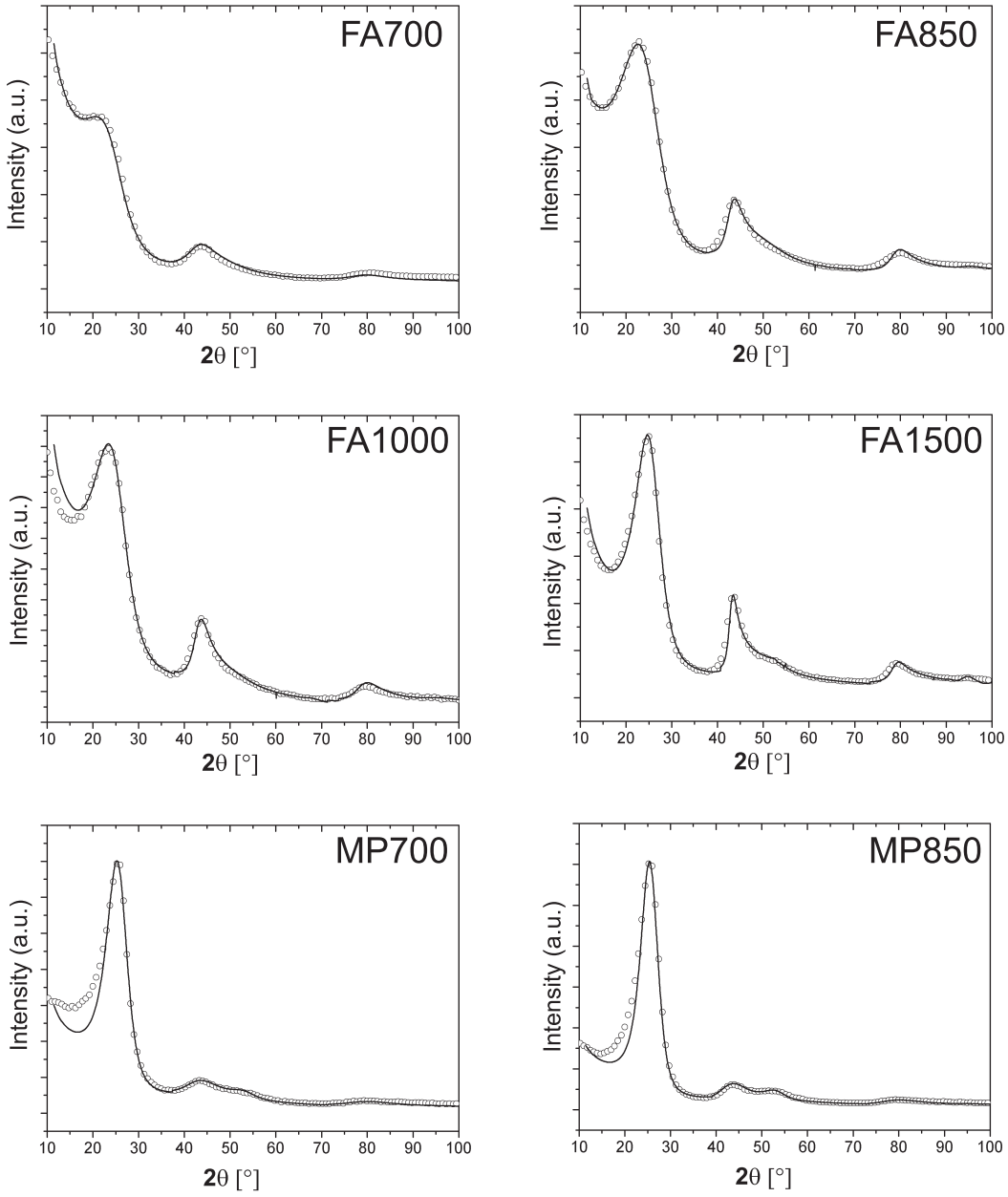

Figure 7.3: WAXS model and experimental data for samples from furfuryl alcohol and mesophase pitch.

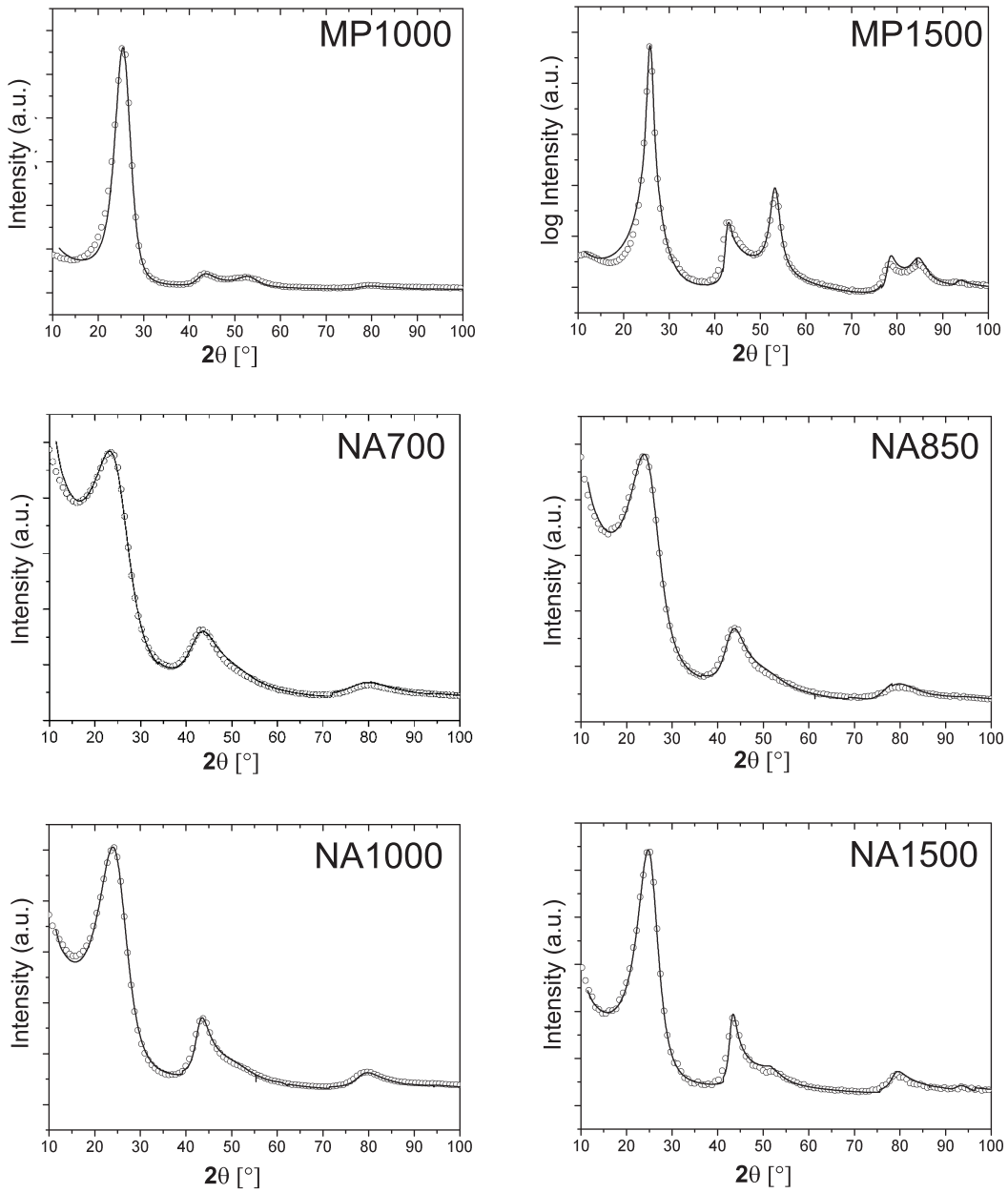

Figure 7.4: WAXS model and experimental data for samples from mesophase pitch and naphthol.

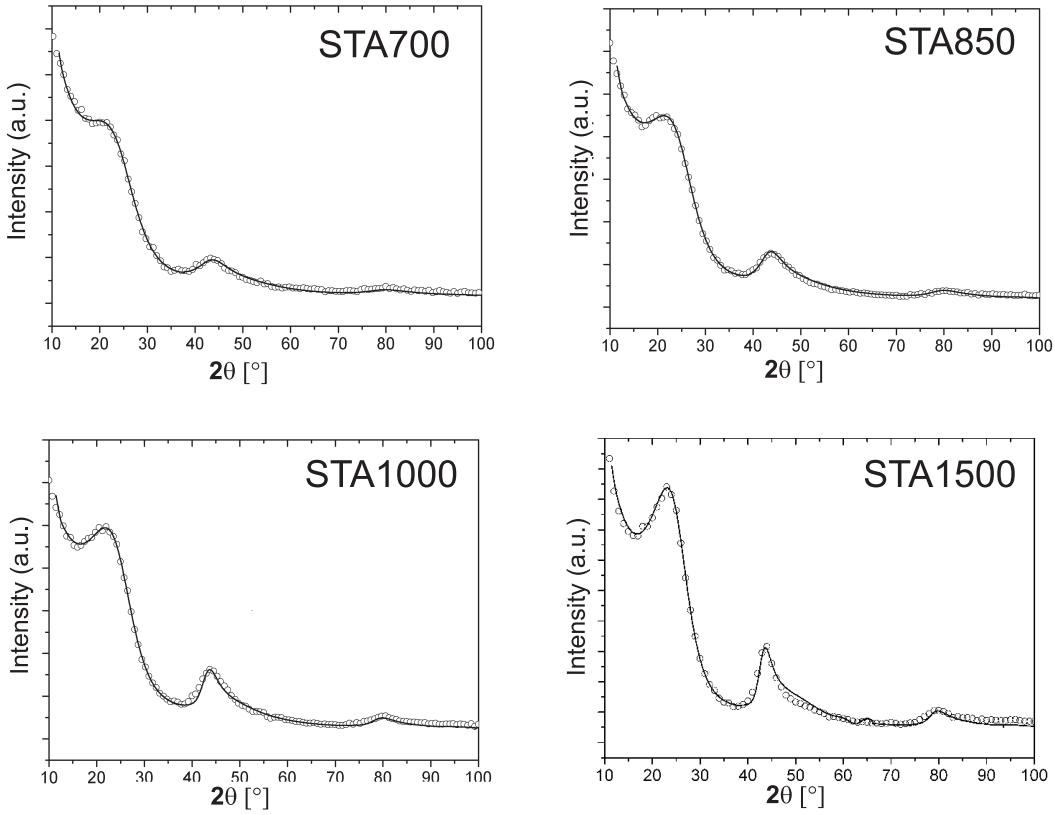

Figure 7.5: WAXS model and experimental data for samples from starch.

	q	μ	β	$a_{3,min}$	$\overline{a}_3$	η	c_n	σ_3	u_3	ν	α	ε_1	σ_1	l_{cc}
FA700	0	1.3	1.9	0.04	0.364	0.92	0.01	0.02	0.01	4.2	0.9	0	0.01	0.1401
FA850	0	2.55	2.21	0.013	0.356	0.98	0.10	0.15	0.00	3.55	1.85	0.01	0	0.1405
FA1000	0	2.42	1.76	0.02	0.351	0.95	0.11	0.018	0.029	3.5	1.7	0.02	0	0.1398
FA1500	0	1.76	1.22	0.019	0.347	0.92	0.01	0.012	0.018	5.6	1.1	0.02	0	0.1400
MP700	0.09	2.09	1.08	0.016	0.343	0.99	0.01	0.01	0.02	3.79	4.36	0.02	0	0.1405
MP850	0.16	2.4	1.05	0.008	0.343	0.99	0.01	0.017	0	19.15	11.87	0	0.007	0.1405
MP1000	0.2	2.95	0.96	0.013	0.345	0.99	0.01	0.015	0	8.52	4.17	0	0.007	0.1405
MP1500	0.38	5.75	0.32	0.018	0.345	0.99	0.01	0.015	0	12.9	1.88	0	0.007	0.1405
MP*	0.12	0.02	0.35	0.044	0.350	0.88	0.05	0.02	0.02	3.5	3.8	0.02	0	0.1420
Monolith**	0	0.43	0.62	0.018	0.349	0.99	0.01	0.021	0	5.2	2.5	0.01	0.007	0.1408

Table 7.1: Parameters of the WAXS model for samples from furfuryl alcohol (FA) and mesophase pitch (MP). Parameters $a_{3,min}$, $\overline{a}_3$, σ_3 , u_3 and l_{cc} in [nm]. μ, β and ν, α are parameters of the Gamma distributions for l and N. * Mesophase pitch before carbonization, ** Porous carbon monolith, carbonized at 1000 °C.

	q	μ	β	$a_{3,min}$	$\overline{a}_3$	η	c_n	σ_3	u_3	ν	α	ε_1	σ_1	l_{cc}
NA700	0	1.12	1.53	0.02	0.351	0.99	0.04	0.015	0.02	4.7	3.8	0.02	0	0.141
NA850	0	0.82	1.2	0.02	0.352	0.99	0.08	0.015	0.02	6.1	3.2	0.025	0	0.140
NA1000	0	1.44	1.3	0.02	0.353	0.99	0.01	0.015	0.02	4.2	1.5	0.025	0	0.140
NA1500	0	0.64	0.82	0.007	0.351	0.99	0	0.003	0.016	6.1	1.3	0.02	0	0.140
SUC700	0	2.65	2.49	0.029	0.358	0.88	0.01	0.019	0.02	4.4	3.7	0.02	0	0.140
SUC850	0	2.40	2.25	0.029	0.354	0.99	0.08	0.019	0.02	5.2	3.2	0.02	0	0.140
SUC1000	0	3.33	2.73	0.029	0.358	0.92	0.04	0.019	0.02	6.2	3.2	0.02	0	0.140
SUC1500	0	3.03	2.07	0.001	0.354	0.99	0.01	0.024	0.021	5.9	2.1	0.01	0	0.140
STA700	0	1.66	1.56	0.073	0.386	0.99	0	0.097	0.01	2.66	3.1	0	0.01	0.1399
STA850	0	1.56	1.88	0.07	0.352	0.99	0.02	0.036	0.01	3.9	2.9	0	0.01	0.1398
STA1000	0	1.85	2.03	0.07	0.353	0.99	0.09	0.034	0.01	6.1	2.8	0	0.01	0.1398
STA1500	0	0.99	1.44	0.011	0.361	0.99	0.05	0.058	0.01	9.2	3.1	0	0.01	0.1398

Table 7.2: Parameters of the WAXS model for samples from naphthol (NA), sucrose (SUC) and starch (STA). Parameters $a_{3,min}$, $\overline{a}_3$, σ_3 , u_3 and l_{cc} in [nm]. μ, β and ν, α are parameters of the Gamma distributions for l and N.

	L_c *WAXSmodel*	L_a *WAXSmodel*	L_a *Raman FWHM(*)*	L_a *Raman area(*)*	L_a *Raman FWHM(**)*	L_a *Raman area(**)*
MP700	0.98	1.1	2.06	1.55	0.70	0.80
MP850	1.11	1.69	2.17	1.72	0.68	0.76
MP1000	1.42	2.28	2.42	1.75	0.64	0.76
MP1500	7.38	7.39	4.07	2.82	0.50	0.60
FA700	0.45	1.33	2.38	1.59	0.65	0.79
FA850	0.57	2.46	2.88	1.62	0.59	0.79
FA1000	0.68	2.65	2.82	1.85	0.60	0.74
FA1500	0.78	6	4.55	2.61	0.47	0.62
NA700	0.49	1.44	2.33	1.43	0.66	0.84
NA850	0.53	2.22	2.63	1.49	0.62	0.82

Table 7.3: Average stack height L_c and average layer size L_a derived from wide-angle x-ray scattering (WAXS model) and Raman spectroscopy (* using the equation from Tuinstra & Koenig. ** using the equation from Ferrari et al. The intensity ratio was determined using full width at half maximum (FWHM) and area).

	L_c *WAXSmodel*	L_a *WAXSmodel*	L_a *Raman FWHM(*)*	L_a *Raman area(*)*	L_a *Raman FWHM(**)*	L_a *Raman area(**)*
NA1000	0.66	3.47	3.12	1.97	0.57	0.71
NA1500	0.7	5.46	5.26	2.38	0.44	0.65
SUC700	0.52	1.44	2.06	1.25	0.70	0.90
SUC850	0.53	2.25	2.39	1.35	0.65	0.86
SUC1000	0.56	2.29	2.49	1.47	0.63	0.82
SUC1500	0.69	3.61	3.44	2.36	0.54	0.65
STA700	0.66	1.18	2.09	1.51	0.69	0.81
STA850	0.48	1.69	2.31	1.51	0.66	0.82
STA1000	0.5	2.54	2.34	1.68	0.65	0.77
STA1500	0.5	3.29	4.28	2.59	0.48	0.62

Table 7.4: Average stack height L_c and average layer size L_a derived from wide-angle x-ray scattering (WAXS model) and Raman spectroscopy (* using the equation from Tuinstra & Koenig. ** using the equation from Ferrari et al. The intensity ratio was determined using full width at half maximum (FWHM) and area).

7.3 Instrumental details

X-ray diffraction (WAXS and SAXS) A D8 Advance machine from Bruker instruments was used for the WAXS measurements. The x-ray tube, operated at 40 kV and 40 mA, emitted Cu-Kα radiation that was monochromatized by a multilayer Göbel mirror. A energy dispersive detector (Sol-X, Bruker) was used to ensure low background noise via the exclusion of inelastically scattered photons. Samples were finely grinded and measured on silicon or deepened plastic samples holders. The measurements were performed in reflection geometry as coupled θ-2θ scans between 10° - 100°.

SAXS experiments (using Cu-Kα radiation) were performed using a Kratky camera from Anton Paar, Germany and a rotating anode machine with a two-dimensional marccd detector.

Sorption experiments Nitrogen sorption experiments were carried out at 77 K using a Tristar 3000 machine from Micromeritics and a Autosorb-1 machine from Quantachrome. The latter one was used for micropore analysis and Krypton sorption experiments. Evaluation of the obtained data was done by using classical BET, BJH and NLDFT models. For micropore analysis, 35 points at relative pressures p / $p_0 < 0.1$ were recorded during the adsorption process.

The software Autosorb-1 (V. 1.52) was used for the evaluation of the isotherms. Different NLDFT models were applied, depending on the evaluation of the adsorption and desorption branch. Cylindrical pores and silica as adsorbent were assumed for evaluation of the adsorption branch. Slit-like and cylindrical pores and carbon as adsorbent were assumed for evaluation of the desorption branch. A carbon model for the adsorption branch was not available. Krypton sorption experiments were carried out at 77 K, assuming nitrogen as adsorbate and cylindrical pores.

Samples were degassed at 150 °C for several hours before measuring.

Electron microscopy (EM) The SEM instrument used in this work was a LEO 1550-Gemini from LEO GmbH, Oberkochen, with an acceleration voltage from 0.1kV to 30kV and a magnification between 20 and 900.000. Non conductive samples were sputtered with gold.

A EM 912 Omega machine from Carl-Zeiss, Oberkochen (acceleration voltage 120kV, magnification 80-500.000) was used in this work for TEM. Samples were measured on carbon coated copper grids (400 mesh).

HRTEM / EELS measurements were made by Dr. Jens-Oliver Müller at the Fritz-Haber-Institute, Berlin.

Raman spectroscopy Raman spectra were obtained using a confocal Raman mi-

croscope CRM-200 from WITec, Germany. A diode-pumped green laser ($\lambda_L = 532$ nm) was used for the measurements. The beam intensity was reduced to prevent thermal damage of the samples. Samples were finely grinded and pressed to pellets prior measurement.

Elemental analysis (EA) A Vario EL Elementar instrument from Elementar Analysensysteme, Germany was used to determine the content of carbon, hydrogen, sulfur and nitrogen in the samples.

Thermogravimetric analysis (TGA) Thermogravimetric analysis were made using a TG 209 F1 machine from Netzsch. Samples were measured in Al_2O_3 crucibles and nitrogen or oxygen gas flow (15 ml / min).

Conductivity measurements The specific sheet resistivity was measured by a four-probe method using a digital multimeter Keithley 2000.

Carbonization procedure Carbonization at temperatures ≤ 1000 °C was carried out under nitrogen flow in a chamber kiln (N7/H) from Nabertherm GmbH, Germany. Some samples that were carbonized at 1000°C were further heat treated at higher temperatures. A vacuum oven from HTM Reetz GmbH, Germany was used for carbonization at 1500°C (heating rate of 10 K / min, plateau 1.5 h). Graphitization at 2500 °C (heating rate of 20 K / min, plateau 3 h) was conducted under He using a Labmaster FP20 from Thermal Technology.

7.4 List of abbreviations and symbols

BET	Brunauer, Emmett, Teller	SAXS	small-angle x-ray scattering
FA	furfuryl alcohol	SEI	solid electrolyte interface
HPLC	high-pressure liquid chromatography	SEM	scanning electron microscopy
HTT	high temperature treatment	STA	starch
MP	mesophase pitch	SUC	sucrose
NA	naphthol	TEM	transmission electron microscopy
NLDFT	non-local density functional theory	THF	tetrahydrofuran
PANI	polyaniline	TGA	thermogravimetric analysis
PR	phenolic resin	VC	vinylen carbonate
PS	polystyrene	WAXS	wide-angle x-ray scattering

Table 7.5: List of abbreviations.

$\overline{a}_3$	average interlayer spacing	σ_1, σ_3	disorder parameter
L_a	average layer size	ε_1	strain parameter
$a_{3,min}$	minimum of interlayer spacing	η	homogeneity of the stacks
L_c	average stack height	u_3	root mean square displacement of a layer in the direction perpendicular to the layer plane caused by thermal motion
κ_a	polydispersity of the chord length	c_n	concentration of non-organized carbon
κ_c	polydispersity of the stack height	q	parameter of preferred orientation
l_{cc}	average C-C bond length	κ_R	polydispersity of the radii
a, c	hexagonal lattice constant	l	chord length
N	number of graphenes each stack		
p/p_0	relative pressure	θ	scattering angle
s	scattering vector	ν	C-Rate (charge / discharge rate)
V	voltage and pore volume	I	intensity

Table 7.6: List of symbols.

7.5 List of publications, patents and presentations

Publications

- *Wide-angle x-ray scattering (WAXS) and structural analysis of non-graphitic carbon;* P. Adelhelm, B. Smarsly, M. Antonietti et al.; (in preparation)
- *Hierarchical macro /- mesoporous carbon monoliths by a simple replication technique using mesophase pitch as carbon precursor*; P. Adelhelm, B. Smarsly, M. Antonietti et. al. (in preparation)
- *Generation of hierarchical meso-/macroporous carbon from mesophase pitch by spinodal decomposition with polymer templates*; P. Adelhelm, L. Chuengchom, M. Antonietti, B. Smarsly, Y. Hu, J. Maier; Adv. Mater.; (submitted)
- *High electroactivity of polyaniline in supercapacitors by using hierarchically porous carbon monolith as support;* L.-Z Fan, Y.-S. Hu, J. Maier, P. Adelhelm, B. Smarsly, M. Antonietti; Adv. Funct. Mater., 2007; (in press)
- *Synthesis of hierarchically porous carbon monoliths with highly ordered microstructure and their application in rechargeable lithium batteries with high rate capability*; Y. Hu, P. Adelhelm, B. Smarsly, S. Hore, M. Antonietti, J. Maier; Adv. Funct. Mater., 2007; (in press)
- *Synthesis and characterization of SiC materials with hierarchical porosity obtained by replication techniques;* K. Sonnenburg, P. Adelhelm, M. Antonietti, B. Smarsly, R. Nöske, P. Strauch; Phys. Chem. Chem. Phys., 2006, 8, 3561

Patents

- *Synthesis of porous carbon with adjustable hierarchical porosity by templating of carbon precursors with linear hydrophobic polymers;* Markus Antonietti, Bernd Smarsly, Philipp Adelhelm, Karin Cabrera; DPA Nr. EP: 06011198

- *Herstellung graphitischer Kohlenstoffe mit hierarchischer Porosität und deren Einsatz als Anode in Batteriematerialien mit höchster Speicherdichte und verbesserter Lade/Entladecharakteristik*; Markus Antonietti, Bernd Smarsly, Philipp Adelhelm, Joachim Maier, Sarmimala Hore, Yongsheng Hu; DPA Nr. EP: 06018886

Presentations

- *Li-Insertion in hierarchical macro-mesoporous carbon monoliths;* Carbon 2007, International Carbon Conference, Seattle, July 2007

- *Synthesis of hierarchical macro-mesoporous carbon by spinodal decomposition;* Carbon 2007, International Carbon Conference, Seattle, July 2007

- *Structural changes in non-graphitic carbon during carbonization: Evaluation by a novel approach model for the wide-angle x-ray scattering*; Carbon 2006, The International Carbon Conference, Aberdeen, July 2006

- *New mesoporous carbons - Synthesis and Applications*; International Symposium on Inorganic Interfacial Engineering, Stockholm, June 2006

- *Mesoporous carbon monoliths - A high performance material for various applications;* ENERCHEM Meeting, October 2005

Award

- Brian Kelly Award 2007 from the British Carbon Group.

7.6 Acknowledgment

Hier möchte ich allen danken, die mich während der Arbeit begleitet haben und mit eine so schöne Zeit am Institut ermöglicht haben.

Danken möchte ich zuerst Prof. Dr. Markus Antonietti für die Möglichkeit, meine Doktorarbeit am MPI-KG durchführen zu können. Über die ausgezeichnete Betreuung und die nette Atmosphäre am Institut habe ich mich sehr gefreut.

Ein großes Dankeschön geht an meinen direkten Betreuer, Prof. Dr. Bernd Smarsly. Seine Betreuung war hervorragend und er war trotz seiner großen Gruppe immer zur Stelle wenn Fragen auftauchten. Mit seinen Ideen trug er wesentlich zum Erfolg der Arbeit bei. Außerdem denke ich gerne an die sportlichen Herausforderungen vor dem Chez Briel zurück. Für seine Stelle in Gießen wünsche ich ihm alles Gute.

Unserem Kooperationspartner in Stuttgart (Prof. Dr. Joachim Maier, Dr. Yong-Sheng Hu und Dr. Li-Zhen Fan) möchte ich für die erfolgreiche Zusammenarbeit innerhalb des ENERCHEM Projektes danken. Insbesondere Yong-Sheng Hu danke ich für seine vielen Messungen und wünsche ihm viel Erfolg für seine Arbeit in den USA. Ebenso gilt mein Dank Dr. Jens-Oliver Müller vom Fritz-Haber-Institut in Berlin für seine HRTEM Aufnahmen.

Ebenso möchte ich mich bei Dr. Karin Cabrera (Merck KGaA, Darmstadt) für die Unterstützung und die Hg-Porosimetrie-Messungen bedanken.

Bedanken müchte ich mich auch bei den vielen Technikern, die mich während der Arbeit unterstützt haben. Insbesondere gilt hier mein Dank Regina Rothe, Rona Pitschke, Heike Runge, Ingrid Zenke, Irina Shekova und Syliva Pirok.

Für Tips bei der Arbeit möchte ich mich noch bei Magda für die Einweisung in die Welt des Fluorwasserstoff, bei Michael für das Korrek-

turlesen und bei Jörg für die Latex-Rettung bedanken. Außerdem geht ein Dankeschön and Helena, die zeitgleich an ihrer Doktorarbeit schrieb und damit alles ein bisschen einfacher machte.

Herrn Dr. Ernst-Peter Resewitz danke ich für die interessante Zusammenarbeit bei den in-situ Sorptionsmessungen.

Ganz besonders möchte ich meinen Freunden und Kollegen danken, mit denen ich in und vor allem auch außerhalb des Institutes soviel Spaß hatte. Ich hoffe, auch in der Zukunft noch was von euch zu hören und zu sehen. Ein großes Dankeschön geht an: Mattijs, Magda, Miles, Helena, Emre, Jelena, Ana, Anja, Michael, Laem, Özlem, Saroj, Nicole, Julia, Simone, Pedro, Anna, Philippe, Pierre, Sebastien, Pantea, Farnoosh, Frederic, Rezan, Arne, Hans, Antonio, Cecile, Jörg, Audree, Rainer, Cara, Thorsten, Sofia, Silke, Munish, Yrong, Andreas, Kirstin, Jens & Jens, Samira, Igor, Steffen....

Meinen Eltern möchte ich ganz herzlich für ihre Unterstützung danken, vor allem während ich die Arbeit verfasst habe. Meinem Vater danke ich für sein Interesse an meiner Arbeit. Ein Dankeschön geht auch an meinen Bruder, der mir bei einigen Fragen unkompliziert weiterhelfen konnte.

Für die super Zeit in den letzten Jahren geht ein liebes Dankeschön an Hilke nach Groningen, ich freu mich riesig auf Holland. :-)

Bibliography

[1] R. H. Baughman, A. A. Zakhidov, and W. A. de Heer. Carbon nanotubes - the route toward applications. *Science*, 297:787–792, 2002.

[2] H. J. Dai. Carbon nanotubes: Opportunities and challenges. *Surface Science*, 500:218–241, 2002.

[3] R. Taylor and D. R. M. Walton. The chemistry of fullerens. *Nature*, 363:685–693, 1993.

[4] A. W. Jensen, S. R. Wilson, and D. I. Schuster. Biological applications of fullerenes. *Bioorganic and Medicinal Chemistry*, 4:767–779, 1996.

[5] Thieme Chemistry. *Roempp Chemie Lexikon*. Georg Thieme Verlag KG, 2006.

[6] H. Marsh. *Introduction to Carbon Science*. Butterworth & Co., 1989.

[7] Michael Ströck. GNU Free Documentation License, 2006.

[8] A. V. Rode, E. G. Gamaly, A. G. Christy, J. G. F. Gerald, S. T. Hyde, R. G. Elliman, B. Luther-Davies, A. I. Veinger, J. Androulakis, and J. Giapintzakis. Unconventional magnetism in all-carbon nanofoam. *Physical Review B*, 70, 2004.

[9] D. Ugarte. Curling and closure of graphitic networks under electron-beam irradiation. *Nature*, 359:707–709, 1992.

[10] T. Burchell. *Carbon Materials for Advanced Technologies*, volume 1. Pergamon, 1999.

[11] W. Ruland and B. Smarsly. X-ray scattering of non-graphitic carbon: an improved method of evaluation. *Journal of Applied Crystallography*, 35:624–633, 2002.

[12] S. Flandrois and B. Simon. Carbon materials for lithium-ion rechargeable batteries. *Carbon*, 37:165–180, 1999.

[13] V. S. Bagotzky, N. V. Osetrova, and A. M. Skundin. State-of-the-art and major scientific and engineering problems. *Russian Journal of Electrochemistry*, 39:919–93, 2003.

[14] S. Polarz and M. Antonietti. Porous materials via nanocasting procedures: innovative materials and learning about soft-matter organization. *Chemical Communications*, 22(22):2593–2604, Nov 21 2002.

[15] A. H. Lu and F. Schuth. Nanocasting: A versatile strategy for creating nanostructured porous materials. *Advanced Materials*, 18(14):1793–1805, Jul 18 2006.

[16] R. A. Caruso. Nanocasting and nanocoating. *Topics in Current Chemistry*, 226:91–118, 2003.

[17] R. Ryoo, S. H. Joo, and S. Jun. Synthesis of highly ordered carbon molecular sieves via template-mediated structural transformation. *J. Phys. Chem. B*, 103:7743–7746, 1999.

[18] H. F. Yang and D. Y. Zhao. Synthesis of replica mesostructures by the nanocasting strategy. *J. Mater. Chem.*, 15(12):1217–1231, 2005.

[19] J. Lee, J. Kim, and T. Hyeon. Recent progress in the synthesis of porous carbon materials. *Advanced Materials*, 18(16):2073–2094, Aug 18 2006.

[20] W. Ruland. *X-ray Diffraction Studies on Carbon and Graphite.* Chemistry and Physics of Carbon, Vol. 4, 1968.

[21] P. Y. Yu and M. Cardona. *Fundamentals of Semiconductors.* Springer Verlag, 1996.

[22] A. C. Ferrari and J. Robertson. Interpretation of raman spectra of disordered and amorphous carbon. *Physical Review B*, 61:14095–14107, 2000.

[23] F. Tuinstra and J. L. Koenig. Raman spectrum of graphite. *The Journal of Chemical Physics*, 53:1126, 1970.

[24] M. J. Matthews, M. A. Pimenta, G. Dresselhaus, M. S. Dresselhaus, and M. Endo. Origin of dispersive effects of the raman d band in carbon materials. *Physical Review B*, 59:R6585–R6588, 1999.

[25] G. A. Zickler, B. Smarsly, N. Gierlinger, H. Peterlik, and O. Paris. A reconsideration of the relationship between the crystallite size la of carbons determined by x-ray diffraction and raman spectroscopy. *Carbon*, 44:3239–3246, 2006.

[26] Rouquerol F. Rouquerol J., Sing K. *Adsorption by Powders and Porous Solids*. Academic Press, 1999.

[27] K.S.W. Sing and S.J. Gregg. *Adsorption, Surface Area and Porosity*. Academic Press, 2 edition, 1982.

[28] K. S. W. Sing. Adsorption methods for the characterization of porous materials. *Adv. Colloid Interface Sci.*, 77:3–11, Jul 1998.

[29] S. Brunauer, P. H. Emmett, and E. Teller. Adsorption of gases in multimolecular layers. *J. Am. Chem. Soc.*, 60:309–319, Jan-Jun 1938.

[30] K. S. W. Sing. *Surface area determination*. Butterworths, 1970.

[31] K. S. W. Sing. *in Colloid Science*. Chemical Society London, 1973.

[32] E. P. Barrett, L. G. Joyner, and P. P. Halenda. The determination of pore volume and area distributions in porous substances: 1. computations from nitrogen isotherms. *J. Am. Chem. Soc.*, 73(1):373–380, 1951.

[33] A. G. Foster. The sorption of condensible vapours by porous solids. part i. the applicability of the capillary theory. *Transactions of The Faraday Society*, 28:0645–0656, 1932.

[34] C. Lastoskie, K. E. Gubbins, and N. Quirke. Pore-size distribution analysis of microporous carbons - a density-functional theory approach. *Journal of Physical Chemistry*, 97(18):4786–4796, May 6 1993.

[35] Everett D. H. Nutall S. Brown A. J., Burgess C. G. V. *Characterization of Porous Solids IV*. The Royal Society of Chemistry, 1997.

[36] *Autosorb-1 Operating Manual V1.50*.

[37] Matthias Thommes. *Physical Adsorption: Characterization of ordered and amorphous mesoporous materials*. Imperial College Press, 2004.

[38] J. M. Tarascon and M. Armand. Issues and challenges facing rechargeable lithium batteries. *Nature*, 414:359–367, 2001.

[39] X. Y. Song, K Kinoshita, and T. D. Tran. Microstructural characterization of lithiated graphite. *Journal of the Electrochemical Society*, 143:L120–L123, 1996.

[40] M. Winter, J. O. Besenhard, M. E. Spahr, and P. Novak. Insertion electrode materials for rechargeable lithium batteries. *Advanced Materials*, 10:725–763, 1998.

[41] Y. Matsumura, S. Wang, and J. Mondori. Interactions between disordered carbon and lithium in lithium ion rechargeable batteries. *Carbon*, 33:1457–1462, 1995.

[42] J. R. Dahn, T. Zheng, Y. H. Liu, and J. S. Xue. Mechanisms for lithium insertion in carbonaceous materials. *Science*, 270:590–593, 1995.

[43] S. S. Zhang. A review on electrolyte additives for lithium-ion batteries. *Journal of Power Sources*, 162:1379–1394, 2006.

[44] M. Wachtler, J. O. Besenhard, and M. Winter. Tin and tin-based intermetallics as new anode materials for lithium-ion cells. *Journal of Power Sources*, 94:189–193, 2001.

[45] Q. Wang, H. Li, X. J. Huang, and L. Q. Chen. Determination of chemical diffusion coefficient of lithium ion in graphitized mesocarbon microbeads with potential relaxation technique. *Journal of the Electrochemical Society*, 148:A737–A741, 2001.

[46] M. D. Levi and D. Aurbach. Diffusion coefficients of lithium ions during intercalation into graphite derived from the simultaneous measurements and modeling of electrochemical impedance and potentiostatic intermittent titration characteristics of thin graphite electrodes. *Journal of Physical Chemistry B*, 101:4641–4647, 1997.

[47] A.M. Glauert. *Practical Methods in Electron Microscopy*, volume 12 of *Electron Diffraction: An Introduction for Biologists*. Elsevier, 1987.

[48] http://goldbook.iupac.org/, 2007.

[49] I. C. Lewis. Chemistry of pitch carbonization. *Fuel*, 66:1527–1531, 1987.

[50] R. A. Greinke. Early stages of petroleum pitch carbonization - kinetics and mechanisms. *Chemistry and Physics of Carbon*, 24:1–43, 1994.

[51] J. P. Boudou, D. Begin, E. Alain, G. Furdin, J. F. Mareche, and A. Albiniak. Effects of fecl3 (intercalated or not in graphite) on the pyrolysis of coal or coal tar pitch. *Fuel*, 77:601–606, 1998.

[52] B. K. Mazumdar, D. D. Banerjee, and G. Ghosh. Coal zinc-chloride reaction - an interpretation. *Energy and Fuels*, 2:224–230, 1988.

[53] A. C. Ferrari, J.C. Meyer, V. Scardaci, C. Casiraghi, M. Lazzeri, F. Mauri, S. Piscanec, D. Jiang, K. S. Novoselov, S. Roth, and A. K. Geim. Raman spectrum of graphene and graphene layers. *Physical Review Letters*, 97, 2006.

[54] Y. Lifshitz. Pitfalls in amorphous carbon studies. *Diamond and Related Materials*, 12:130–140, 2003.

[55] C. T. Kresge, M. E. Leonowicz, W. J. Roth, J. C. Vartuli, and J. S. Beck. Ordered mesoporous molecular-sieves synthesized by a liquid-crystal template mechanism. *Nature*, 359:710–712, 1992.

[56] S. J. Han and T. Hyeon. Novel silica-sol mediated synthesis of high surface area porous carbons. *Carbon*, 37:1645–1647, 1999.

[57] N. Ishizuka, H. Minakuchia, K. Nakanishi, N. Soga, and N. Tanaka. Designing monolithic double-pore silica for high-speed liquid chromatography. *Journal of chromatography*, 797:133–137, 1998.

[58] A. Taguchi, J. H. Smatt, and M. Linden. Carbon monoliths possessing a hierarchical, fully interconnected porosity. *Advanced Materials*, 15:1209, 2003.

[59] A. H. Lu, J. H. Smatt, and M. Linden. Combined surface and volume templating of highly porous nanocast carbon monoliths. *Advanced Functional Materials*, 15:865–871, 2005.

[60] A. H. Lu, W. C. Li Li, W. Schmidt, and F. Schuth. Fabrication of hierarchically structured carbon monoliths via self-binding and salt templating. *Microporous and Mesoporous Materials*, 95:187–192, 2006.

[61] H. Fujimoto, A. Mabuchi, K. Tokumitsu, and T. Kasuh. Irreversible capacity of lithium secondary battery using meso-carbon micro beads as anode material. *Journal of Power Sources*, 54:440–443, 1995.

[62] K. Sonnenburg, P. Adelhelm, M. Antonietti, B. Smarsly, R. Noske, and P. Strauch. Synthesis and characterization of sic materials with hierarchical porosity obtained by replication techniques. *Physical Chemistry Chemical Physics*, 8:3561–3566, 2006.

[63] H. F. Yang, Y. Yan, Y. Liu, F. Q. Zhang, R. Y. Zhang, Y. Meng, M. Li, S. H. Xie, B. Tu, and D. Y. Zhao. A simple melt impregnation method to synthesize ordered mesoporous carbon and carbon nanofiber bundles with graphitized structure from pitches. *The Journal of Physical Chemistry B*, 108:17320–17328, 2004.

[64] Z. J. Li and M. Jaroniec. Colloidal imprinting: A novel approach to the synthesis of mesoporous carbons. *Journal of the American Chemical Society*, 123:9208–9209, 2001.

[65] T. W.Kim, I. S. Park, and R. Ryoo. A synthetic route to ordered mesoporous carbon materials with graphitic pore walls. *Angewandte Chemie*, 42:4375–4379, 2003.

[66] Y. D. Xia and R. Mokaya. Synthesis of ordered mesoporous carbon and nitrogen-doped carbon materials with graphitic pore walls via a simple chemical vapor deposition method. *Advanced Materials*, 16:1553, 2004.

[67] F. Bonino, S. Brutti, P.Reale, B. Scrosati, L. Gherghel, J. Wu, and K. Mullen. A disordered carbon as a novel anode material in lithium-ion cells. *Advanced Materials*, 17:743, 2005.

[68] H. Buqa, D. Goers, M. Holzapfel, M. E. Spahr, and P. Novak. High rate capability of graphite negative electrodes for lithium-ion batteries. *Journal of the Electrochemical Society*, 152:A474–A481, 2005.

[69] A. S. Arico, P. Bruce, B. Scrosati, J. M. Tarascon, and W. van Schalkwijk. Nanostructured materials for advanced energy conversion and storage devices. *Nature Materials*, 4:366–377, 2005.

[70] O. Barbieri, M. Hahn, A. Foelske, and R. Koetz. Effect of electronic resistance and water content on the performance of RuO2 for supercapacitors. *Journal of the Electrochemical Society*, 153:A2049–A2054, 2006.

[71] A. Rudge, J. Davey, I. Raistrick, S. Gottesfeld, and J. P. Ferraris. Conducting polymers as active materials in electrochemical capacitors. *Journal of Power Sources*, 47:89–107, 1994.

[72] Y. G. Wang, H. Q. Li, and Y. Y. Xia. Ordered whiskerlike polyaniline grown on the surface of mesoporous carbon and its electrochemical capacitance performance. *Advanced Materials*, 18:2619, 2006.

[73] L.-Z. Fan, Y.-S. Hu, J. Maier, P. Adelhelm, B. Smarsly, and M. Antonietti. High electroactivity of polyaniline in supercapacitors by using hierarchically porous carbon monolith as support. *Advanced Functional Materials (in press)*, 2007.

[74] H. Minakuchi, K. Nakanishi, N. Soga, N. Ishizuka, and N. Tanaka. Effect of skeleton size on the performance of octadecylsilylated continuous porous silica columns in reversed-phase liquid chromatography. *Journal of Chromatography*, 762:135–146, 1997.

[75] N. Tanaka, H. Kobayashi, K. Nakanishi, H. Minakuchi, and N. Ishizuka. Monolithic LC columns. *Analytical Chemistry*, 73:420–429, 2001.

[76] N. Tanaka, H. Kobayashi, N. Ishizuka, H. Minakuchi, K. Nakanishi, K. Hosoya, and T. Ikegami. Monolithic silica columns for high-efficiency chromatographic separations. *Journal of Chromatography*, 965:35–49, 2002.

[77] L. Granasy. Nucleation and spinodal decomposition. *Solit State Phenomena*, 56:67–105, 1997.

[78] Günther Gottstein. *Physikalische Grundlagen der Materialkunde*. Springer, 1998.

[79] J. Ozaki, N. Endo, W. Ohizumi, K. Igarashi, M. Nakahara, A. Oya, S. Yoshida, and T. Iizuka. Novel preparation method for the production of mesoporous carbon fiber from a polymer blend. *Carbon*, 35:1031–1033, 1997.

[80] Y. Meng, D. Gu, F. Q. Zhang, Y. F. Shi, L. Cheng, D. Feng, Z. X. Wu, Z. X. Chen, Y. Wan, A. Stein, and D. Y. Zhao. A family of highly ordered mesoporous polymer resin and carbon structures from organic-organic self-assembly. *Chem. Mater.*, 18:4447–4464, 2006.

[81] C. Liang and S. Dai. Synthesis of mesoporous carbon materials via enhanced hydrogen-bonding interaction. *J. Am. Chem. Soc.*, 128:5316–5317, 2006.

[82] M. M. Shapi. Thermal decomposition of polystyrene: Volatile compounds from large-scale pyrolysis. *Journal of Analytical and Applied Pyrolysis*, 18:143–161, 1990.

[83] U. Kasavajjula, C. S. Wang, and A. J. Appleby. Nano- and bulk-silicon-based insertion anodes for lithium-ion secondary cells. *Journal of Power Sources*, 163:1003–1039, 2007.

[84] L. Y. Beaulieu, K. W. Eberman, R. L. Turner, L. J. Krause, and J. R. Dahn. Colossal reversible volume changes in lithium alloys. *Electrochemical and Solid State Letters*, 4:137–140, 2001.

[85] K. P. de Jong and J. W. Geus. Carbon nanofibers: Catalytic synthesis and applications. *Catalytic Reviews: Science and Engineering*, 42:481–510, 2000.